Investigating the Role of Pericytes in Multiple Sclerosis by Inducing Experimental Autoimmune Encephalomyelitis in Genetically Modified Mouse Models

by

Dila ATAK

A Dissertation Submitted to the

Graduate School of Health Sciences in Partial Fulfillment of the

Requirements for the Degree of

Doctor of Philosophy

in

Neuroscience

KOÇ ÜNİVERSİTESİ

December 2021

Investigating the Role of Pericytes in Multiple Sclerosis by Inducing Experimental Autoimmune Encephalomyelitis in Genetically Modified Mouse Models

Koç University Graduate School of Health Sciences

This is to certify that I have examined this copy of a doctoral

dissertation by

Dila ATAK

and have found that it is complete and satisfactory in all respects,

and that any and all revisions required by the final

An examining committee has been made.

Committee Members:

_____

Prof. Dr. Yasemin Gursoy-Ozdemir (Advisor)

_____

Prof. Dr. Erdem Tuzun

_____

Assoc. Prof. Dr. Mujdat Zeybel

_____

Prof. Dr. Mehmet Kaya

_____

Prof. Dr. Aslı Tuncer

_____

Assoc. Prof. Dr. Atay Vural [Co-Advisor]

Date: 15.12.2021

Investigating the Role of Pericytes in Multiple Sclerosis by Inducing Experimental Autoimmune Encephalomyelitis in Genetically Modified Mouse Models

Dila ATAK

Doctor of Philosophy in Neuroscience, December 2021

ABSTRACT

Background: Pericytes are mural cells positioned on the abluminal side of endothelial cells. They have crucial roles in blood-brain-barrier (BBB) maturation and maintaining immune homeostasis in the central nervous system (CNS). Recent studies of pericyte cell cultures and well-characterized pericyte deficiency mouse models suggest that pericytes also have immunomodulatory functions. However, the animals used in these studies are inborn pericyte-deficient mouse models that already have a deficient BBB formation and a disrupted microvasculature morphology. Furthermore, partial ablation of pericytes in developing mice leads to increased infiltration of leukocytes to the CNS in later life, both in steady-state and pathological conditions. These abnormalities might confound the actual findings related to the pericyte function in neuroinflammatory diseases. Therefore, studying the neuroinflammatory roles of pericytes by using the existing pericyte deficiency models is incompetent in making confident conclusions about the findings.

The most ubiquitous neuroinflammatory CNS disease is Multiple Sclerosis (MS). It is a disease of autoimmunity in which the peripheral inflammatory cells infiltrate the brain after the opening of BBB, resulting in the degeneration of myelin sheaths, oligodendrocytes, and underlying nerve fibers. The players initially causing the preternatural passage of these immune cells to the CNS parenchyma are not clearly defined yet. Besides, the line of events happening during the pathogenesis of the disease is also not well-known.

ABSTRACT

Aim: In this study, we first aimed to generate and characterize a tamoxifen-inducible pericyte ablation model in adult mice that have a properly developed vasculature and mature BBB. Secondly, we sought to investigate the effect of pericyte loss in MS pathogenesis through the most frequently used model of MS-like neuroinflammation, the experimental allergic encephalomyelitis (EAE) model.

Methods: To create our inducible pericyte ablation model, PDGFRβ-PA2-CreER$^{+/-}$ mice (JAX Mice, 030201) were crossed with Rosa26-DTA176$^{+/+}$ mice (JAX Mice, 010527). After genotyping, 9-10 weeks old progeny was intraperitoneally injected with 100 mg/kg tamoxifen for two (2X), three (3X), or five (5X) consecutive days to induce the expression of diphtheria toxin in *Pdgfrβ*-positive pericytes. PDGFRβ-Cre^{+}/DTA176^{+} (Cre-positive) mice were characterized as pericyte ablation group, and PDGFRβ-Cre^{-}/DTA176^{+} (Cre-negative) mice were used as controls. To characterize our model, the level of pericyte coverage, *Pdgfrβ* gene expression, and vasculature changes were examined in the brain and spinal cord tissues of both groups. To do so, immunohistochemistry, quantitative PCR, and AngioTool software were used, respectively. The analyses were separately done for the short-term (15 days) and long-term (60 days). Additionally, behavioral tests of spatial recognition memory (Y-maze performance) and locomotor activity (Grip Strength Test) were run. According to the results of the characterization experiments, the pericyte ablation group that was administered with two consecutive days of TAM injections (2X TAM) was selected for further EAE experiments. EAE was induced by MOG_{35-55} EAE kit (Hooke Labs, EK2110) 15 days after TAM injections. Cre-negative and wild-type C57BL/6 mice were used as pericyte ablation controls for EAE experiments, and they together were considered as “wild-type mice” when discussing the results. After EAE induction, weight and clinical symptom variations were monitored and scored for 28 days. Statistical analysis was done by repeated-measures 2-way ANOVA multiple comparison test.

Results: There was a 75% (+-SEM=0.9192) decrease in pericyte coverage of the cortex ($p<0.01$) and a 40% (+-SEM=2.385) decrease in the pericyte coverage of the spinal cord ($p<0.01$) in the 2X TAM pericyte ablation group mice (n=8) compared to the Cre-negative controls (n=7). Similarly, *Pdgfrβ* gene expression was decreased to 10 % (+-SEM=2.230) in the cortex ($p=0.036$) and 60% (+-SEM=4.511) in the spinal cord ($p=0.036$). The vessel analysis and the behavioral analysis revealed no significant

differences between the 2X TAM pericyte ablated group and Cre-negative controls. Based on these results, pericyte ablated mice created with 2X TAM were chosen to be used in EAE experiments.

During EAE, the pericyte ablated mice (n=7) and the wild-type mice (n=23) had similar clinical progression up to score 1.5 until the 15th day of the EAE induction. However, after that time point, the symptoms of the pericyte ablated mice started to worsen with a higher exacerbation rate. This difference got statistically significant after Day 20 and continued till the end of the experiment (p= 0.0141, 0.0056, 0.008, 0.0276, and 0.0188 at Day20-28). Concurrently, starting with the first symptoms of EAE, pericyte ablated mice also lost more weight than the wild-type mice (p= 0.0411, 0.0067, 0.0236, 0.0093, 0.01, 0.0194, and 0.0081 at Day8 and Day16-28). On the other hand, the immunohistochemical analysis of the spinal cord tissues revealed that the number and the size of inflammatory lesions were more and larger in the pericyte ablated mice compared to the lesions of the wild-type mice. Additionally, the periventricular region of the brain presented unprecedented inflammatory foci in pericyte ablated mice, while the wild-type EAE mice did not show any cell accumulations in the brain.

Conclusion and Comment: This project has generated and characterized a TAM inducible pericyte ablation model in adult mice. The advantages of this new generation pericyte ablation model over the other pericyte deficiency models are that pericyte ablation amount and ablation induction time could be controlled, and while so, the model does not require the injection of any toxin. In this project, by using our pericyte ablation model in combination with the EAE model, pericytes were shown to play a protective role during the resolution of neuroinflammation.

Key Words: Blood-Brain Barrier, Pericytes, Pericyte Ablation, Pdgfrβ, Multiple Sclerosis, Experimental Allergic Encephalomyelitis, Transgenic Mouse Models

ÖZETÇE

Transgenik Farelerde Deneysel Alerjik Ensefalomiyelitis Modeli Kullanılarak Multipl Skleroz Hastalığında Perisitlerin Rolünün İncelenmesi

Dila ATAK

Sinirbilim Ph.D., Aralık 2021

Giriş: Perisitler, endotel hücrelerinin abluminal tarafında yer alan mural hücrelerdir. Bu hücreler kan-beyin bariyeri (KBB) oluşumunda ve santral sinir sistemi (SSS) bağışıklık homeostazını sağlamada önemli rollere sahiptirler. Son yıllarda, perisit hücre kültürleriyle ve iyi karakterize edilmiş perisit ablete fare modelleyle yapılan çalışmalar, perisitlerin ayrıca immünomodülatör fonksiyonlara sahip olduğunu göstermektedir. Fakat, bu çalışmalarda kullanılan hayvanlar doğuştan perisit eksikliği olan fare modelleridir ve zaten yetersiz bir BBB oluşumuna ve bozulmuş bir mikrovaskülatür morfolojiye sahiptirler. Ayrıca, gelişmekte olan farelerde perisitlerin kısmi ablasyonu, hem normal fizyolojik durumda hem de patolojik koşullarda lökositlerin SSS'e infiltrasyonunun artmasına neden olduğu bilinmektedir. Bu anormallikler, nöroinflamatuar hastalıklarda perisit fonksiyonuyla ilgili gerçek bulguları gölgeyleyebilir. Bu nedenle, mevcut perisit eksikliği modellerini kullanarak perisitlerin nöroinflamatuar rollerini incelemek, bulgular hakkında güvenli sonuçlar çıkarma konusunda yetersiz kalmaktadır.

En yaygın nöroinflamatuar CNS hastalığı Multipl Skleroz'dur (MS). MS hastalığı periferik inflamatuar hücrelerin KBB'nin açılmasından sonra beyne sızdığı ve

miyelin kılıflarının, oligodendrositlerin ve altta yatan sinir liflerinin dejenerasyonuna neden olduğu bir otoimmünite hastalığıdır. Başlangıçta bu bağışıklık hücrelerinin CNS parankimine olağandışı geçişine neden olan hücreler henüz net olarak tanımlanmamıştır. Bunun yanı sıra, hastalığın patogenezi sırasında meydana gelen olaylar dizisi de bilinmemektedir.

Amaç: Bu çalışmada, ilk olarak, normal gelişmiş vasküler yapıya ve sağlıklı KBB'ye sahip yetişkin farelerde tamoksifen ile indüklenebilir bir perisit ablasyon modeli oluşturmayı ve karakterize etmeyi amaçladık. İkinci olarak, en sık kullanılan MS benzeri nöroinflamasyon modeli olan deneysel alerjik ensefalomiyelit (DAE) modeli aracılığıyla perisit yokluğunun MS patogenezine etkilerini araştırdık.

Yöntem: Indüklenebilir perisit ablasyon modelimizi oluşturmak için PDGFRβ-PA2-CreER$^{+/-}$ fareler (JAX Laboratories, 030201) ile Rosa26-DTA176$^{+/+}$ fareler (JAX Laboratories, 010527) çaprazlandı. Bu çiftleşme sonucu elde edilen 9-10 haftalık yavrular genotiplendikten sonra, *Pdgfrβ*-positive perisitlerinde difteri toksin ifadesini indüklemek için iki (2X), üç (3X) veya beş (5X) ardışık gün boyunca intraperitonel yolla 100 mg/kg tamoksifen enjeksiyonları yapıldı. PDGFRβ-Cre^{+}/DTA176^{+} (Cre-pozitif) fareler perisit ablasyon grubu olarak ve PDGFRβ-Cre^{-}/DTA176^{+} (Cre-negatif) fareler kontrol olarak karakterize edildi. Modelimizi karakterize etmek için, her iki grubun beyin ve omurilik dokularında endotel üzerindeki perisit kaplama alanı, PDGFRβ gen ifade seviyesi ve damar ilişkili değişiklikler incelendi. İncelemeler için sırasıyla immünohistokimya, kantitatif PCR ve AngioTool [1] yazılımı kullanıldı. Analizler kısa dönem (15 gün) ve uzun dönem (60 gün) için ayrı ayrı yapıldı. Ek olarak, uzamsal tanıma belleği (Y-labirent performansı) ve lokomotor aktivite (Kavrama Kuvveti Testi) davranış testleri yapıldı. Karakterizasyon deneylerinin sonuçlarına göre, sonraki DAE deneyleri için iki ardışık gün TAM enjeksiyonu (2X TAM) ile indüklenen perisit ablasyon grubu seçildi. DAE modeli, TAM enjeksiyonlarından 15 gün sonra MOG_{35-55} DAE kiti (Hooke Labs, EK2110) ile başlatıldı. DAE deneylerinde perisit ablasyonu kontrolü olarak kontrolleri olarak Cre-negatif ve yabanıl tip C57BL/6 fareleri kullanıldı ve sonuçlar tartışılırken iki grup birlikte "yabanıl tip fareler" olarak değerlendirildi. DAE deneyleri başlatıldıktan sonra, ağırlık ve klinik semptom varyasyonları 28 gün boyunca izlendi. İstatistiksel analiz, 2-yönlü ANOVA tekrarlanan ölçümler çoklu karşılaştırma testi ile yapıldı.

Bulgular: Perisit endotel kaplama alanında cortekste %75 (+-SEM=0.9192) ($p<0.01$) ve omurilikte %40 (+-SEM=2.385) azalma ($p<0.01$) gözlemlendi. 2X TAM perisit ablasyon grubu fareler (n=8), Cre-negatif kontroller (n=7) ile karşılaştırıldığında, perisit kaplama alanı sonuçlarına benzer şekilde, *Pdgfrβ* gen ekspresyonu kortekste %55'e (+-SEM=2.230) ($p=0.036$) ve omurilikte %60'a (+-SEM=4.511) düştü ($p=0.036$). Damar analizleri ve davranış analizleri ise, 2X TAM perisit ablasyonlu grup ile Cre-negatif kontroller arasında önemli bir fark olmadığını ortaya koydu. Bu sonuçlardan yola çıkarak DAE deneylerinde 2X TAM ile oluşturulan perisit ablete farelerin kullanılması kararlaştırıldı.

DAE sırasında, perisit ablasyonlu fareler (n=7) ve yabanıl tip fareler (n=23), DAE modelinin 15. gününe kadar skor 1.5 seviyesine benzer klinik gelişime sahipti. Fakat, deneyin bu noktasından sonra, perisit ablasyonu yapılmış farelerin semptomlarının daha yüksek bir alevlenme oranı ile kötüleştiği izlendi. Bu fark 20. günden sonra istatistiksel olarak anlamlılık kazandı ve bu anlamlılık deneyin sonuna kadar devam etti (20-28. günlerde $p= 0.0141$, 0.0056, 0.008, 0.0276 ve 0.0188). Eşzamanlı olarak, DAE'nin ilk semptomlarından başlayarak, perisit ablasyonu yapılmış fareler yabanıl tip farelerden daha fazla kilo kaybettiler ($p= 0.0411$, 0.0067, 0.0236, 0.0093, 0.01, 0.0194 ve 0.0081, 8. gün ve 16-28. günlerde). Öte yandan omurilik dokularının immünohistokimyasal analizi, yabanıl tip farelerin lezyonlarına kıyasla perisit ablasyonlu farelerde enflamatuar lezyonların sayısının ve boyutunun daha fazla ve daha büyük olduğunu ortaya koydu. Ek olarak, beynin periventriküler bölgesi, perisit ablasyonlu farelerde benzeri görülmemiş enflamatuar odaklar sunarken, yabanıl tip DAE'li fare beyinlerinde herhangi bir hücre birikimi gözlenmedi.

Sonuç ve Yorum: Bu projede, yetişkin farelerde TAM ile indüklenebilir bir perisit ablasyon modeli oluşturuldu ve karakterize edildi. Bu yeni nesil perisit ablasyon modelinin diğer modellere kıyasla avantajı, bu modelde perisit ablasyonunun hem de ablasyon miktarının hem de ablasyonun başlangıç zamanının kontrol edilebilmesi ve bu kontrol süreçlerinde modelin herhangi bir toksin enjeksiyonu gerektirmemesidir. Bu proje kapsamında, perisit ablasyon modelimizin DAE modelinde kullanılmasıyla, perisitlerin nöroinflamasyonun çözülmesi sırasında koruyucu bir rol oynadığı gösterilmiştir.

Anahtar Kelimeler: KBan-Beyin Bariyeri, Perisit, Perisit Ablasyonu, Pdgfrβ, Multiple Sclerosis, Deneysel Allergic Ensefalomiyelit, Transjenik Fare Modelleri

ACKNOWLEDGMENT

First and utmost, I need to express my heartfelt appreciation to my research supervisors, Prof. Dr. Yasemin Gürsoy Özdemir, and my co-advisor, Assoc. Prof. Atay Vural, whose sagacity and erudition was inestimable in formulating the research questions and methodology of my thesis project. Their tactful feedback led me to hone my thoughts and perception and brought my work to its possible apex. This thesis project could have never reached the quality it has without their prop up and enlightenment and devoted involvement in every step throughout the Sisyphean journey of my Ph.D. and research. Also, I want to express the most inexpressable appreciation to the KUTTAM director, Prof. Dr. Ihsan Solaroğlu, an avuncular man of profundity and geniality, who bolstered and backed me up in all stages of my academia.

I would also like to express my tribute to my committee members, including Prof. Dr. Erdem Tüzün, Prof. Dr. Mehmet Kaya, Prof. Dr. Meryem Aslı Tuncer, and Assoc. Prof. Müjdat Zeybel. Also, thanks to Assoc. Prof. Gülayşe Ince Dunn who was my first-year Ph.D. advisor before she closed her laboratory at Koç University. She was also the professor of my first Neuroscience course. Her teaching style and enthusiasm for conveying and delivering her knowledge have inscribed an indelible interest in academia and research in me. Similarly, thanks go to Prof. Dr. Nazlı Başak, who was the first professor to draw my interest into the field of Neuroscience by accepting me to her laboratory as a freshman intern in my undergraduate study of Molecular Biology and Genetics field.

I would like to thank all of my colleagues in the YGO Lab and Vural Lab of the KUTTAM family, starting from Aysu Bilge Gökyüzü, Esra Özkan, Mohammadreze Yousefi, for helping me with the experiments that run for this thesis project. Also, special thanks to the animal facility staff, Nilhan Coşkun, Ahmet Kocabay, Mustafa Demir, and Muhammed Reşat Oğuzkan Yaralı, who have been unwavering in their personal and professional support during my long-lasting animal experiments.

Getting through my dissertation required more than academic and technical support, and I have had many, many people to thank for listening and empathizing with me over the past five years. Accolading and appreciating their friendship cannot be

expressed through these incapable words! I especially thank my most beloved and kindest friend and colleague, Erdost Yıldız, for making me feel like I have someone to rely on in every possible professional and emotional obstacle I had. Similarly, I would like to thank my beautiful and successful friend and housemate, Buse Cevatemre, for her unjudgemental and unconditional support in every aspect of my life. I would also like to thank Assos. Prof. Ceyda Açılan Ayhan and CAA lab members for accepting me as an honorary member when I was far from my own lab located on the hospital campus.

Most importantly, none of this could have happened without my family. I exceptionally thank my father for being the role model of endurance and strength in my life. To my mother, who has been the meaning of care and sacrifice. To my brother, who brought the *joie de vivre* to my life from his very existence. This dissertation stands as a true testament brought about by their unconditional love and gratitude.

Additionally, my interns have played an integral, indispensable role in my experiments. I do appreciate their 7/24 presence, assistance, and support. Thanks especially goes to Zeynep Lal Caan, Çiçek Kanar, Furkan Hoşer, Melike Cevizci.

Also, I like to express my gratitude toward my friend Mert Bayer for his backups in every way possible and not only that but also for his contribution and guidance in coding for confocal image analysis in collaboration with my colleague Erdost Yıldız.

At the end of the day, I would also want to accolade and acclaim Hamed A. Ranjbar, my affectionate and sterling friend. His contribution and solicitude to the ultimate stage of Ph.D. and related emotional burden as an expert proofreader and as a clinical psychologist have facilitated and eased my toughest stage to reach the idealized culmination.

Funding

This Project is funded by TUBITAK 1001 (116S552), TUBITAK 1003 (216S656), TUBITAK 2236 (119C018) Research Funds, and Koç University Research Center for Translational Medicine (KUTTAM), equally funded by the Republic of Turkey Ministry of Development Research Infrastructure Support Program.

TABLE OF CONTENTS

LIST OF TABLES

LIST OF FIGURES

ABBREVIATIONS

Ang1	Angiopoietin 1
APC	Antigen Presenter Cell
aSMA	Alpha Smooth Muscle Actin
BBB	Blood-Brain Barrier
BSCB	Blood-Spinal Cord Barrier
BLK1	B lymphoid tyrosine kinase
CD13	Cluster of Differentiation 13
CD146	Cluster of Differentiation 146
CFA	Complete Freund's Adjuvant
CIS	Clinically Isolated Syndrome
CNS	Central Nervous System
CO_2	Carbondyoxide
CreER	Cre Recombinase-Estrogen Receptor
C_T	Cycle of Threshold
DPBS	Dulbecco′s Phosphate Buffered Saline
dpi	Day Post Injection
DT	Diphtheria Toxin
DTA	Attenuated Diphtheria Toxin
DTR	Diphtheria Toxin Receptor
iDTR	Inducible Diphtheria Toxin Receptor
EAE	Experimental Allergic Encephalomyelitis
EC	Endothelial Cell
GDNF	Glial cell line-Derived Neurotrophic Factor

GFAP	Glial Fibrillary Acidic Protein
GLAST	Glutamate Aspartate Transporter
GM	Gray Matter
HBVP	Human Brain Vascular Pericytes
H&E	Hematoxylin and Eosin
K^+	Potassium
KCNJ8	Potassium Inwardly Rectifying Channel Subfamily J Member 8
LAMs	Leukocyte Adhesion Molecules
LPS	Lipo Poly Saccharide
MBP	Myelin Basic Protein
MHC	Major Histocompatibility Complex
MMPs	Matrix Metalloproteinases
MOG	Myelin Oligodendrocyte Glycoprotein
mRNA	Messenger ribonucleic acid
MS	Multiple Sclerosis
MSC	Mesenchymal Stem Cells
NAWM	Normally Appearing White Matter
NG2	Neuron-Glial Antigen 2
NGS	Normal Goat Serum
NVU	Neurovascular Unit
O_2	Oxygen
OPC	Oligodendrocyte Precursor Cells
PCs	Pericytes
PCR	Polymerase Chain Reaction
Pdgfβ	Platelet Drived Growth Factor β

Pdgfrβ	Platelet Drived Growth Factor Receptor β
PFA	Paraformaldehyde
PLP	Proteolipid protein
PPMS	Primary Progressive Multiple Sclerosis
PTN	Pleiotrophin
PTX	Pertussis Toxin
PVAP	Plasmalemma Vesicle-associated Protein
RRMS	Relapsing Remitting Multiple Sclerosis
RGS5	Regulator of G protein Signalling Protein 5
SRMS	Secondary Progressive Multiple Sclerosis
TAM	Tamoxifen
2X TAM	Two consecutive doses of Tamoxifen injection group
3X TAM	Three consecutive doses of Tamoxifen injection group
5X TAM	Five consecutive doses of Tamoxifen injection group
TCR	T cell Receptor
VEGF-A	Vascular Endotelial Growth Factor
VSMC	Vascular Smooth Muscle Cells
WT	Wild Type
WM	White Matter

CHAPTER 1

1 INTRODUCTION

1.1 Blood-Brain Barrier

The blood-brain barrier (BBB) is a tightly controlled physical barrier separating the peripheral and (Central Nervous System) CNS circulation from each other. It prevents the passage of the large molecules from the circulating blood to the CNS parenchyma and ensures CNS protection from the harms of potentially toxic molecules. While so, it selectively permits the passage of necessary nutrients to the CNS parenchyma with the assistance of selective transporters [2]. It also cooperates in the removal of waste products from the CNS parenchyma [3]. Meanwhile, the necessary gaseous molecules or wastes (O_2 and CO_2) can readily diffuse from the endothelial membrane [4]. Therefore, the presence of BBB provides the CNS with a suitable environment for the healthy and effective synaptic transmission and the proper functioning of the vasculature [5]. BBB gains these functions mainly owing to its specialized endothelial cells (ECs). ECs of the BBB have different physiological properties than the other ECs of the body. Firstly, they lack the fenestrations between them [6]. Secondly, they have an overabundant expression of tight junction proteins (e.g., zonula ocludens-1, occludin, claudin-5). Supporting the tight control of transcytosis, they have a limited number of pinocytic vesicles [7]. All these properties of BBB make the brain and spinal cord very well-protected and immune-privileged organs [8].

In addition to specialized endothelial cells, BBB structure consists of various other components such as astrocyte end-feet, pericytes, and a 30-40 nm thick basal lamina positioned between the ECs and the plasma membrane of astrocyte end-feet [9] (Figure 1). The basal lamina is composed of many proteins (such as Laminin, Collagen-IV), and it ensheathes the pericytes wrapping the ECs. Brain extracellular matrix proteins such as laminin, elastin, fibronectin, and tenascin also contribute to the function of BBB [10]. The communication between these BBB components and nearby

interneurons is called Neurovascular Coupling, and all these cell types and protein structures are named Neurovascular Unit (NVU) (Figure 1). NVU regulates the perfusion according to the local metabolic demands of neurons [11].

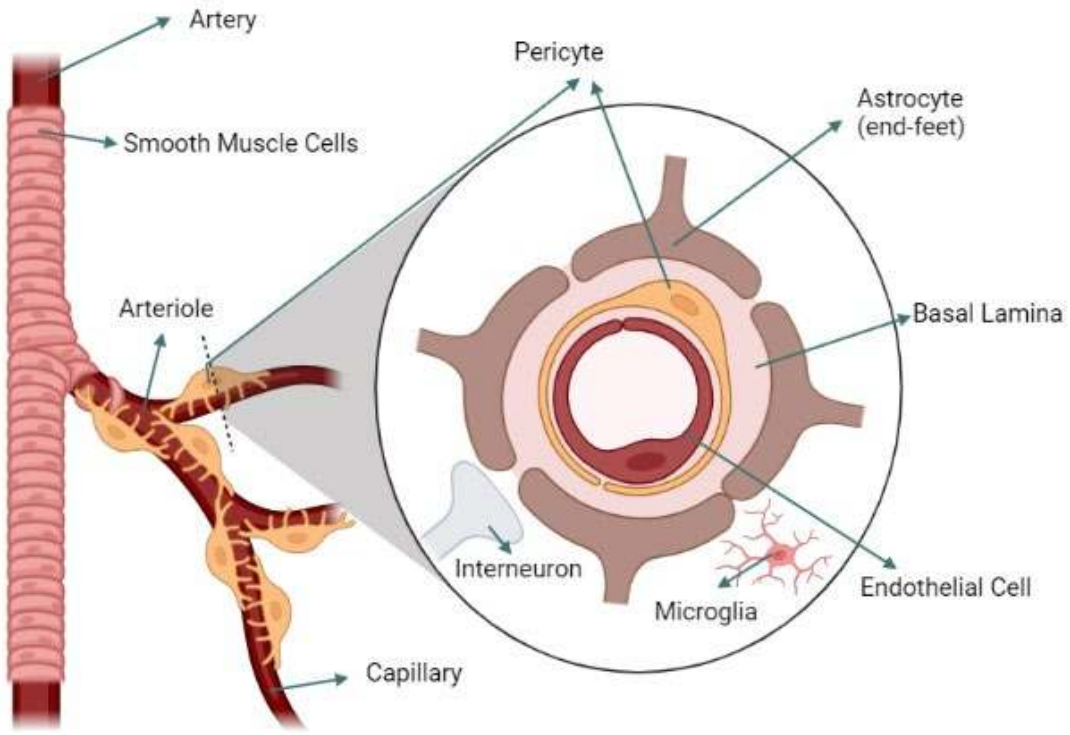

Figure 1. The Neurovascular Unit

The arteries of the CNS are wrapped with Smooth Muscles Cells while the processes of the pericytes coved the pre-capillary arterioles and the capillaries. These cell types, along with the endothelial cells and astrocyte end-feet, make up the blood-brain barrier. Pericytes are located on the abluminal surface of the capillaries, embedded in the basal lamina. All these cell types communicate with each other and with the neighboring interneurons and the microglia to ensure homeostasis within CNS. The interactions between the components of these cells, the so-called neurovascular unit, are referred to as the neurovascular coupling.

1.2 Pericytes

Pericytes are multifunctional mesenchymal cells of vasculature located on the abluminal side of the pre-capillary arterioles, capillaries, and post-capillary venules. Pericytes were first described in 1873 as "Rouget cells" and mural cells by Charles Rouget. Then, Zimmerman reintroduced them in 1923 as "Pericytes" [12]. They are found all around the body with different numbers, morphologies, and functions. The pericyte/endothelial cell ratio is highest in the retina (1:3 ratio) and the brain (1:5 ratio),relatively[13].

1.2.1 Pericyte Morphology and Types in CNS

The pericyte cell body consists of a prominent nucleus surrounded by a small amount of cytoplasm. Primary processes protrude from both sides of the round cell body in a direction parallel to the vessel wall. Secondary extensions come out in different directions from these primary processes, and they circumstantially wrap the vessel wall. This typical pericyte morphology is referred to as "bump on a log" morphology [14] (Figure 1). Pericytes are embedded in the endothelial cells' basement membrane and cover 22-32% of the capillaries [15]. There are also direct contact points of pericytes to the endothelial cells without any basement membrane between them. These contacts can be established through various structures, including gap junctions, adhesive plaques, and "peg and socket" connectors. Gap junctions allow the direct connection between the cytoplasm of cells and the passage of small molecules and ionic currents. Adhesive plaques have fibronectin-reach microfilament bundles attached at the pericyte plasma membrane, and they provide adherence between pericytes and electron-dense material in the opposing endothelial cytoplasm [16]. On the other hand, peg and socket connections are interlinking outgrowths (pegs) from one cell to other that reciprocally intertwine with (peg into the socket) each other [17]. These different pericyte connections determine pericyte morphology which changes depending on the vessel type. For example, pericytes have more extension in the pre-capillary arterioles, and their morphology gets closer to the morphology of the vascular smooth muscle cells (VSMCs) covering the arterioles (Figure 1). They are shorter in length, and they offer

more comprehensive coverage of the endothelial surface. These pericytes are subclassed as “ensheathing pericytes” or “translational pericytes” [18]. On the true capillaries, pericyte morphology is characterized by a conspicuous ovoid cell body and hundreds of micrometers long very thin protrusions along the capillary walls. This pericyte type is called “thin strand pericyte”. On the arteriolar side of the capillary and the post-capillary venules, pericytes gain a mesh-like morphology with better coverage of the capillary's abluminal surface and are called “mesh pericytes” [19,20].

1.2.2 Pericyte Identification

Although there are many markers for pericytes, no single marker is exclusively specific to pericytes. This is because pericytes are very heterogeneous, and the marker expressions could change depending on their developmental stage[21]. Therefore, pericytes are identified by a combination of markers that would allow the differentiation from the other cells having similar marker expressions with pericytes (such as SMCs and Mesenchymal Stem Cells (MSCs). Moreover, pericytes can be recognized by considering their different features, such as pericyte-specific antibody staining, anatomical positioning, and appropriate morphology. The markers that are used for pericyte staining are listed in Table 1.

Table 1. Known Pericyte Markers

Marker	Category	Function	References
Pdgfrβ	Tyrosine-kinase receptor	Pericyte recruitment during angiogenesis/BBB formation, proliferation	22,23
NG2	Membrane chondroitin sulphate proteoglycan	Cell adhesion, cell-cell communication, migration, proliferation, angiogenesis	24,25
CD13	Type II membrane zinc-dependent metalloprotease	Peptide cleavage, adhesion, migration, proliferation	26,27
αSMA	αSMA Contractile filament/ structural protein	Vessel contraction	23,28
RGS5	GTPase-activating protein	Controls PDGFRβ signaling during vascular maturation	29,30
KCNJ8	Inwardly rectifying potassium channel subfamily	Associates with SUR2	31
SUR2	Regulatory subunit of ATP-sensitive potassium channels	Regulation of ATP-sensitive potassium channels	31
BLK1	Transmembrane cell surface protein	Modulates Notch signaling and differentiation	31,32
CD146	Adhesion molecule	Leucocyte extravasation	33,34
Desmin	Contractile filament/structural protein	Vessel contraction	35

1.2.3 Functions of Pericytes in CNS

In the last decade, various functions were attributed to pericytes. They serve in the formation and maintenance of BBB, blood flow regulation, angiogenesis, glial scar formation, secretory processes, neuromodulation, plasticity, etc.[36]. In this section, some of the best-studied functions of pericytes were explained.

Regulation of blood flow

Cerebral blood flow is dynamically regulated through neurovascular coupling to meet the local oxygen and nutrient needs of neurons. VSMCs are the primary cell type responsible for the dilation and constriction of blood vessels depending on the local cues [37]. However, these cells are not present on the capillaries, and instead, pericytes cover the capillaries [38]. Therefore, it is tempting to think that pericytes are the ones to regulate capillary diameter when demanded by the neighboring cells. Furthermore, pericytes express contractile proteins such as tropomyosin, myosin, aSMA[39]. They also have some filamentous protein expression known to control the structural integrity during cell contraction, namely Vimentin and Desmin [40].

In vivo imaging studies have shown that when the neuronal activity and the glutamate release to the extracellular environment increase, the capillary pericytes relax to allow the dilation of capillaries and increase of the blood flow [41]. On the other hand, during mild ischemia, resultant oxidative stress induces pericyte contraction [23]. This situation obstructs the regaining of the capillary flow. Furthermore, in the prolonged ischemia case, pericytes die and go into a steady contracted state of rigor. Since pericytes cannot relax after rigor, the cerebral perfusion could not be regained, and hypoperfusion was observed[42]. In spite of these data, there is still a debate on contractibility and cerebral blood flow functioning of the pericytes because the contractibility could not be observed directly. Since it is hard to distinguish pericytes from contractile VSMCs, it is challenging to attribute the blood flow variations to pericyte contractility directly. However, new data continues to accumulate, suggesting pericytes have a role in cerebral blood flow regulation. For example, a recent study showed that inducible brain-specific pericyte ablation leads to circulatory failure as well as neuronal loss [43].

BBB formation and maintenance

Pericytes have crucial roles in the maintenance of the proper blood vessel functioning besides their contribution to the formation of new vessels and extracellular matrix components [44]. The fact that the pericyte/endothelial cell number ratio is the highest in the retina and the brain compared to the other organs suggests a link between the BBB formation and functioning to the pericytes [5,45-47]. Additionally, the existence of the tight junctions between the ECs and pericytes and pericyte contribution to the tight junction protein synthesis through their Angiopoietin 1 (Ang1) signaling makes it presumable that they are an essential cell type for the BBB selective permeability and neurovascular coupling[48,49]. Also, they secrete glial cell line-derived neurotrophic factor (GDNF) that promotes the Claudin5 tight junction protein production[48]. Moreover, pericytes were implicated in the control of vesicle trafficking [50] and regulation of active transporter expression [51]. Specifically, they regulate Transferrin expression in ECs and Aquaporin4 expression in astrocytes [50].

The most convincing data about their roles in BBB maintenance comes from the studies of pericyte deficient transgenic mouse models. Decreased pericyte coverage resulted in increased capillary diameter and BBB leakage in $Pdgfr\beta^{+/-}$ knock out and $Pdgfr\beta^{F7}$ point mutation mice[50,52]. Microarray gene expression analysis of CD31+ endothelial cells in the $Pdgfr\beta^{-/-}$ mice revealed that there was no downregulation of BBB genes; however, the genes that were known to increase the BBB permeability such as Angpt2, Plvap, and leukocyte adhesion molecules (LAMs) were upregulated [52]. This suggests that pericytes have a role in the suppression of BBB permeability. Tight junction disposition was also disrupted in pericyte deficient mice[50,52]

Angiogenesis

In embryonic development, initial vessel formation happens very early to provide the embryo's nutrient and oxygen needs. The initial de novo vessel formation from endothelial cell precursor (angioblast) is called vasculogenesis. The construction of new blood vessels from the pre-existing vessels is called angiogenesis [35]. Angiogenesis can happen throughout the organism's lifespan, but is it minimal and tightly controlled during adulthood [53]. Angiogenesis starts in case of insufficiency of

existing vascular plexus and resultant hypoxia. Hypoxic environment triggers the neighboring cells to secrete angiogenetic factors such as Vascular Endothelial Growth Factor A (VEGF-A), which endothelial cells sense and react to [54,55]. The endothelial cell located where the most angiogenic factor gradient exists becomes the tip EC and starts the sprouting towards the attractant angiogenic factor gradient [56]. Meanwhile, pericytes detach from the blood vessel, and ECs secrete enzymes such as Matrix metalloproteinases (MMPs) to digest the existing basal lamina. This degradation enables the tip EC to progress further into the parenchyma [57]. When the two tip ECs from different ancestor vessels meet at some point, they form the immature capillary network [55]. Then, ECs start to secrete platelet-derived growth factor β (PDGFβ) to recruit pericytes to the vessel wall [38]. PDGFβ is sensed by PDGFRβ receptors on pericytes and the NG2 receptor (as a co-receptor of PDGFβ) [58,59]. Due to the pericyte recruitment and further pericyte-endothelial cell coupling, the capillary gets matured and stabilized. The interaction between the pericytes and endothelial cells also promotes the new basal lamina formation [44]. Additionally, pericyte-endothelial cell coupling activates the (transforming growth factor β) TGFβ [60] and TGFβ inhibits further endothelial cell proliferation and migration [61]. It also downregulates the VEGF receptor expression on the ECs [62]. VEGF receptor expression is further downregulated by Notch signaling through the Notch receptors of pericytes [56]. Angiogenin1 (Ang1) secretion by pericytes stabilizes the newly formed vessels by activating the Tie2 receptors on ECs [63].

Transgenic models of pericyte deficiency further strengthened the importance of pericytes for vascular development and stabilization. When Pdgfrβ or its ligand Pdgfβ is genetically knocked out, mice die in the embryonic stage due to the microvascular hemorrhage [64,65]. The miscommunication or loss of communication between endothelial cells and pericytes leads to uncontrolled EC proliferation and leaky and unstable vessel formations [66,67].

Scar formation

Tissue injury provokes scarring as a natural reaction that happens when fibrous material is deposited to aid wound healing. The scar formation after a CNS injury protects the cell viability in the penumbra by isolating the injured area. While the

deposited scar tissue is useful ad hoc, it serves as an impregnable blockade that impedes axonal regrowth and is extremely pernicious to cerebral tissue regeneration [68]. Astrocytes include the bulk of cells in the CNS scar, also known as glial scars. Astrocytes become hypertrophic, proliferate rapidly, increase extracellular matrix (ECM) deposition, and express higher levels of the intermediate filaments glial-fibrillary-acid protein (GFAP) and vimentin after a brain injury. These mechanisms corroborate creating a dense network of astrocyte pseudopodia, which fills the gap left by dying cells [69]. As the second-most abundant cells in glial scars and the CNS's major macrophages, microglia migrate quickly to the injured site, attempting to restore tissue homeostasis by removing apoptotic cells and necrotic debris [69].

Despite that CNS scarring has been attributed only to glial cells [70], pericytes have been found to play a role in non-glial CNS scarring. Following injury, local tissue pericytes in almost all organs differentiate into myofibroblast-like cells and induce tissue fibrosis [71,72]. Genetic fate tracking was used to demonstrate the subpopulation of glutamate aspartate transporter (GLAST) expressing pericytes and their detachment from vessel walls and subsequent migration after spinal cord damage [73]. Pericytes at the damaged region mature into αSMA-expressing myofibroblast-like cells with increased ECM production, leading to the glial scar formation [73]. In the damaged spinal cord, a subtype of pericyte (about 10% of the overall population) has been observed to differentiate into a scar-forming stromal cell [73]. These cells translocate from their perivascular stance, are drawn to the damage site, and become positive for fibroblast markers. They 'seal' the damaged tissue by forming large networks of extracellular matrix proteins, which finally make up connective tissue and form the stromal component of scar tissue. This structure is formed to prevent further damage.

1.2.4 Pericytes in Neuroinflammation

When the pericytes are incubated with the inflammatory cytokines, the expression of inflammatory genes prominently increases [74]. Therefore, pericytes are thought to serve as neuroinflammatory cells by acquiring new functions during inflammation.

After stimulation of primary brain microvascular pericyte culture cells with Lipo Poly Saccharide (LPS) and/or cytokines (e.g., IFNγ, TNFα, IL1β, TGFβ, and IL17), an upregulation in the expression of chemokine, cytokine, and other inflammation-related genes has been observed [75,76] (Table 2).

Table 2. Summary of immune mediators expressed by pericytes (Modified from[89])

Immune Family	Immune Mediator
Immune family	Immune mediator
Adhesion molecules	ICAM-1, VCAM-1, MCAM
Chemokines	CCL2(MCP-1), CCL3, CCL4, CCL5, CCL11, CXCL1, CXCL8 (IL-8), CXCL10 (IP-10), CX3CL1
Cytokines	IL-1/, IL-1b, IL-2, IL-3, IL-4, IL-5, IL-6, IL-9, IL-10, IL-12, IL-13, IL-17, IL-18, IL-33, IFNɣ, TNF/, G-CSF, GM-CSF
Antigen presentation	MHCII/HLA-DR
ROS/RNS	iNOS/NO, NOX4/O_2^-
Transcription factors	NF-κB, C/ EBPδ, STAT1, SMAD2/3
Phagocytic/endocytic receptors	Fc receptor, CR3, CD36, CD47, CD68, LRP-1
MMPs	MMP2, MMP9

Pericytes can express major histocompatibility complex-II (MHC-II) molecules to act like antigen presenter cells (APCs). They also have the phagocytotic capability. In addition, they can affect T cells, monocytes/macrophages, and neutrophils with the cytokines and chemokines they secrete [75-77]. There is little study of the role of pericytes in neuroinflammation in vivo. In a study conducted with HIV patients, widespread pericyte loss was found in the brain [78]. In another study, it was shown that pericytes in the brain were activated after systemic LPS injection, and they were the first cells to

respond to systemic inflammation in the brain [79]. Loss of pericytes leads to leukocytes entering the brain and may modulate the inflammatory response.

1.2.5 Conventional In Vivo Pericyte Deficiency Models and Their Contributions to Literature

Heretofore, many transgenic pericyte deficiency animal models have been used to study the function of pericytes in health and various diseases. These models were mostly focused on transgenic manipulations to impose loss of function in pericyte-related signaling molecules or receptors. Here, I will concisely review the literature and related findings on pericyte deficiency models employed thus far.

Pdgfβ$^{-/-}$

The first attempt to create a pericyte deficiency model happened in 1994 by Leven et al. In this project, they created a complete loss of function in the *Pdgfβ* gene (Pdgfβ$^{-/-}$), the main ligand for pericyte signaling, by deleting sequences that encode a major part of the mature protein (exon3 and exon4)[64]. However, that model failed to study the complete loss of function of pericytes due to the pre-natal death of animals around E17.5-18.5 with hemorrhagic and edematous phenotypes. They further investigated the effect of PDGFβ loss in the prenatal time window and found that these mice had abnormal kidney glomeruli, heart and blood vessel dilation, anemia, thrombocytopenia, and hemorrhages. They later discovered that, although Pdgfβ$^{+/+}$ (wild-type) or Pdgfβ$^{+/-}$ (partial loss of function) capillaries were straight and had a constant diameter (~5μm), Pdgfβ$^{-/-}$ capillaries were tortuous, varied in diameter, and contained multiple microaneurysms ranging in size from 25 to 100 μm. Additionally, cylindrical dilations on capillaries were also seen in these mice. Some of these dilations appeared to be caused by localized capillary wall distensions. However, both light microscopy and transmission electron microscopy revealed enhanced endothelial cellularity at several dilated locations, showing that microaneurysm development contained a component of endothelial cell proliferation [80].

Pdgfrβ$^{-/-}$

The second model of pericyte deficiency targeted the *Pdgfrβ* gene (receptor for PDGFβ) of pericytes. Similarly, these null mutant mice (Pdgfrβ$^{-/-}$) were also embryonic lethal with hemorrhagic, thrombocytopenic, and severely anemic phenotypes. They had defective kidney glomeruli because they lacked mesangial cells of kidney [65]. On the other hand, Pdgfrβ$^{+/-}$ mice had a partial knock-out, presented with 27%-35% pericyte loss, and were viable [81,82]. Zlokovic's group investigated the effect of pericyte loss and suggested two parallel pathways leading to brain vascular injury by utilizing Pdgfrβ$^{+/-}$ mice. The first pathway shows that brain microcirculation is disrupted in those mice, resulting in diminished brain capillary perfusion, cerebral blood flow, and neurovascular coupling, leading to chronic perfusion stress and hypoxia. In the second path, due to BBB breakdown is associated with the accumulation of serum proteins and several vasculotoxic and/or neurotoxic macromolecules in the brain, ultimately leading to secondary neuronal degenerative changes. They showed that age-dependent vascular damage in pericyte-deficient mice precedes degenerative neuronal changes, learning and memory impairment, and the neuroinflammatory response [83]. Lastly, another group reported aberrant cerebral blood flow. Nevertheless, they did not observe apparent structural and functional changes in microvascular structure and reactivity as other researchers did [81].

Pdgfβ$^{ret/ret}$

The third model of pericyte deficiency was created by Lindblom et al. studied in the laboratory of Christer Betsholtz, who had the seminal model discussed above. This time, instead of deleting a major functional portion of PDGFβ protein, they targeted only the retention motive of the protein by insertion of loxP-flanked PGK-neo cassette into intron 5 and a premature translation stop codon/HindIII site into exon 6 of the *Pdgfβ* gene in mouse embryonic stem (ES) cells. As a result, PDGF-B binding to heparan sulfate Proteoglycans was disrupted in the progeny (Pdgfβ$^{ret/ret}$). In this Pdgfβ$^{ret/ret}$ model, the animals were viable with loss of pericyte recruitment (26 % less coverage[50]) to the micro vessels. The effects of PDGFβ retention motive deletion and consequent poor pericyte recruitment to micro vessel walls exhibited severe retinal

deterioration, glomerulosclerosis, and proteinuria[84]. Further, they analyzed the integrity of BBB by testing the passage of a set of traces through the BBB, namely azo dye Evans's blue, fluorescent dye cadaverine Alexa Fluor-555, fluorescently labeled albumin, 70 kDa dextran, and IgG. To use as a control group, they have created a rescue transgenic mouse for Pdgfβ$^{-/-}$ null mutant mice, which are complemented by one or two copies of a conditionally silent human *Pdgfβ* transgene targeted to the Rosa26 locus and activated by endothelial Cre recombinase (hemizygous R26P$^{+/0}$ or homozygous R26P$^{+/+}$ mice). They observed that the Pdgfβ$^{ret/ret}$ has the most BBB leakage compared to R26P$^{+/0}$ with 40% pericyte coverage where R26P$^{+/+}$ rescue mice did not show leakage for those tracers[50]. In another study, investigating the neuroimmune functions of pericytes, Torok et al. showed that in Pdgfβ$^{ret/ret}$ mice, loss of pericytes triggers the upregulation of ICAM1 and VCAM1, and this alteration facilitates the infiltration of the immune cells into the CNS parenchyma in the default state and causes even more exaggerated infiltration in EAE induced mice. They also observed ataxia symptoms with unprecedented lesions in the cerebellum in EAE mice[85].

Pdgfrβ$^{F7/F7}$

Another study investigated the role of PDGFRβ by creating point mutations in the tyrosine-binding sites for signal transduction molecules (Src, Grb2, PI3K, RasGAP, SHP-2, PLCγ). They have tested the combination of mutated alleles for pericyte coverage, F7 allele mutants (Pdgfrβ$^{F7/F7}$), heaving the 7 point mutations in binding sites for all transduction proteins, had less pericyte coverage (~65% pericyte loss) than other mutant alleles and the most severe vascular pathologies[82]. In 2010, Daneman et al. investigated the role of pericytes for the BBB formation by using Pdgfrβ$^{F7/F7}$ and Pdgfrβ$^{F7/-}$ (obtained by crossing with Pdgfrβ$^{+/-}$) mice and demonstrated that pericytes regulate functional aspects of the BBB, including the formation of tight junctions and vesicle trafficking in CNS endothelial cells. Moreover, they found that pericytes do not induce BBB-specific gene expression in CNS endothelial cells but instead inhibit the expression of molecules that increase vascular permeability and CNS immune cell infiltration[52]. Later, another group also reported increased Blood-Spinal Cord Barrier (BSCB) to 350Da, 40,000 Da, and 150,000 Da fluorescent vascular tracers in cervical, thoracic, and lumbar regions. They also observed diminished endothelial zonula

occludens-1 (ZO-1) and occludin tight junction protein expression in this Pdgfrβ$^{F7/F7}$mice. They concluded that increased BSCB permeability-related accumulation of cytotoxic fibrin and thrombin leads to motor neuron loss [86]. Using Pdgfrβ$^{F7/F7}$ mice, pericyte deficiency has also been linked to white matter structural integrity and functions because pericyte degeneration results in toxic fibrin leakage and blood flow reduction. Consequently, they suggested that a toxic environment and decreased blood flow triggers myelin, axon, and oligodendrocyte loss[87].

Tie1Cre^{+}; Pdgfβ$^{+/-}$ (endothelial-specific *Pdgfβ* ablation)

In 2001, the Betsholtz group created an endothelial-specific *Pdgfβ* ablation that managed to escape the pre-natal death as opposed to the case in *Pdgfβ* and *Pdgfrβ* null mutants. They floxed the exon 3 of the *Pdgfβ* (Pdgfβ$^{flox/flox}$), which encodes a significant part of the protein. Then, they crossed their Pdgfβ$^{+/-}$ mice with Tie1Cre mice [88], which expresses Cre-recombinase under the endothelial-specific Tie1 gene promoter control. The resultant practical progeny was Tie1Cre^{+}; Pdgfβ$^{+/-}$ mice, and then they subsequently crossed these mice with Pdgfβ$^{flox/flox}$ mice to get Pdgfβ$^{lox/-}$ mice. Their model has exhibited inter-and intra-individual variation of pericyte density. If the CNS pericyte ablation was more than 50%, the mice showed irregular microvessel diameter, microaneurysms, and increased vascular regression. On the other hand, the mutants having less than 50% pericyte coverage reduction displayed an increase of abnormal vessels in their retinas[89]. They further investigated the abnormalities caused by endothelial-specific PDGFβ ablation and found that mutants developed organ defects such as cardiac, placental, and renal abnormalities as in the null mutants. The only advantage of their model was that these mice survived into adulthood, but they had persistent pathologies, specifically brain microhemorrhages, focal astrogliosis, and granulous kidney abnormalities [90].

All the pericyte deficient models listed above provided valuable insight into pericyte function in both steady-state and pathological conditions. Pericyte insufficiency brings forth a variety of anatomical malformations and functional abnormalities in the CNS and throughout the body. The formation, development, and maintenance of a healthy and functional BBB require proper pericyte function for the lifespan of the organism. As an outcome, animal models with pericyte deficiency suffer

from vascular abnormalities giving rise to cerebral blood flow dysregulations and BBB leakage starting from the embryonic stage and protracting into adulthood. These phenotypes may lead to theoretical conjecture if these mice are used in combination with other disease models (e.g., EAE, ischemic stroke, CSD, etc.) involving similar pathologies.

1.3 Multiple Sclerosis

Multiple sclerosis (MS) is a chronic, inflammatory (immune-mediated), demyelinating autoimmune disease of the central nervous system (CNS). It is characterized by the destruction of myelin sheaths and underlying axons and resultant neurodegeneration. It is a common, life-long disorder of young people (peak age at 20s-30s). A total of 2.8 million people is estimated to live with MS [91]. The prevalence (number of cases per 100.000 people) of MS is highest in Northern America with 164.6 cases, 127 cases in Western Europe, and 91.1 cases in Australasia [92]. The prevalence changes depending on the geography, decreasing from poles to the equator. Even though vitamin D deficiency was attributed to the increased risk of MS, the exact reason why this geographical variance exists is still debatable [93]. Another variance factor in the prevalence of the disease is sex; MS is more common in a woman than a man, with a ratio of 2:1. Other than these factors, family inheritance, history of other autoimmune diseases, and race (white-colored North Europeans having more risk than the Asians and the Africans) are also the risk factors for MS [94].

The neuroinflammation of the CNS in MS manifests itself as inflammatory lesions called plaques seen in the Magnetic Resonance Images of the diseased brain and the spinal cord. Depending on which area of CNS has active inflammatory plaques, the symptoms of the disease could show variability among the patients [95]. Nonetheless, the main symptoms of the disease could be generalized as numbness and tingling, muscle spasms and weakness, mobility problems, pain, fatigue, bladder problems, and vision problems [96] (Figure 2). Cognitive and emotional changes also could be observed in MS patients[97].

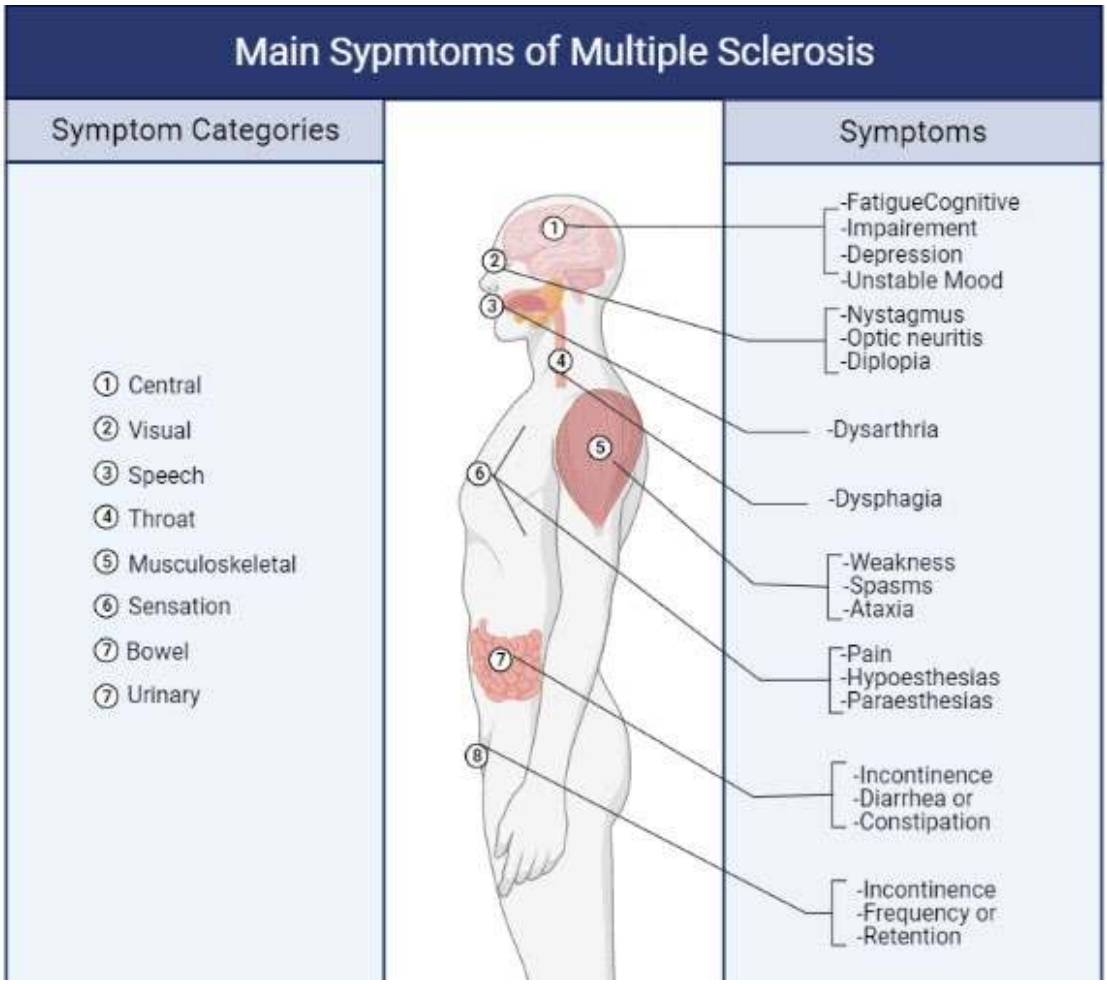

Figure 2. Main Symptoms of Multiple Sclerosis

The main symptom categories that might be experienced in MS patients are the left side of the figure. The type of symptoms of those regions was detailed on the right side of the figure. Adopted from [98].

MS is categorized depending on the patterns of clinical presentation of the disease (Figure 3). Among these clinical presentations, the most common type is Relapsing-Remitting MS (RRMS), affecting around 90% of MS patients [99]. In RRMS, patients experience repeated acute episodes of neurological dysfunction (Relapses) with short or long periods of clinical symptom withdrawal (Remissions). These remissions could be as a complete or partial recovery until the next episode. Episode frequency, timing, and severity are not predictable, and these parameters vary among patients with RRMS [100]. Most RRMS patients (around 80%) convert into another type of MS after a few relapses, the Secondary-Progressive MS (SPMS) [101]. In this phase of

the disease, CNS atrophy caused by axonal loss and pertinent decreased brain volume is added to the neurological symptoms. Therefore, the disease burden increases dramatically. The disease continuously progresses at a high rate and without any remissions [102]. Lastly, only 10% of the MS patients have Primary Progressive MS (PPMS), with progressive symptoms starting from the initial onset of the disease and worsening over time instead of sudden relapses [103] [104].

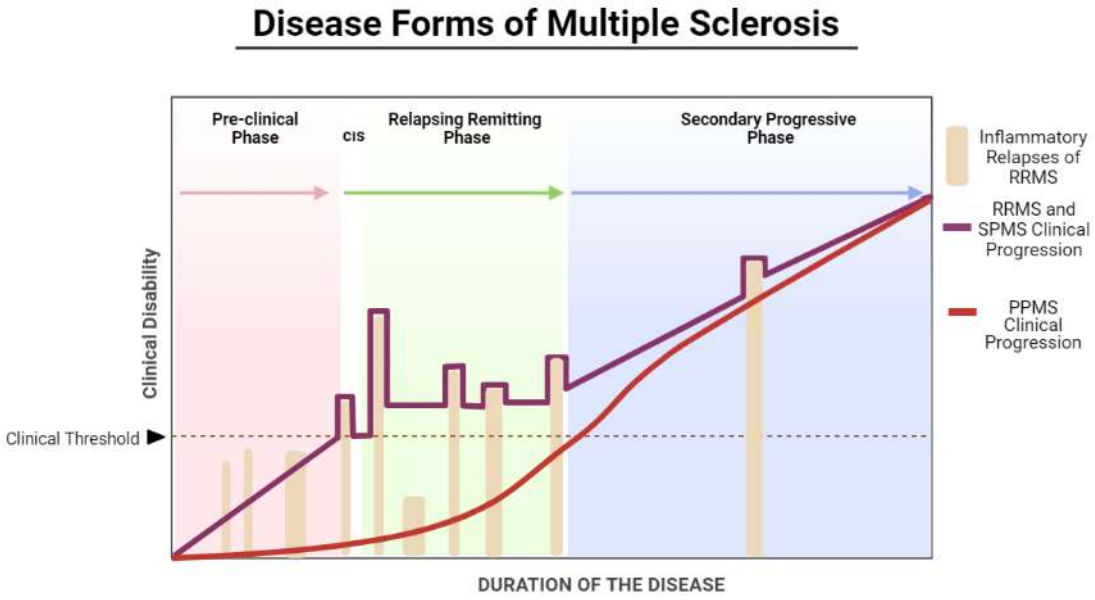

Figure 3. Disease Forms and Progression Types in MS

Three types of MS disease courses are depicted in this figure. The inflammatory relapses of the relapsing-remitting MS (RRMS) are shown by the columns with different lengths (debilitating power) and intervals. Relevant clinical progression and the recovery degrees were drawn with the purple line. In the following phase of RRMS, the secondary progressive MS (SRMS) are shown in the right in continuation of MS attacks of RRMS. On the other hand, the progressive MS form (without any attacks) of primary progressive MS (PPMS) clinical progression is depicted by the red line. Adopted from [94].

1.3.1 Pathogenesis of MS

MS pathology is characterized mainly by BBB breakdown, inflammation, and demyelination. As a consequence of the inflammatory environment, neurotoxicity, hypoxia, and neurodegeneration are the secondary contributors to the pathology in the advanced stages of the disease[105]. Immunopathogenesis of MS is orchestrated by

autoreactive T helper cells (Th1 and Th17 cells) and B cells, whereas cytotoxic T cells and macrophages are the effector cells [106] (Figure 4). The most copious cell type in the inflammatory areas are macrophages and CD8+ cytotoxic T cells. Concordantly, the number of CD8+ T cells is correlated with the degree of axonal degeneration[107]. In addition to above mentioned immune cell types, dendritic cells and microglia also contribute to disease pathogenesis. Collaborated action of all these immune cells results in clinically observable (by MRI) inflammatory lesions of the normal-appearing white matter in the brain and the spinal cord[108,109]. These lesions are called plaques. The triggering factors for the formation of plaques issued by this intense inflammatory response are not clear.

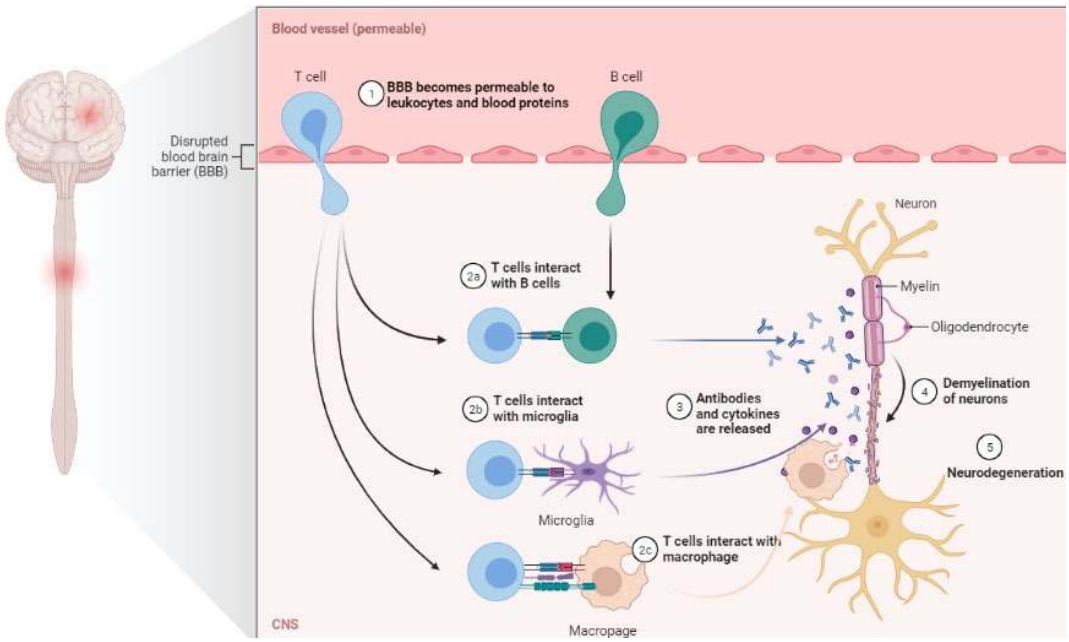

Figure 4. Pathogenesis of MS

In the pathogenesis of MS, encephalitogenic T cells and B cells of the peripheral immune system illegally pass through the BBB into the CNS parenchyma. In the CNS parenchyma, T cells further activate the B cells, microglia, and macrophages. As a result of these activations, chemokines and cytokines are released into the environment. Antibodies are also produced by B cells. By cumulative action of those activated immune cells, the myelin sheats and the oligodendrocytes are attacked, and the signaling of neurons is disrupted. In the end, this inflammatory environment might cause neurodegeneration.

Moreover, it has still been debated if this inflammatory process is initiated peripherally or by CNS itself. There are two models for initiation of MS pathogenesis: CNS Model (inside-out) or Peripheral Model (outside-in) models [110]. In the CNS Model, it is argued that components of immune surveillance of the CNS, monocytes, and neutrophils start the neuroinflammation in the brain. This inflammatory environment triggers BBB breakdown and the recruitment of the T and B cells to the CNS parenchyma [111]. On the other hand, in the peripheral model, T and B cells are initially activated in the secondary lymphoid organs via a variety of possible mechanisms such as activation by a foreign protein that is molecularly like the self-antigen (molecular mimicry) [112], the release of a previously sequestered CNS antigens, miss-activation of the T cells without proper T cell receptor (TCR) stimulation or by the co-expression of TCRs having different specificities [113]. Independently from which disease model is correct; after T cells and B cells start to infiltrate to CNS parenchyma, they get restimulated by the original antigen, and a cascade of events triggers further inflammation [114]. The infiltrated cells release their specific chemokines and cytokines and recruit other immune cell types to the inflamed area. Some anti-inflammatory mechanisms suppress this inflammation at some point of the disease course, and the oligodendrocytes remyelinate the demyelinated axons, and a partial recovery happens [115]. However, the damage could be so severe that the function cannot be regained in some cases [116]. Therefore, it is essential to figure the line of events happening during that inflammatory response and find targets to stop the inflammatory cascade before it is triggered enough to execute their irreversible damages.

1.3.2 Roles of Pericytes in MS

Apart from the abovementioned roles of pericytes for CNS homeostasis, it has been found that pericytes also play a role in the formation and protection of myelin[117]. They secrete molecules that support the transformation of oligodendrocyte precursor cells (OPCs) into mature oligodendrocytes[118]. In addition, it was reported that pericytes strengthen the BBB by increasing the P2X7 receptor expression, which suppresses the inhibition of Claudin5 expression in the EAE model of rats[119]. For these reasons, it is suggested that pericytes could be a therapeutic target for MS disease [118]. In our previous study, we showed that incubation of HBVP cell culture with EAE and progressive MS

sera causes increased ratios of early apoptosis and decreased survival. Furthermore, it has also been shown that the number of brain pericytes is reduced in patients with MS[120,121]. However, the significance of this decrease in the pathology of MS is unknown.

1.4 EAE model

Experimental Allergic Encephalomyelitis (EAE) is the most used CD4+ T cell-mediated autoimmune demyelination model mimicking MS[122]. It successfully represents the pathology of MS in terms of BBB breakdown, inflammation, demyelination, axonal degeneration, and gliosis[123]. The model is characterized by multifocal and mononuclear inflammatory infiltration and concurrent demyelination in the spinal cord white matter and substantial astrocytic, microglial, and macrophage activation in the spinal cord gray matter[124]. Moreover, the model also represents the anti-inflammatory processes along with the remyelination and repair mechanisms in a predictable timeline during the experiments. It is induced by subcutaneous injection of specific encephalitogen myelin proteins with Complete Freund's Adjuvant [125], which contains inactivated *Mycobacterium tuberculosis* particles in oil emulsion. Following the injection of this emulsified combination, two repetitive daily injections of pertussis toxin (PTX) are also required to initiate the peripheral immunization state in EAE [126].

There are various forms of EAE models that can be employed in mice, depending on the type of priming peptide (or protein), animal strains used [126], and the way of immunization. The first protein found to be suitable for EAE induction was Myelin Basic Protein (MBP) (30 % of total myelin proteins). MBP was thought to be the only primary antigen in MS for many years. Then a second protein was identified as encephalitogen, that is, proteolipid protein (PLP). PLP is the most copious myelin protein with a 50% abundance within the myelin proteins[127]. Another protein with little abundance among the myelin protein with a 0.01-0.05% of all proteins, Myelin oligodendrocyte glycoprotein [128], is also capable of inducing CNS-specific autoimmune disease in EAE.

The use of encephalitogenic peptides in different animal strains results in mimicking the various forms of MS disease. For example, $MBP_{84–104}$ peptide presents a monophasic disease course in B19.PL mice, $PLP_{139–151}$ peptide, induces a relapsing-remitting form of MS in SJL mice, and $MOG_{35–55}$ peptide shows a chronic and non-relapsing disease course in C57BL/6 mice [127].

The above-mentioned EAE induction is called active induction, and it is not the only way to induce EAE in mice. There is also another method called adoptive transfer [129,130]. The process of immunization starts by isolating encephalitogenic T cells from actively protein-primed mice and restimulation of these T cells in vitro by specific cytokines and chemokines. Then these T cells are injected into the naïve mice intravenously or intraperitoneally. In this way, the peripheral immunization step of the active EAE model is bypassed, and a more homogenous disease form, induced by the same population of encephalitogenic T cells, is observed in experimental animals[126]. Furthermore, this model gives the researcher the possibility for localizing the T cells during the disease course in vivo by labeling those T cells in vitro prior to administration to the recipient mice [131]. The timing of the initial symptoms of the disease is also more predictable in the adoptive transfer method compared to that in the active transfer method.

Active or adoptive transfer methods or the type of priming protein to be used in the studies could be chosen depending on the experimental question and techniques to be implemented during the model investigations. EAE could also be studied in a variety of species other than rodent strains such as guinea pigs, macaques, rabbits, and rhesus monkeys. The diversity of options that cover most of the pathologies seen in the MS makes the EAE model the most favorable animal model of neuroinflammation thus far [132].

However, as every disease model has its drawbacks, EAE also has some disadvantages and pitfalls that should be carefully considered when translating the experimental results to human MS [133]. First, the pathogenesis of the EAE model differs from the human MS because of the way of peripheral immunization. Relating to the way of induction of EAE, usage of adjuvants that create a harsh immunity response is a majorly criticized issue in this model. Secondly, the disease course in EAE changes depending on the priming peptide or the strain used in the study. This could be turned into an advantage if appropriately chosen, depending on the research question [122]. However, this interchangeability might require additional control groups when using transgenic animals having mixed backgrounds or when comparisons are made related to the antigen type. Most of the strains, including the prevalently used C57BL/6 mice, show a monophasic chronic disease course; however, in human MS, the most frequently

seen disease course is RRMS. EAE also differs from human MS in terms of the location of lesions. In EAE, the lesions are restricted to the spinal cord, while in human MS, brain inflammation overcomes the spinal cord inflammation. Lastly, interspecies immune differences between rodents and humans could be misleading when translating the EAE results to human MS. Despite all these disadvantages, EAE experiments have been a significant source for understanding MS disease and targeted drug discoveries to the day [134].

1.5 Hypothesis and Aims

Pericytes are indispensable members of BBB. They have a variety of critical roles for the homeostasis of CNS and proper functioning of the neurovascular coupling. Correspondingly, they are players in the pathogenesis/pathology of several neurological disorders such as Alzheimer's disease, CADASIL, ischemic stroke, glioblastoma multiforme, diabetic retinopathy, etc. [5,18,41,135,136]. To this day, many transgenic animal models have been used to study the function of pericytes in health and various diseases. These models were mostly focused on transgenic manipulation aiming at imposing loss of function in pericyte signaling. Because of the fact that the pericytes are required for healthy and functional BBB formation, development, and maintenance, these inherently pericyte deficient mice already happen to have vascular malformations and BBB malfunction. Therefore, the lack of proper pericyte function during the development adversely affects the animal's general health, mainly in terms of BBB breakdown-resulted toxicity and cerebral blood flow dysregulation. This condition could mislead the researchers when implementing disease models (e.g., EAE model, ischemic stroke, CSD, etc.) using those mice because the models are developed in an already problematic biological environment. Distinguishing the effect of developmental pericyte deficiency itself from the contribution of pericytes to the pathogenesis of the utilized disease models is a precarious task, especially for the pathologies involving loss of BBB integrity and vascular malfunctioning such as in the MS disease. Despite this drawback, well-characterized complete or partial knock-out models of pericyte signaling components have provided significant insight into the function of pericytes in both health and disease conditions [137]. Heretofore, by using these models, it has been shown that pericyte deficiency has detrimental effects on the brain by leading to white matter injury and causing inflammation, brought about by fibrin leakage [138]. Pericyte deficiency has also been shown to cause neurovascular uncoupling resulting in limited oxygen supply to the brain and leading to neurodegeneration [139]. In the light of these findings, we hypothesized that pericytes might have a protective role in neuroinflammation.

In this thesis project**,** we sought to investigate the role of pericytes in multiple sclerosis pathogenesis by using the combination of *in vivo* inducible pericyte deficiency and neuroinflammation models. However, to be able to effectively and as naturally as possible mimic the neuroinflammation pathogenesis in pericyte deficient mice, we needed first to innovate an inducible pericyte ablation model which could be established in adult life. Consequently, the mice would be intact from possible pericyte loss-related vascular side effects during embryonic development and postnatal maturation into adulthood. For our new generation pericyte ablation model, instead of targeting the signaling pathways of the pericytes as in the models utilized thus far, we directly aimed to eliminate the pericyte cells themselves by manipulating their cell-type-specific genes to induce diphtheria toxin expression by pericyte-specific Cre recombinase activity. Subsequently, in our new generation inducible pericyte ablation mouse model, we utilized the EAE model of MS-like neuroinflammation to shed light on their roles in MS pathogenesis.

As a summary, our aims in this thesis project were:

1. Creating an inducible pericyte ablation model of adult mice
2. Investigating the role of pericytes in neuroinflammation by using our new generation pericyte ablation model

Our hypothesis was that pericytes might have a protective role in neuroinflammation.

CHAPTER 2

2 MATERIALS AND METHODS

2.1 Ablation of Pericytes by using Transgenic Animals

To create our inducible pericyte ablation model, we used the CreER-LoxP system. In this system, the loxP floxed sequences are removed from the genome in the presence of the tamoxifen-activated Cre Recombinase-Estrogen receptor fusion protein (CreER). Precisely, mice from 2 different lines, which are PDGFRβ-P2A-CreER$^{+/-}$ (JAX Mice, 030201) and Rosa26-DTA176$^{+/+}$ (JAX Mice, 010527), were crossed to get the time and cell type-dependent pericyte ablation. PDGFRβ-P2A-CreER transgenic mice have a CreER expression under the control of the *Pdgfrβ* promoter. The mating partner of these mice, Rosa26-DTA176, has a diphtheria toxin (DTA176) gene expression under the control of a constitutive ROSA promoter. Rosa26-DTA176 mice also have a loxP floxed stop gene upstream of the DTA176 gene (Figure 5). Therefore, even though the DTA176 protein is expressed in all the cells of the animals, it cannot be translated into a functional protein because there is a stop codon upstream of the DTA176 mRNA sequence. However, this stop codon would be excised from the genome in case there is a Cre Recombinase activity in the cells. Therefore, only in the cells that could express the CreER, in our case, *Pdgfrβ*-positive cells would express a functional diphtheria toxin protein. As a result, *Pdgfrβ*-positive cells, including pericytes, would be ablated due to the cell-specific, intrinsic expression of DTA upon tamoxifen injection.

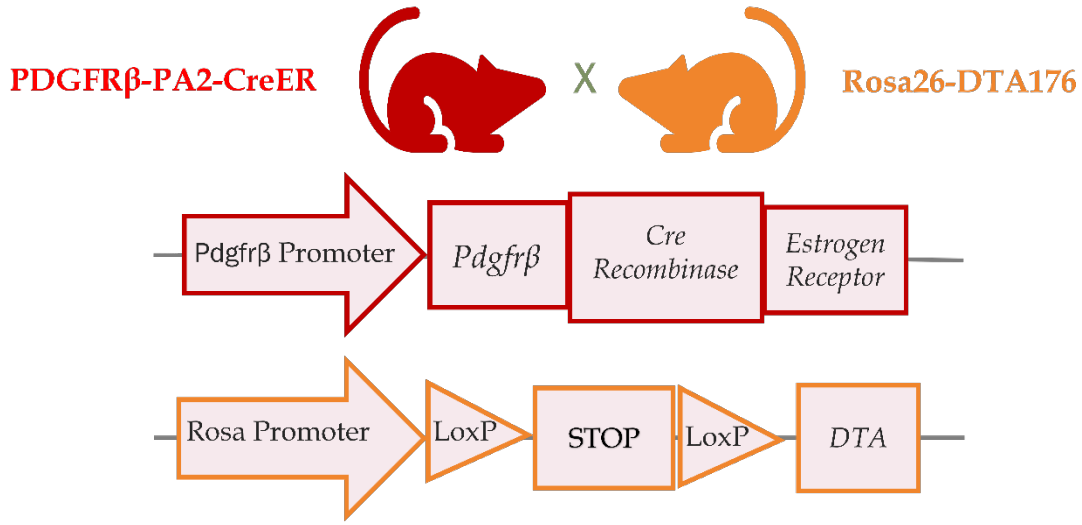

Figure 5. Transgenic Alleles of the Acute Pericyte Ablation model

Pdgfrβ-P2A-CreER animal expresses the Cre Recombinase-Estrogen receptor fusion protein under the control of *Pdgfrβ* promoter as seen in the upper allele. In the bottom allele, the transgenes of Rosa26-DTA176 animal were shown as Diphtheria toxin is added with an upstream LoxP floxed stop codon to be expressed under the control of Rosa promoter. The expression of the DTA gene creates a functional translation product only after the removal of the loxP floxed stop codon by the action of Cre Recombinase.

2.1.1 Genotyping

PDGFRβ-P2A-CreER (030201, Jackson Laboratory) mice and Rosa26-DTA176 (010527, Jackson Laboratory) were mated to create our pericyte ablation transgenic line. Rosa26-DTA176 is homogenously expressing the attenuated diphtheria toxin, DTA176. Therefore, it does not require any genotyping. However, the CreER complex is expressed heterogeneously in the PDGFRβ-P2A-CreER line. Thus, theoretically, only half of the progeny expresses CreER according to the Mendelian rules. To determine CreER positive progeny, tail polymerase chain reaction (PCR) was conducted. First, DNA isolation from the tails was performed using the Zymo Quick DNA Miniprep kit (Cat. No: D4069). Then, PCR was conducted with the genomic DNA to amplify the Cre gene as a tested product and the *Pdgfrβ* gene as an internal

positive control (Table 3). To visualize the genotyping results, PCR products were run on 1.5 % agarose gel (Figure 6).

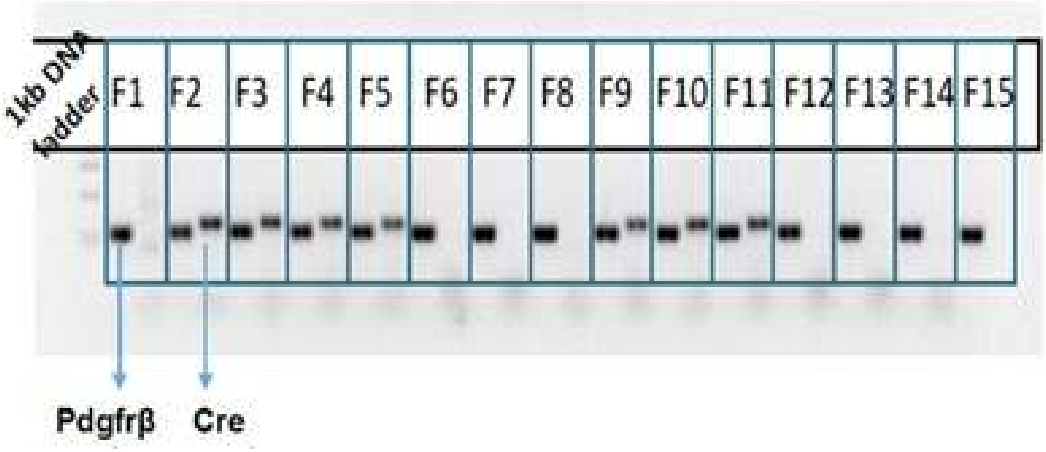

Figure 6. An example image of DNA electrophoresis results of genotyping

The letter F represents the sex of the animal as female, and the numbers represent the IDs of the animals. Each animal has two PCR products. The first one is produced by the internal control primers, resulting in the replication of the *Pdgfrβ* gene. The second lane is a product of primers designed to replicate the Cre Recombinase gene if it exists. The first lane functions as the internal positive control to ensure technical reliability, while the second lane gives the result about the heterogeneous existence of the Cre Recombinase gene.

Table 3. List of Primers used in Genotyping

PDGFRβ-Cre/ Forward	CCA CCT TGA ATG AAG TCA ACA C
PDGFRβ-Cre/ WT Reverse	AGC TTG TGG CAG TGT AGC TG
PDGFRβ-Cre/ Mutant Reverse	ACA TGT CCA TCA GGT TCT TGC

2.1.2 Tamoxifen administration

Tamoxifen is dissolved in corn oil at a stock concentration of 10 mg/ml and intraperitoneally injected to each group at a dosage of 100 mg tamoxifen/kg body weight for consecutive two days, three days, or five days depending on their group. As

a result of tamoxifen administration as an estrogen receptor agonist, transfer of the cytoplasm resident CreER complex to the nucleus was achieved, and Cre recombinase could execute its function of exciting cleaving of the LoxP floxed genomic sequence (Figure 7). In our model, the stop codon expressing transgenic sequence in front of the DTA176 transgene was removed. Subsequently, the expression of the toxin, DTA176, started, and the Pdgfrβ positive cells went into apoptosis.

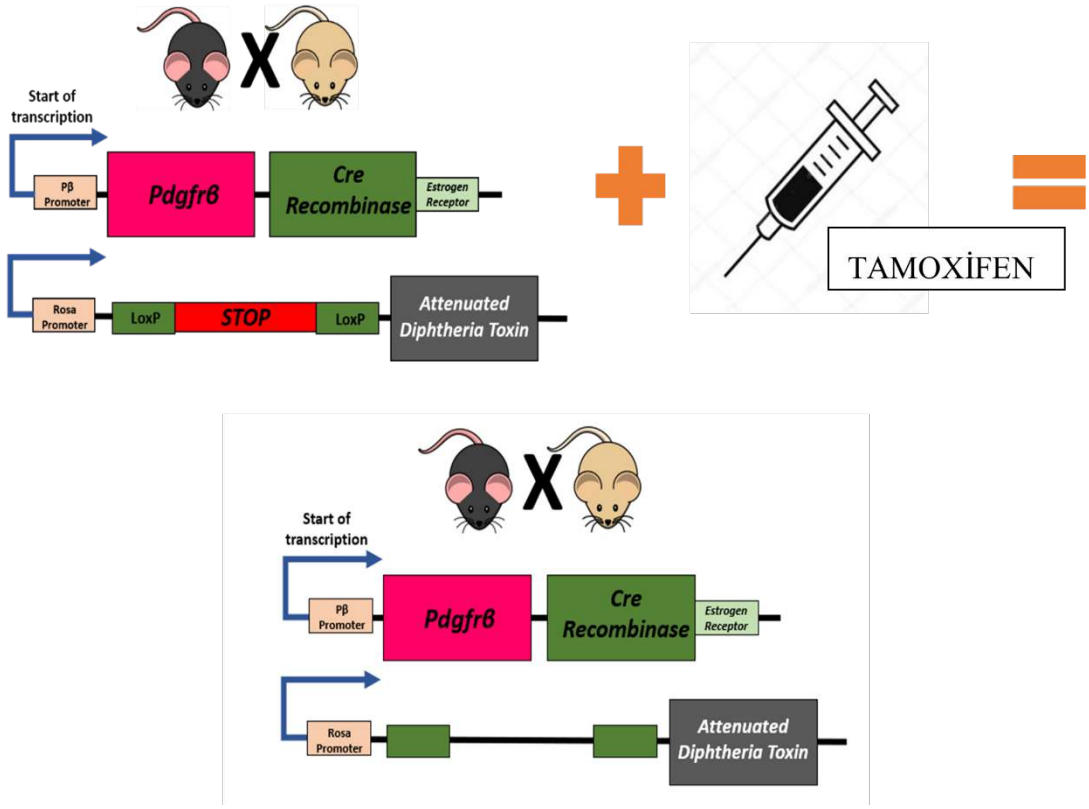

Figure 7. The effect of tamoxifen administration on the transgenic alleles of the acute pericyte ablation model

The tamoxifen administration to our pericyte ablation model animals as an estrogen receptor agonist enables the cytoplasm stuck Cre Recombinase-Estrogen receptor fusion protein to be transported to the nucleus. Then the Cre Recombinase can execute its function of removing the LoxP floxed sequence, the stop codon in our model. Therefore, the DTA gene, depicted as the Attenuated Diphtheria Toxin in the figure, can be translated into a functional protein. As a final result, Diphtheria toxin kills the *Pdgfrβ* positive cells.

2.2 Experimental Plan for the Characterization of Pericyte Ablation Model

8-16 weeks old female and male adult mice were age-matched to Cre (+) experimental and Cre (-) control groups. I had three different experimental/ control groups as each group takes different repeats of tamoxifen administration as 5, 3, and 2 consecutive days. Additionally, every dosage group is divided into two groups depending on the termination time as at Day 15 and Day 60. Each experimental group contained six mice, while each control group had four mice. Their weight data was collected for 15 days (for the acute pericyte ablation group) or 60 days (for the chronic pericyte ablation group) following the first tamoxifen administration, and they were terminated (Figure 8).

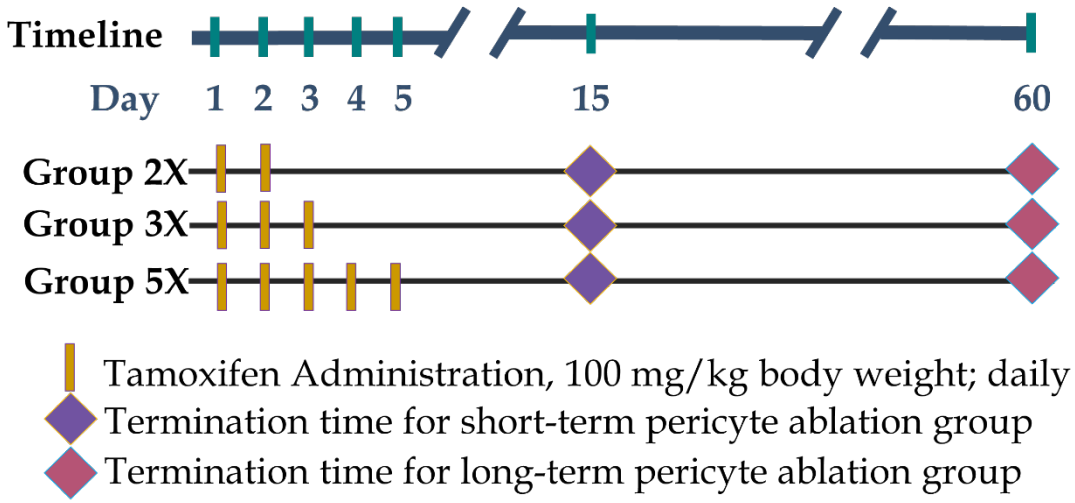

Figure 8. Experimental timing for characterization of the pericyte ablation

The First line shows the timeline of the injections and terminations. The yellow sticks demonstrated repetitive tamoxifen injections, and each dosage group was shown in a different line as Group 2X, Group 3X, and Group 5X. The purple diamond symbol represents the termination time for the acute pericyte ablation at Day15. The green diamond symbol represents the termination time for the chronic pericyte ablation group at Day60.

2.3 Fixation by Cardiac Perfusion

Mice were anesthetized by using overdose ketamine/xylazine anesthesia. After sedation, a toe-pinch reflex was checked to ensure complete sedation was achieved before any procedures were started. The mice were cut open below the diaphragm, and the rib cages were cut on the lateral edges to reveal the heart. A 31-gauge needle connected to a pumping perfusion machine was inserted into the heart's left ventricle, and the right atrium was cut to allow the circulated solution to leave the body. First, the animals were perfused with PBS until all the blood in the body was discarded. Secondly, 4% Paraformaldehyde (PFA) is perfused through the body till the mouse is fully fixed and rigidified. The brain and spinal cord were dissected, and the tissues were post-fixated for two days in 4 % PFA. Then, they were processed for the immunohistochemical assays. The n numbers for the characterization experiments are given in Table 4.

Table 4. Number of the animals used for the immunostaining experiments of the inducible pericyte ablation characterization

n	MALE							FEMALE						
	15 Days			60 Days				15 Days			60 Days			
	2X	3X	5X	2X	3X	5X	TOTAL	2X	3X	5X	2X	3X	5X	TOTAL
Cre^{+} $DTA176^{+}$ (Pericyte Ablated)	4	4	4	4	4	4	24	4	4	4	4	4	4	24
Cre^{-} $DTA176^{+}$ (Control)	2	2	2	2	2	2	12	2	2	2	2	2	2	12

2.4 Hematoxylin and Eosin Staining

Before any immunohistochemical staining, the efficiency of fixation and the integrity of tissues were checked by Hematoxylin and Eosin staining. The incubation solutions and the timing were as follows in the stated order:

1. Distilled water 1 minute
2. Mayer's Hemalum solution (Merck, 109249) for 3 minutes
3. running tap water to remove excess staining (around 1 minute)
4. PBS for 5 minutes
5. Eosin Y-alcohol solution (Shandon, 6766007) for 30 seconds
6. running tap water to remove excess staining (~1 minute)
7. PBS for 5 minutes
8. Two changes of 100% ethanol for 2 minutes
9. Two changes of Xylene for 5 minutes

At the end of the incubations, the tissues were mounted with Entellan. The images of the H&E-stained sections were taken by using Light microscopy (Zeiss Primo star 1).

2.5 Immunohistochemistry

After the brain and spinal cord were dissected at the end of the perfusion, the tissues were post-fixed for two days in 4 % PFA. The tissues were equilibrated by gradually increasing by 10%, 20%, and 30% sucrose concentrations in 0.1M phosphate buffer to avoid crystallization during cryopreservation. After they equilibrated to the 30% sucrose solution, the tissues were frozen in the OTC with the help of fluid nitrogen evaporation. Cryopreserved brain tissues were cut into 30-micron free-floating sections, and spinal cord tissues were cut into 20-micron slide mount sections using a cryostat. 4 consecutive sections around 100 microns apart were taken for each sample. For immunofluorescence staining, sections were blocked with (5% NGS, 2% BSA, 0.1% TritonX-100 in DPBS) for 1 hour at room temperature. Then, the sections were incubated with a 1:100 concentration of primary antibody CD13 (MCA2183) overnight at +4 degrees in the blocking solution. After incubation with primary antibodies, sections were washed with DPBS for 5 minutes. Then, the sections were incubated for 2 hours in RT with 1:200 concentration of fluorophore-conjugated secondary antibody (Alexa Fluor 647, ab150159) to detect the pericytes and Dylight 488 conjugated tomato-lectin (DL-1174) to visualize vessels, then washed in DPBS again. All the incubations for the free-floating brain tissues were done with gentle agitation by using a shaker at the rate of ~70 rpm. Slide-mounted spinal cord tissues were encircled by a hydrophobic pap-pen before each step of the protocol. The incubations were done in a steady state. Finally, the sections were mounted by one drop of mounting medium with Hoechst in 1:1 DPBS-Glycerol solution and covered with cover glasses.

2.5.1 Confocal Imaging

4-6 random areas of cortex from non-adjacent, ~100micron apart brain sections with 20X magnification and nine white/gray matter regions with 40X magnification from nine sections from different segments of the spinal cord were quantified imaged and by Leica DMI8 SP8 Confocal Microscopy. 488 nm laser was used to excite Dylight 488-conjugated tomato lectin. The emission was collected through the 500-550 nm detector range, whereas a 633 nm laser was used to excite AF-647, and emission was

collected through 660-720 nm. Then the images were analyzed using ImageJ and MATLAB.

2.5.2 Pericyte Coverage Analysis

For ImageJ analysis, 10-micron thick maximum projection images were obtained for each image. The red channel was used for CD13 (pericyte marker), and the green channel was used for tomato-lectin (vessel marker) staining. Channels were separately converted into 8-bit images and processed to enhance the signal by applying Gaussian Filter (sigma=2). Then the triangle thresholding was performed to generate the masked images (Figure 9). To avoid the background signals and unspecific stains, stains under the size of 50 pixel^2 were removed. Finally, to calculate the pericyte coverage, the ratio of the integrated density of the CD13 was divided by the integrated density of the tomato-lectin signal. These processes were performed automatically without any potential biased manual adjustment using MATLAB Code (see Appendix A. The MATLAB Codes, used for the pericyte Coverage Analysis)

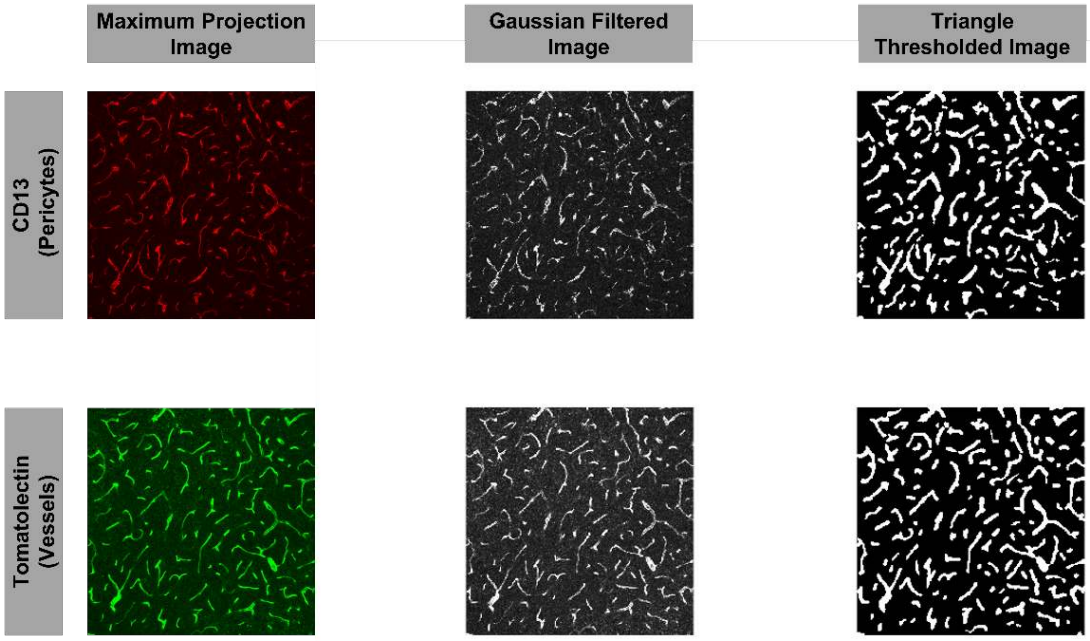

Figure 9. The Images Generated by MATLAB for Pericyte Coverage Analysis

The confocal images of the CD13 stained pericytes (upper panel) and tomato lectin-stained vessels (bottom panel) were processed by MATLAB code by applying Gaussian Filter (sigma=2) shown in the

middle row. Then this image was converted into a Thresholded image by the function of triangle threshold as shown on the right side of the figure.

2.5.3 Analysis of Pericyte Count

Pericyte numbers of the 10um thick z-stack images of the cortex and the spinal cord were counted by the cell counter Plug-in of the ImageJ software. The 2-micron apart z-stacks of the 10 um thick merged images of the Hoechst, CD13 and tomatolectin staining were exported as multipage images. The CD13 staining overlapping with a cell body located on the tomatolectin signal was counted as a pericyte. The counting was done by going back and forth through the multipage to avoid recounting the projections of the counted pericytes. The counter pericyte numbers were normalized into the green area percent to compare different images with each other. All the images that were compared were taken using the same laser intensity settings and the detector ranges.

2.5.4 Analysis of Vessel Morphology

The channel that shows the tomatolectin staining was exported as multipage. Then the maximum projection image was obtained by using Image J. The image type was changed to 8-bit, and the Gaussian Filter (sigma=2) was applied to the image. Then triangle thresholding on a white background was used to mark the vessels. Then the images were masked by creating a binary image to filter out the background staining smaller than 20 inch^2. After the background particle elimination, the masked images (Figure 10) were saved and analyzed in the AngioTool software [1] in terms of Explant area, Vessel area, Vessel Percentage Area, Total Number of Junctions, Junction Density, Total Vessel Length, Average Vessel Length, and Total Number of End Points.

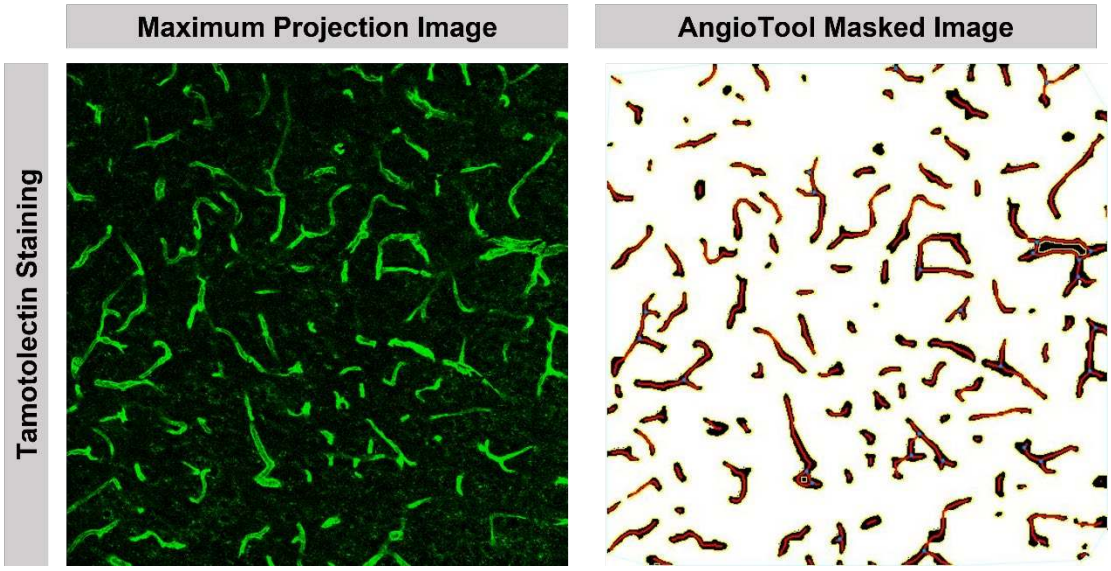

Figure 10. The masked image generated by AngioTool Software for vessel analysis

AngioTool software was used to mask the Tomatolectin-stained vessels. Then, the mask images were analyzed in terms of vessel parameters.

2.6 Real-Time Quantitative Polymerase Chain Reaction (RT-qPCR)

The cortex of the brains was dissected, and RNA of the cortex tissue was extracted by using RNA Miniprep Plus Kit (Zymo Research, R1055) according to the manufacturer's instructions. 500 ng of the extracted RNA was used to generate cDNA by reverse transcription reaction by random primers. RT-qPCR was performed using miScript SYBR® Green PCR Kit (Qiagen, 218073) with LightCycler 480 Instrument (Roche Diagnostics). GAPDH cDNA was amplified as a housekeeping gene, and CT of GAPDH was subtracted from the CT of the target mRNA to find ΔCT value for the target mRNA. Then, the amount of the target mRNA was calculated with the formula of 2-(ΔCT). Experiments were performed three times with three technical replicas.

2.7 Behavioral Tests

Y maze and inverted screen (grip strength) tests were used to investigate spatial recognition memory and motor performance. All the tests were performed one day before the termination of the animals.

2.7.1 Y Maze Spontaneous Alternation Test

The white-colored Y maze setup with the dimensions of 6 cm width, 20 cm depth and 35 cm arm length were used to quantify the spatial recognition memory of the animals (Figure 11). The mice were recorded for 5 minutes after leaving to the middle of the maze. The maze was cleaned with 10 % ethanol and waited to be dried before use between each experiment. The recordings were then watched and manually quantified. When quantifying, each arm was labeled as A, B, and C (Figure 11). The list of the arm entries was written down. A spontaneous alteration was defined as entering all the arms in a row without reentering any previously visited arms. Finally, to calculate the Y maze score, the number of spontaneous alterations was divided into the number of all triads.

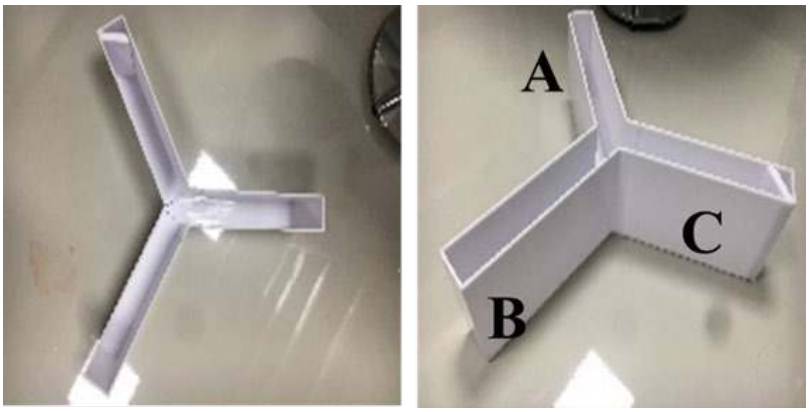

Figure 11. The Y maze set up and example labeling for the quantification

The image of the Y maze setup and its labeling for the quantification process was illustrated.

The Kondziela's Inverted Screen (Grip Strength) Test

The inverted screen test was applied to measure the locomotor activity changes in mice. The mouse was placed in the middle of the 30x30cm sized, 1 mm squared screen (Figure 12). Then, the screen was inverted to force the mouse to grip the wires of the screen. The test was applied three times until the mouse fell or achieved 300 seconds of holding time. The average holding time was compared between the experimental and the control group.

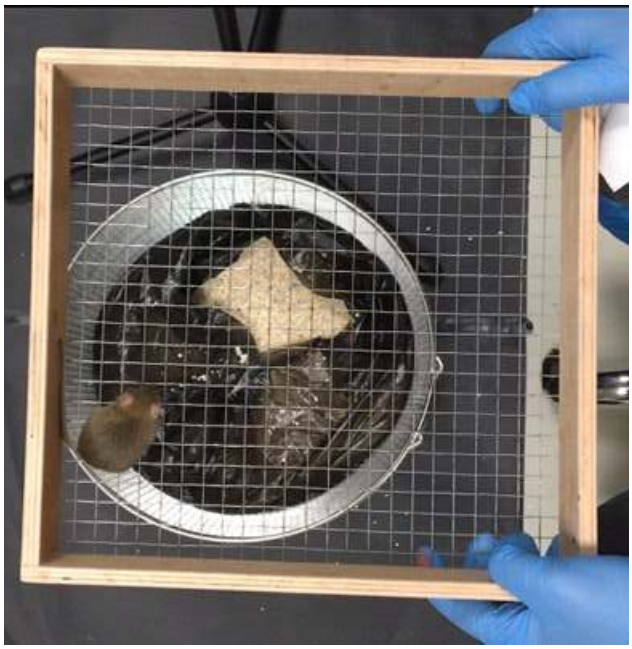

Figure 12. The Kondziela's inverted Screen test setup

The inverted screen test setup is shown before the screen was inverted when the mouse is habituating to the screen.

2.8 Active Experimental Allergic Encephalomyelitis (EAE) model

For the induction of the EAE model, we have used the commercial “Hooke Kits for EAE induction” (EK-2110). Ten days before the application of Hooke Kits for EAE induction, 9-13 weeks old C57BL6/J mice were taken into the procedure care room for acclimatization. Mice were housed randomly as at most five animals in one cage in a climate-controlled procedure care room (22 ± 2 °C) maintained on a 12 h light/dark cycle (7 a.m-7 p.m.) with ad libitum access to food and water throughout the experiment. On the first day of the experiment, 0.1ml of MOG35-55-CFA emulsion/injection was injected subcutaneously into the mice's upper back and lower back. The injections were applied under isoflurane anesthesia (with 1.5 L/min of oxygen flow and 3% of isoflurane vapor). After injections, animals were left to recover in their initial cages. 2-3 hours later, each mouse was intraperitoneally injected with 200ng of PTX in 0.1 ml volume. On Day 1, PTX injections were repeated, and animals were left in their cages undisturbed for a week. From Day 7, animals were weighted and clinically scored according to Hooke Labs EAE Scoring Guide (Table 3Table 6) every other day until Day28 (Figure 13). On Day 28, mice were anesthetized with 0.1ml/10mg bodyweight of 100 mg/ml ketamine and 20 mg/ml xylazine anesthesia cocktail and terminated by cardiac perfusion of DPBS and 4% paraformaldehyde. The brain and spinal cord were removed and further processed for immunohistochemistry staining. Images were acquired by Leica TCS SP8 DLS confocal microscope.

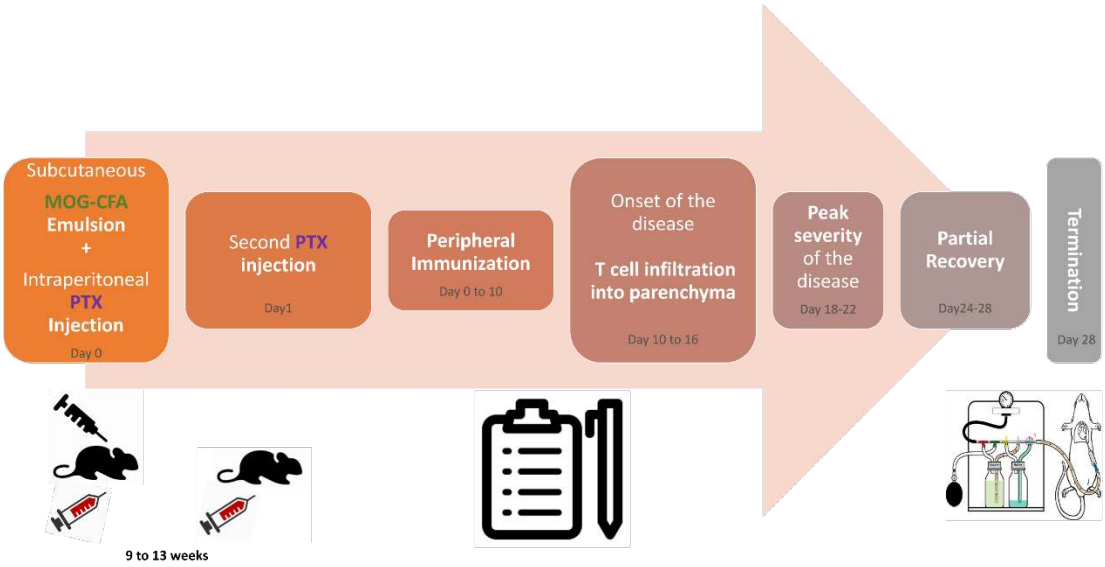

Figure 13. Chronic Experimental Allergic Encephalomyelitis (EAE) model experimental timeline overview

The EAE model starts with the habituation phase one week before the EAE induction day. On Day 0, MOG-CFA emulsion of the Hooke Lab is subcutaneously injected into the animals' upper back and lower back. 2-3 hours after the emulsion injection, the mice have intraperitoneally injected with pertussis toxin (PTX) solution, and the mice were left to rest. The next day, a second PTX injection was done. Then the animals were left without any disturbance for the first which when the peripheral immunization takes place. The animals' weight and clinical scores were evaluated until Day 28, and the animals were terminated.

When the mice were scored for the clinical symptoms of the active EAE model, the questions below were asked and answered to find the correct score:

1. When holding the mice from the tip of the tail:
    a. Is the tail erect?
    b. Is the tip moving?
2. When holding the mice from the base of the tail:
    a. Is there any movement in the tail?
    b. Could the tail make the helicopter-like a turn?
    c. Is the tail dropping over the researcher's finger?
    d. Are the hind legs wide open? Are they close in the middle?
    e. Are the hind legs closed and at one side of the body?

   f. Is the mouse turning the upper body?
3. When the mouse is walking on the grid:
   a. Is any of the legs falling? If yes, are one or both legs falling?
4. When the mouse is walking on the floor:
   a. Can the mouse move?
   b. Is it leaning towards one side? Is it turning towards one side all the time?
   c. Is the mouse have a wobbly walk?
   d. Is the mouse falling during walking?
   e. Are the hind legs dragging? Are the hind legs tripping on the foot? Is tripping or dragging on one leg or both legs?
   f. Are the hind legs paralyzed? If yes, are one leg or both legs paralyzed?
   g. Can the mouse move the hind legs forward of the hip?
   h. Is the head leaning towards the floor?
   i. Can the mouse use the front legs?
   j. Can the mouse only walk by leaning to the walls of the cage?
   k. Are the hind legs flat on the floor and crawling? Does the mouse have a humpback?
5. When the mouse left to the floor on its back,
   a. Can it turn itself to the normal walking position?
6. Is the mouse alert to the stimuli from outside?
7. Can the mouse eat when given food?

Table 5. Mouse EAE Scoring Guide of Hooke Labs

0	No obvious changes in motor function compared to non-immunized mice. When picked up by base of tail, the tail has tension and is erect. Hind legs are usually spread apart. When the mouse is walking, there is no gait or head tilting.
0.5	Tip of tail is limp. When picked up by base of tail, the tail has tension except for the tip. Muscle straining is felt in the tail, while the tail continues to move.
1.0	Limp tail. When picked up by base of tail, instead of being erect, the whole tail drapes over finger. Hind legs are usually spread apart. No signs of tail movement are observed.
1.5	Limp tail and hind leg inhibition. When picked up by base of tail, the whole tail drapes over finger. When the mouse is dropped on a wire rack, at least one hind leg falls through consistently. Walking is very slightly wobbly.
2.0	Limp tail and weakness of hind legs. When picked up by base of tail, the legs are not spread apart, but held closer together. When the mouse is observed walking, it has a clearly apparent wobbly walk. One foot may have toes dragging, but the other leg has no apparent inhibitions of movement. - OR - Mouse appears to be at score 0.0, but there are obvious signs of head tilting when the walk is observed. The balance is poor.
2.5	Limp tail and dragging of hind legs. Both hind legs have some movement, but both are dragging at the feet (mouse trips on hind feet). - OR - No movement in one leg/completely dragging one leg, but movement in the other leg. - OR - EAE severity appears mild when picked up (as score 0.0-1.5), but there is a strong head tilt that causes the mouse to occasionally fall over.

3.0	Limp tail and almost complete paralysis of hind legs. One or both hind legs are able to paddle, but neither hind leg is able to move forward of the hind hip. - OR - Limp tail with paralysis of one front and one hind leg. - OR - ALL of: ▪ Severe head tilting, ▪ Walking only along the edges of the cage, ▪ Pushing against the cage wall, ▪ Spinning when picked up by base of tail.
3.5	Limp tail and complete paralysis of hind legs. In addition to: Mouse is moving around the cage, but when placed on its side, is unable to right itself. Hind legs are together on one side of body. - OR - Mouse is moving around the cage, but the hind quarters are flat like a pancake, giving the appearance of a hump in the front quarters of the mouse.
4.0	Limp tail, complete hind leg and partial front leg paralysis. Mouse is minimally moving around the cage but appears alert and feeding. Often euthanasia is recommended after the mouse scores 4.0 for 2 days. However, with daily s.c. fluids most C57BL/6 mice may recover to 3.5 or 3.0, while SJL mice may fully recover even if they reach score 4.0 at the peak of disease. When the mouse is euthanized because of severe paralysis, a score of 5.0 is entered for that mouse for the rest of the experiment.
5.0	Mouse is spontaneously rolling in the cage (euthanasia is recommended). - OR - Mouse is found dead due to paralysis. - OR - Mouse is euthanized due to severe paralysis.
	In the recovery stage:
0.0	When held by the base of tail, tail is somewhat "hooked" and rigid, but tail makes complete rotations around the body axis ("helicopter"). Mouse is healthy. No signs of wobbling.
0.5	Mouse appears normal but tail is "hooked" and rigid. Tail does not make complete rotations around the body axis ("helicopter"). Mouse is healthy. No signs of wobbling.

3.0	Mouse is found on its side (as described for score 3.5 above), but there is excessive hind leg movement. Mouse cannot walk. - OR - Mouse has a wobbly walk (as described for score 2.5 above), and is unable to take more than two steps without falling on its side. The mouse is unable to right itself. - OR - Mouse has poor movement in the hind legs (as described for score 2.5 above), and has partial front leg paralysis evidenced by head held lower than normal and mouse's inability to right itself when placed on its side.
All other scores	Subtract 0.5 from the score of all mice with either a rigid, "hooked" tail or pedaling of hind legs.

2.9 Experimental plan for the combination of pericyte ablation and EAE

Pericyte ablation transgenic mouse line (PDGFRβ-PA2-CreER$^{+/-}$; Rosa26-DTA176$^{+/+}$ mice) and the wild type C57BL6/J lines were habituated to the isolated experimental room ten days before the experiment. Animals were hosted in that secluded room for experimentation and only be handled by me to avoid any possible stress triggers. Both races of animals were separated into groups according to different injections that they will be administered (shown in Table 6). Then each experimental group was divided into three subgroups as technical replicates (for details see Appendix G. Experimental Plan for the combination of inducible pericyte ablation and EAE). 2 constitutive doses of Tamoxifen administration were done as described above, and the EAE injections were done on Day 15 of the first tamoxifen injection. Previously optimized "Hooke Kits for EAE induction" (EK-2110) were used for the EAE induction. The mice were weighed and scored for 28 days and terminated (Figure 14).

Table 6. Experiment groups for the pericyte ablation and EAE combination

Cre Recombinase Existence	MOG	Tamoxifen	Race	Aim	n
+	+	+	Mixed	To see the effect of the pericyte ablation on the EAE model *(The main transgenic experimental group)*	10
+	-	+	Mixed	To see the effect of the pericyte ablation on the EAE model *(the main transgenic control group)*	10
-	+	+	Mixed	To see the effect of the race on the EAE model	8
-	+	-	Mixed	To see the effect of tamoxifen administration on the EAE model	5
	+	+	Wild Type	To see the effect of tamoxifen administration on the EAE model	3
	+	-	Wild Type	To check the efficiency of the Hooke Lab MOG-EAE kits *(WT- experimental group)*	13
	-	-	Wild Type	To see the regular weight changes and possible side effects of the vehicle solutions *(WT- Control Group)*	5

Figure 14. Experimental timeline of the Inducible Pericyte Ablation and EAE Model Combination

The process of animal research starts with a long time of preparation. The animals were mated and genotyped, and because the progeny of one homogenous and one heterogenous transgenic mouse race were mated, this process lasted as long as three months. At the start of any experiment, the animals were habituated to the experimental room for at least a week. Then on Day 0 and Day1, intraperitoneal tamoxifen injections were done. Animals were rested for 15 days for pericyte ablation to take place, and the weights of the animals were recorded every two days. On Day 15, the EAE model was induced, and animals were evaluated for weight changes and the clinical scores for the following 28 days until Day 43 of the experimental plan. Then the animals were terminated at Day 43.

CHAPTER 3

3 RESULTS

3.1 Weight changes of the mice after 5, 3, or 2 consecutive days of tamoxifen administration

In this thesis, a new tamoxifen-inducible pericyte ablation model was introduced. Since the model has not been used before, characterization of the model and the optimization of the tamoxifen dosage were necessary to be able to combine the model with other experimental models or manipulations. To characterize the pericyte ablated animals, the effectiveness of different repetitive doses of Tamoxifen (2,3 and 5 consecutive daily injections) was investigated. The general health of the animals was observed by monitoring the weight changes during 15 days as a short-term and 60 days as a long-term period.

3.1.1 Pericyte ablation effect on weight in short-term (15 Days)

Five consecutive days of tamoxifen administration

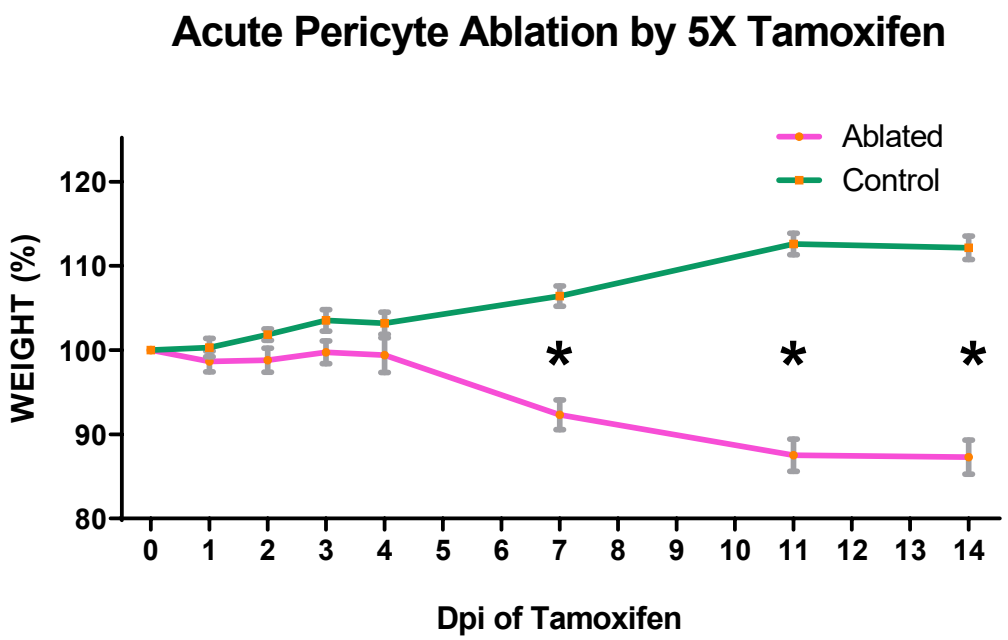

Figure 15. The change in the weights of pericyte ablated and control mice within 15 days after the tamoxifen injection for five consecutive days

The x-axis shows the days post tamoxifen injection, in the first four days and ones in a week, the weight of the animals recorded. The gap between the weights of the pericyte ablated and the control group was significant after the first week. The significance was assessed by the 2-way ANOVA repeated measures multiple comparison test. n=14 for the pericyte ablated group and n=11 for the control group. $p<0.0001$ for the data point at Day7,11 and 14. The error bars show the SEM.

A dramatic difference between the weights of the pericyte ablated (PDGFRβ-PA2-CreER^{+}; Rosa26-DTA176^{+}) and the control mice (PDGFRβ-PA2-CreER^{-}; Rosa26-DTA176^{+}) injected with five doses of tamoxifen was observed starting from the 4th day after the first tamoxifen administration. This difference was significant after the first week of the experiment, with a weight difference of 12% (from 92 to 106% $p<0.0001$). The gap between the weight graphs of the pericyte ablated and control mice

increasingly continued until Day 15 and reached the point where pericyte ablated mice lost an average of 10% of their weight. In comparison, the control mice increase their weight in the range of average growth of 10%. More specifically, the weight percentage difference between the pericyte ablated and control mice was 25% (from 87.3% to 112.2%, $p<0.0001$) at Day15 (Figure 15). This amount of weight loss indicates that the animal is not healthy, and most of the time, animals that lose 10-15 % of their body weight should be terminated for ethical reasons. Therefore, there is no long-term data for the mice which were given tamoxifen for five consecutive days since five repeats of tamoxifen administration were fatal, and most of this group did not survive even for the short-term experimental time, 15 days. However, even though the remaining animal numbers were low at the end of the experiment, some further analyses were done using those animals. It was certain that this dosage of tamoxifen is not suitable for studying the effect of the pericyte ablation on another model. However, it may be used to study the impact of pericyte loss directly.

Three consecutive days of tamoxifen administration

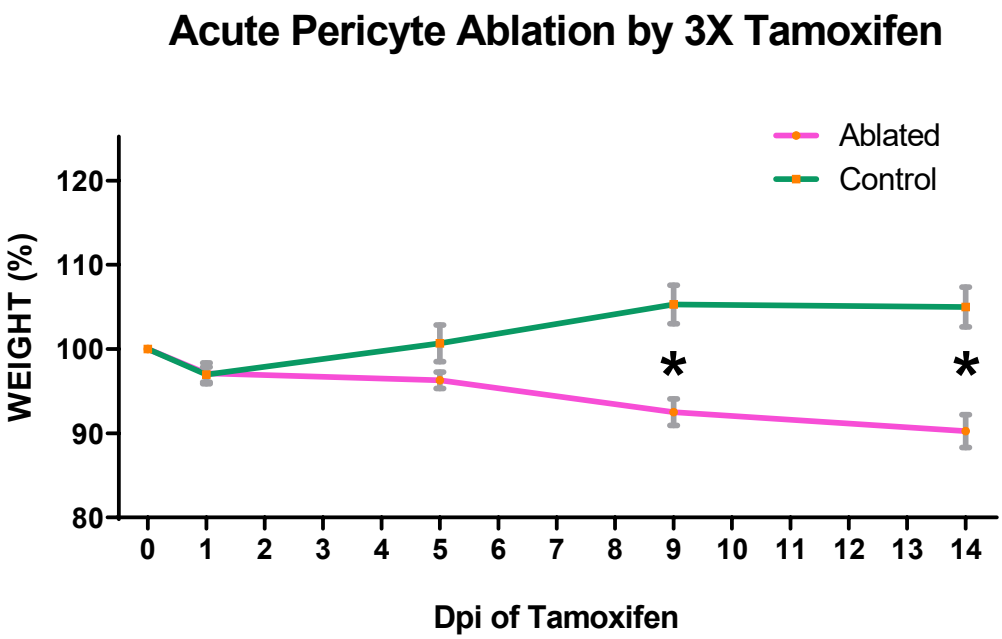

Figure 16. The change in the weights of pericyte ablated and control mice within 15 days after the tamoxifen injection for three consecutive days

The weights of the animals have been recorded ones in a week. The gap between the weights of the pericyte ablated and the control group was significant after the first week. The significance was assessed by the 2-way ANOVA repeated measures multiple comparison test. n=21 for the pericyte ablated group and n=12 for the control group. $p<0.0001$ for the data point at Day 9, $p<0.0001$ at Day 14. The error bars show the SEM.

In the case of 3 repetitive dosages of tamoxifen is given to the pericyte ablation group (PDGFRβ-PA2-CreER^{+}; Rosa26-DTA176^{+}) and the control group (PDGFRβ-PA2-CreER^{-}; Rosa26-DTA176^{+}), there was again a significant weight difference of pericyte ablated and the control mice starting around the first week (13% from 92% to 105%, $p<0.0001$) This weight difference continued towards to the 15th day (15% from 90% to 105%, $p<0.0001$) (Figure 16). As in the case of 5 doses of tamoxifen injected pericyte ablation group, three doses of tamoxifen injected animals also lost the health-threatening and ethically critical level of weight.

Two consecutive days of tamoxifen administration

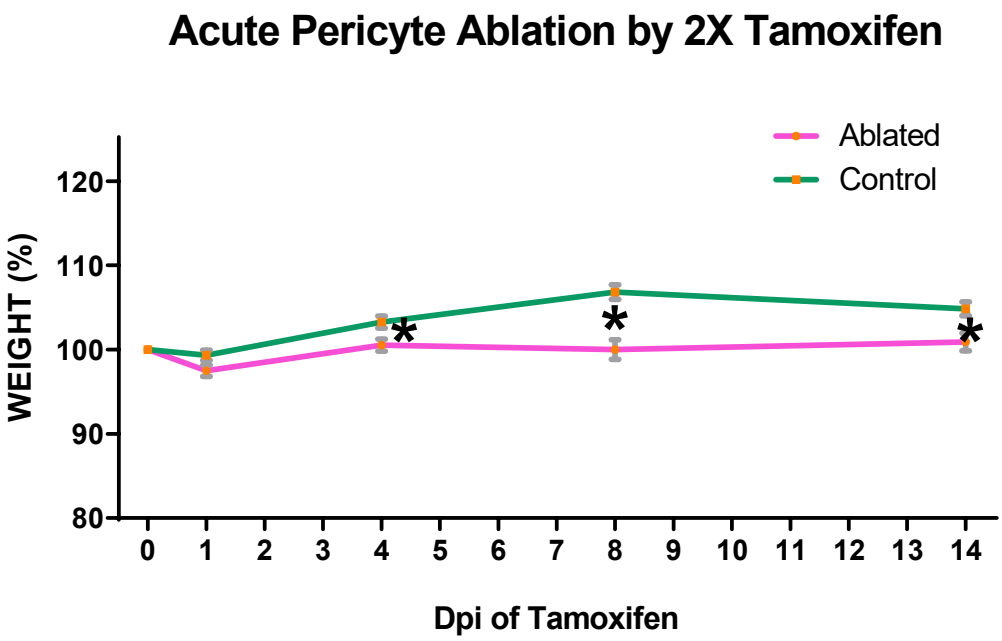

Figure 17. The change in the weights of pericyte ablated and control mice within 15 days after the tamoxifen injection for two consecutive days

The weights of the animals have been recorded ones in a week. The gap between the weights of the pericyte ablated and the control group was significant after the first week. The significance was assessed by the 2-way ANOVA repeated measures multiple comparison test. n=22 for the pericyte ablated group and n=12 for the control group. p= 0.0136 for the data point at Day 4, p<0.0001 at Day 8 and p= 0.0066 at Day 14. The error bars show the SEM.

As a last effective dosage of tamoxifen, two repetitive doses of tamoxifen were given for consecutive days to another group of pericyte ablation and the control group. In this dosage, a slight gap between the pericyte ablated mice and the control mice weight graphs was also observed with the peak at the 8th day (6% from 100% to 106%, p<0.0001). The weight gap decreased at the 15th day (4% from100% to 104%, p=0.0066) (Figure 17). Since the weight loss is not as much as the other doses, two times of tamoxifen dosage, in case it happens to be effective enough in terms of pericyte

ablation, was the most feasible dosage for the further experiments that would potentially cause more weight loss for those animals.

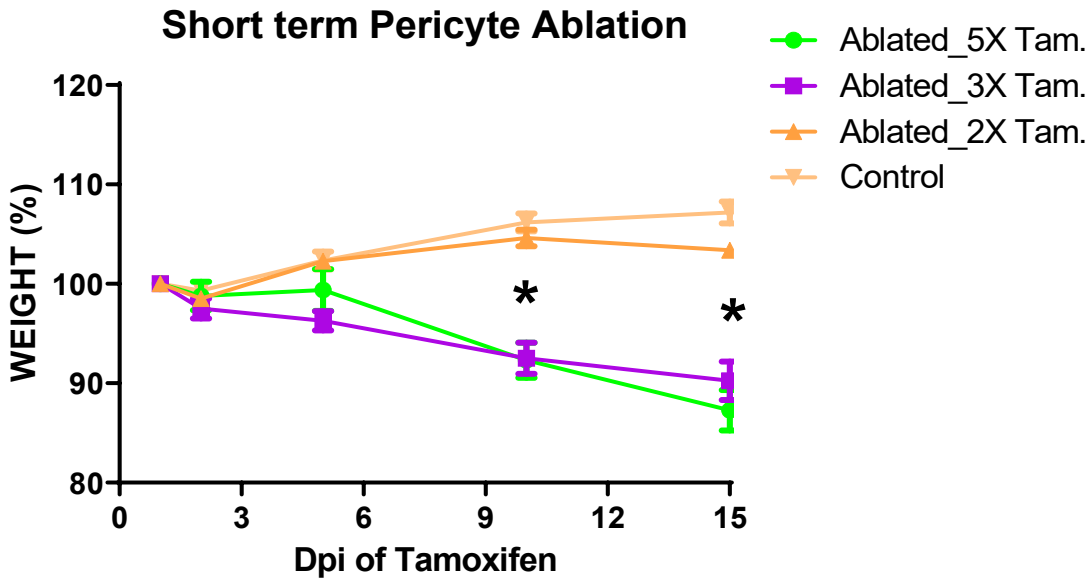

Figure 18. Comparison of the weight changes caused by pericyte ablation with different repetitive doses of tamoxifen in short term

The difference between the two doses of tamoxifen and both 3 and 5 doses of tamoxifen-induced weight loss was significant. The stars represent the significance of the 2X Tamoxifen weight graph to both other doses, $p<0.0001$ for Day10 and Day15. The statistical analyses were done by using 2-way ANOVA repeated measures multiple comparison test. n=14 for 5X Tamoxifen group, n=21 for 3X Tamoxifen group, n= 22 for the 2X Tamoxifen group and n=35 for all doses merged control group. The details of the statistical analysis are given in Appendix C. Statistical Analysis Results of Figure 18. The error bars show the SEM.

When the weight loss levels of different doses of tamoxifen were compared with each other, the 3 and 5 repetitive dosages of tamoxifen-induced pericyte ablation resulted in significantly more weight loss than the two doses of tamoxifen-induced pericyte ablation ($p<0.0001$ for each data point) (Figure 18).

3.1.2 Pericyte ablation effect on weight in the long term (60 Days)

To observe the impact of pericyte ablation in the long-term, both three doses and two doses of tamoxifen groups were also analyzed for the 60 days in terms of weight differences between the pericyte ablated and the control group.

Three consecutive days of tamoxifen administration

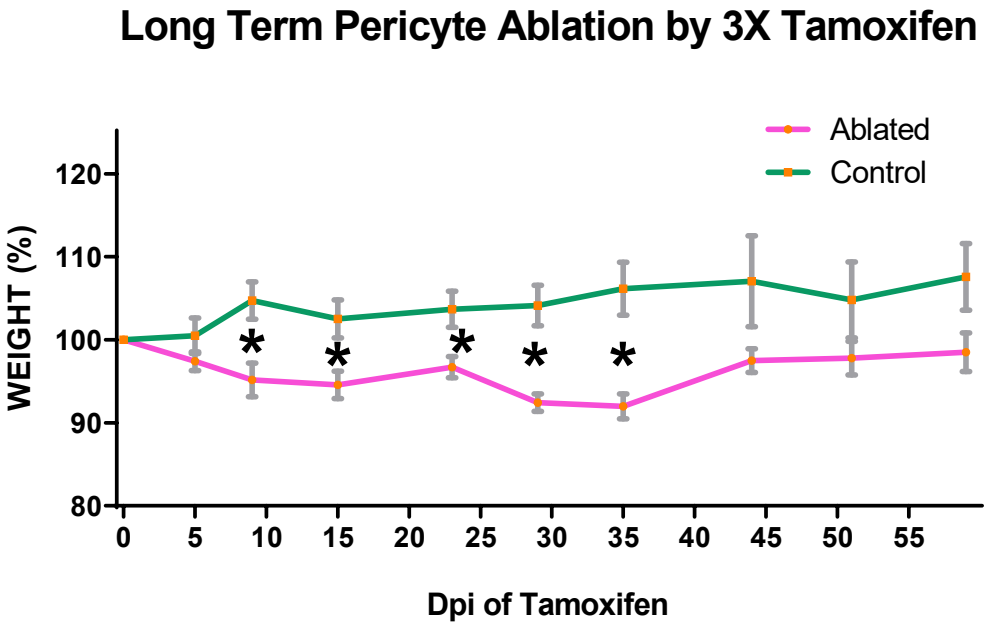

Figure 19. The change in the weights of pericyte ablated and control mice within 60 days after the tamoxifen injection for three consecutive days

The weights of the animals have been recorded ones in a week. The gap between the weights of the pericyte ablated and the control group was significant after the first week. This difference continued until the 60th day of the experiment, with a non-significant difference after around the 40th day. The significance was assessed by the 2-way ANOVA repeated measures multiple comparison test. n=10 for the pericyte ablated group and n=12 for the control group. p=0.0051 for the data point at Day 9, p= 0.0113 at Day 15, p= 0.0133 at Day 24, p=0.0006 at Day30, p= 0.0011 at Day35. The error bars show the SEM.

When the effect of pericyte ablation by the three doses of tamoxifen administration on the weight graph of the animals in the long term, again a significant

weight difference was observed between the pericyte ablated and the control group. The difference was significant in the time points between the first week and the 5th week after the tamoxifen administration (Figure 19).

Two consecutive days of tamoxifen administration

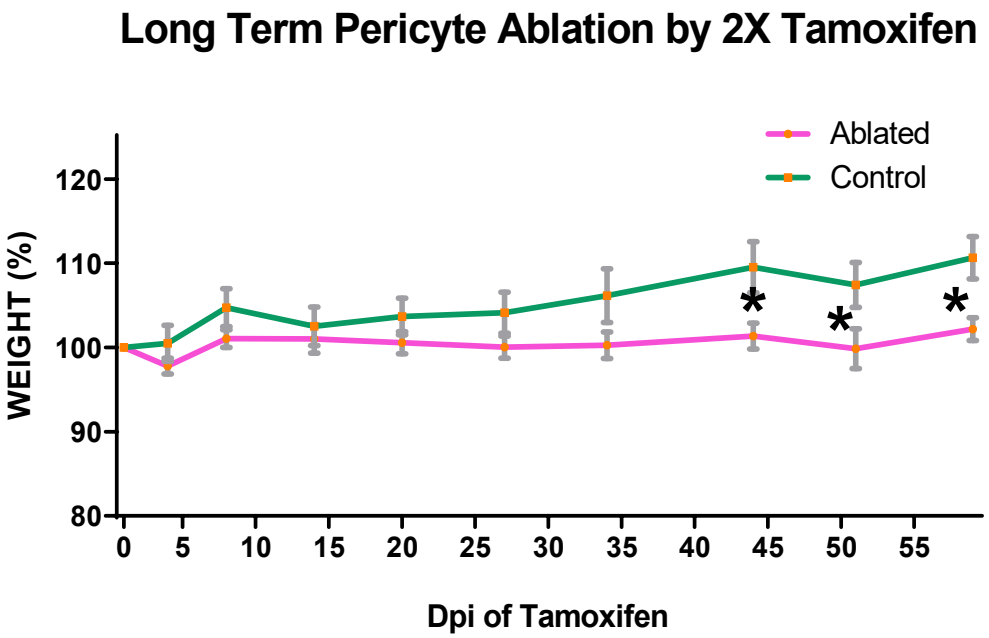

Figure 20. The change in the weights of pericyte ablated and control mice within 60 days after the tamoxifen injection for two consecutive days

The weights of the animals have been recorded ones in a week. The gap between the weights of the pericyte ablated and the control group was significant after around the 45th day. The significance was assessed by the 2-way ANOVA repeated measures multiple comparison test. n=11 for the pericyte ablated group and n=12 for the control group. p= 0.0295 for the data point at Day 44, p= 0.0462 at Day 51, p= 0.0133 at Day 24, p= 0.0092 at Day 59. The error bars show the SEM.

The same long-term weight tracking was also done for the two consecutive days of the tamoxifen injected animals. The results showed no significant difference between the pericyte ablated and the control group until the 45th day of the experiment. Then the significance was consistent throughout the experiment time. As in the short-term weight tracking results, the two times tamoxifen injected animals showed the mildest weight loss pattern in the long-term experiments (Figure 20).

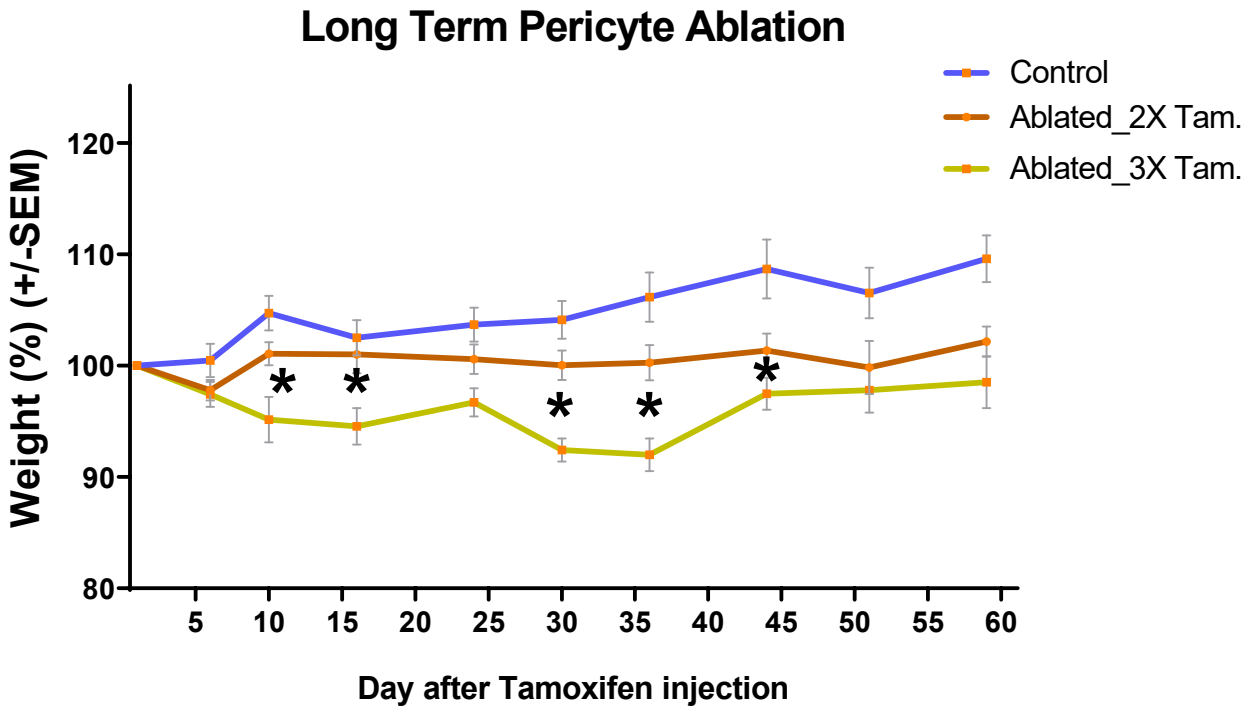

Figure 21. Comparison of the weight changes caused by pericyte ablation with different repetitive doses of tamoxifen in the long term

The difference between the two doses and three doses of tamoxifen-induced weight loss was significant. The stars represent the significance of the weight loss difference between these doses. The statistical analyses were done by using 2-way ANOVA repeated measures multiple comparison test. n=14 for 5X Tamoxifen group, n=10 for 3X Tamoxifen group, n= 12 for the 2X Tamoxifen group and n=25 for all doses merged control group. The details of the statistical analysis are given in Appendix D. Statistical Analysis Results of Figure 21. The error bars show the SEM.

When the long-term weight tracking of all groups was compared to each other, the significant weight loss was consistently continued as in the same dose-dependent trend of the short-term data. Two times tamoxifen injected group showed the mildest pattern in terms of the degree of weight loss, and three times tamoxifen injected group lost significantly more weight than the two times tamoxifen injected group (Figure 21).

3.2 Hematoxylin and Eosin (H&E) staining results

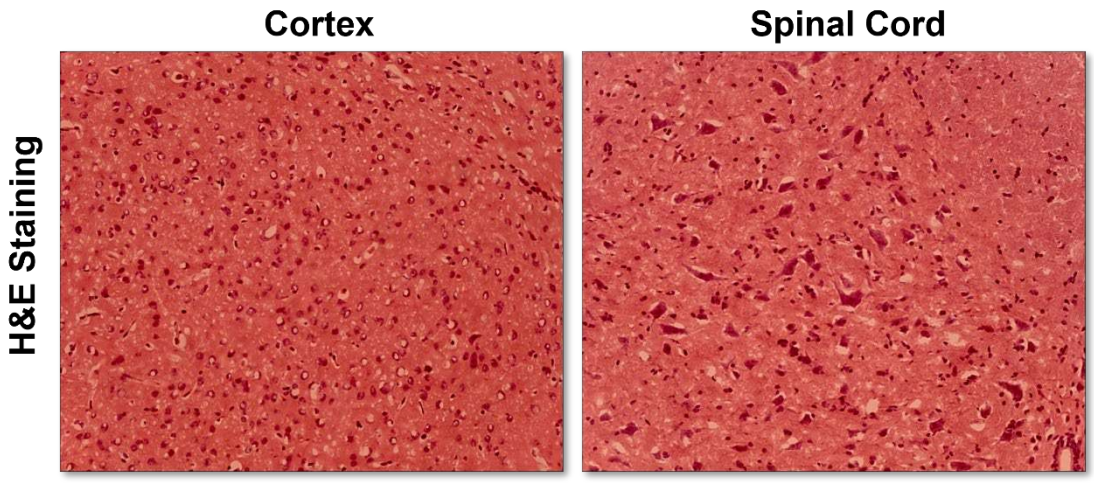

Figure 22. H&E staining of the brain and the spinal cord tissues

Hematoxylin and Eosin staining was performed to ensure the quality of the tissues to be immunostained. The hematoxylin stain is seen as blue/purple in the images, and it stains nuclear components, while eosin is seen as pink stains cytoplasmic components such as collagen fibers, muscle fibers, and elastin. These results show that the tissues were intact and reliable for immunostaining analysis. The cortex image was taken by 5X objective, while the spinal cord images were taken by 10X objective.

The tissue integrity and quality were checked by H&E staining to ensure that the tissues were not harmed during the cryopreservation before the immunohistochemical staining. As seen in Figure 22, the tissues were intact and reliable to proceed with immunohistochemical analysis.

3.3 Confocal image analysis of the inducible pericyte ablation in the cortex and spinal cord

3.3.1 Pericyte Ablation in the cortex

The pericyte coverage data was obtained as a ratio of the integrated signal density of the CD13 signal to the combined signal density of the tomatolectin staining. The effectiveness of the Cre activation and the pericyte ablation was assessed by the degree of decrease in the pericyte coverage.

Pericyte Ablation induced by five repetitive doses of tamoxifen (5X)

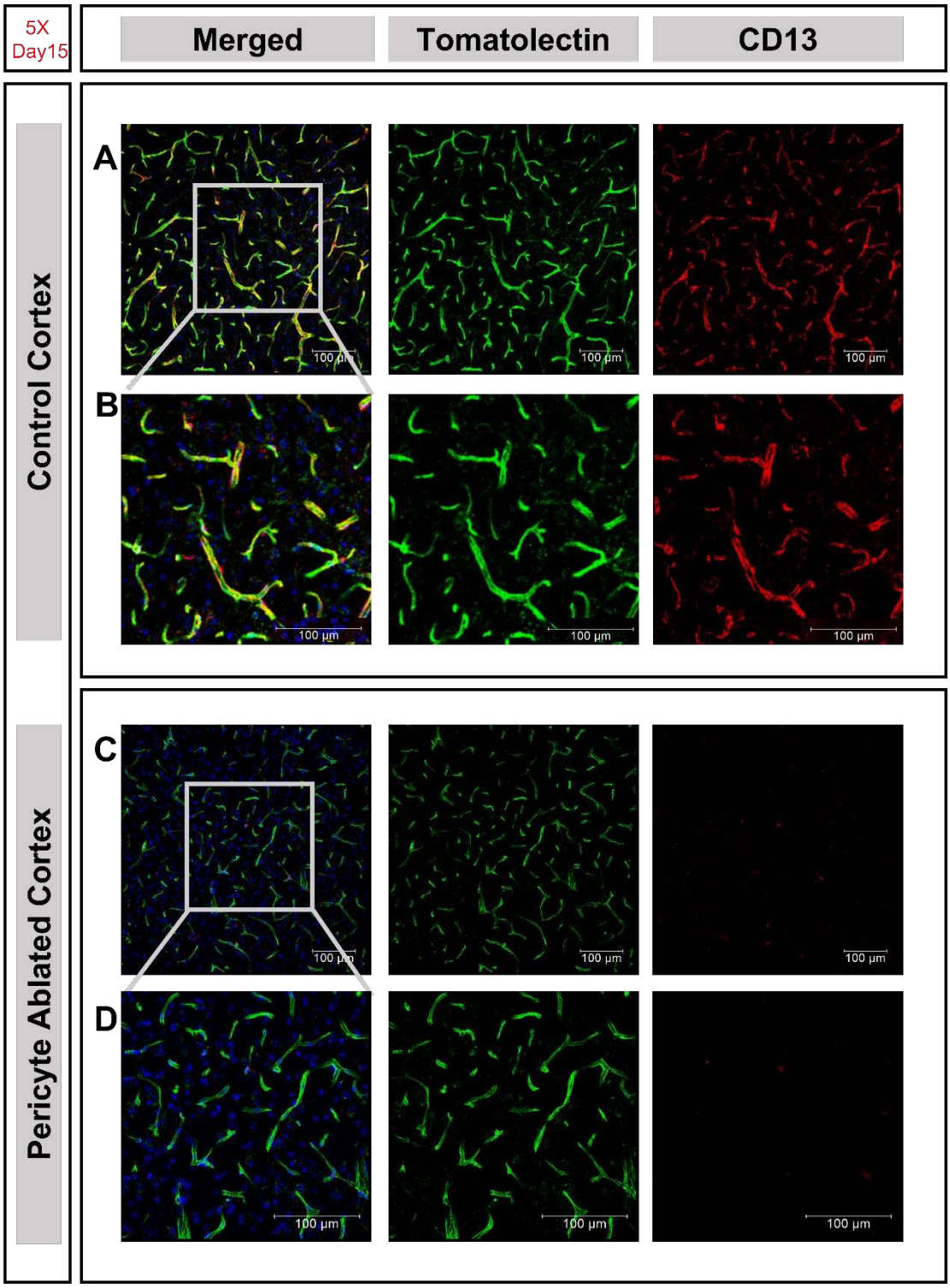

Figure 23. Cortex images of five times tamoxifen injected animals at Day 15

The confocal microscopy images of the CD13 stained pericytes (red) and Tomatolectin stained vessels and merged images with the Hoechst-stained nuclei (blue) are shown for the control group (A and B), and the pericyte ablated group (C and D). A and C were taken using 20X objective, and B and C show the images taken by 2X digital zoom with the same objective. In C and D, the pericyte coverage and the number are decreased compared to the pericyte coverage and the number of the A and B. The scale bars are shown in the right bottom corner of each image as 100µm.

There was a prominent decrease in the pericyte coverage of the five times tamoxifen injected pericyte ablated mice compared to the Cre-negative littermate controls (Figure 23).

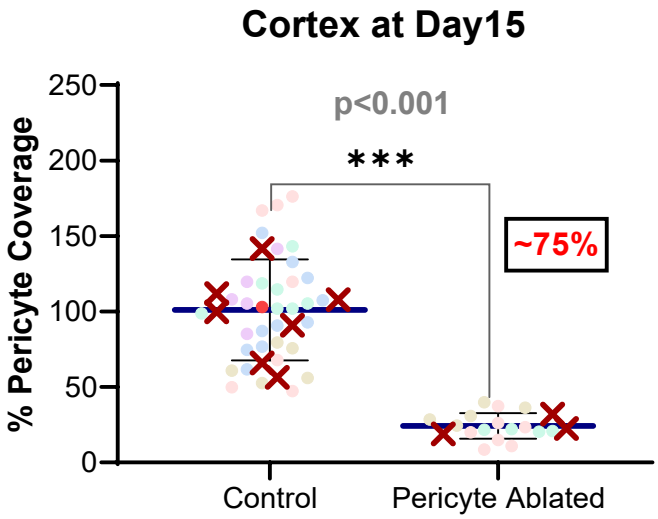

Figure 24. Quantification of the pericyte coverage and number in the cortex for five times tamoxifen injected animals

The confocal images of the cortex were quantified in terms of pericyte coverage (A), and pericyte number (B) were graphed. A shows a 75% reduction in the pericyte coverage in the cortices of the five consecutive days of tamoxifen administered animals after 15 Days. n=3 for the pericyte ablated group and n=7 for the control group. The x symbols on the graphs show the average value for each animal, and the different colors of dots show the pericyte coverage of the individual images of each animal (5-6 images per animal). The values were normalized to the control group average value as a percentage. The

statistical analysis was done by Student's t-test (two-tailed Mann Whitney test). $p<0.001$. The error bars show the SD.

The quantification of 5-6 images from four non-adjacent sections revealed a 75% decrease of pericyte coverage in the cortex of the five times tamoxifen injected pericyte ablated animals (Figure 24). The long-term analysis was not done for the five-time tamoxifen injection group because this dosage of pericyte ablation throughout the body was lethal.

Pericyte Ablation induced by three repetitive doses of tamoxifen (3X)

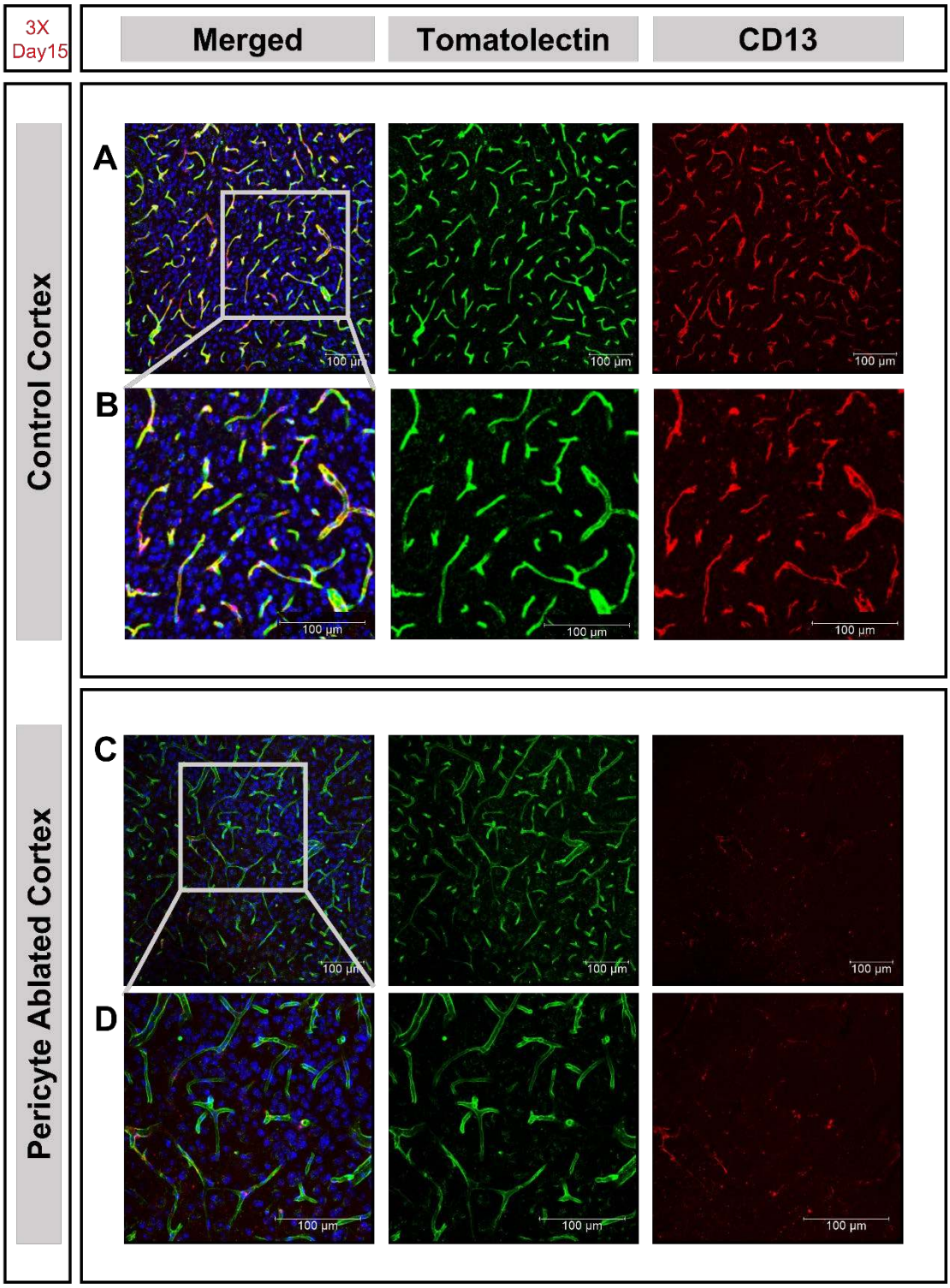

Figure 25. Cortex images of 3 times tamoxifen injected animals at Day 15

The confocal microscopy images of the CD13 stained pericytes (red) and Tomatolectin stained vessels and merged images with the Hoechst-stained nuclei (blue) are shown for the control group (A and B) and the pericyte ablated group (C and D). A and C were taken by using 20X objective, and B and C show the images taken by 2X digital zoom with the same objective. In C and D, the pericyte coverage and the number were decreased compared to the pericyte coverage and the number of the A and B. The scale bars are shown in the right bottom corner of each image as 100μm.

The pericyte coverage analysis was also done for the three doses of tamoxifen injected group. The representative images of the cortex are shown above in Figure 25. A sufficient amount of pericyte ablation was also observed in the three times tamoxifen injected groups.

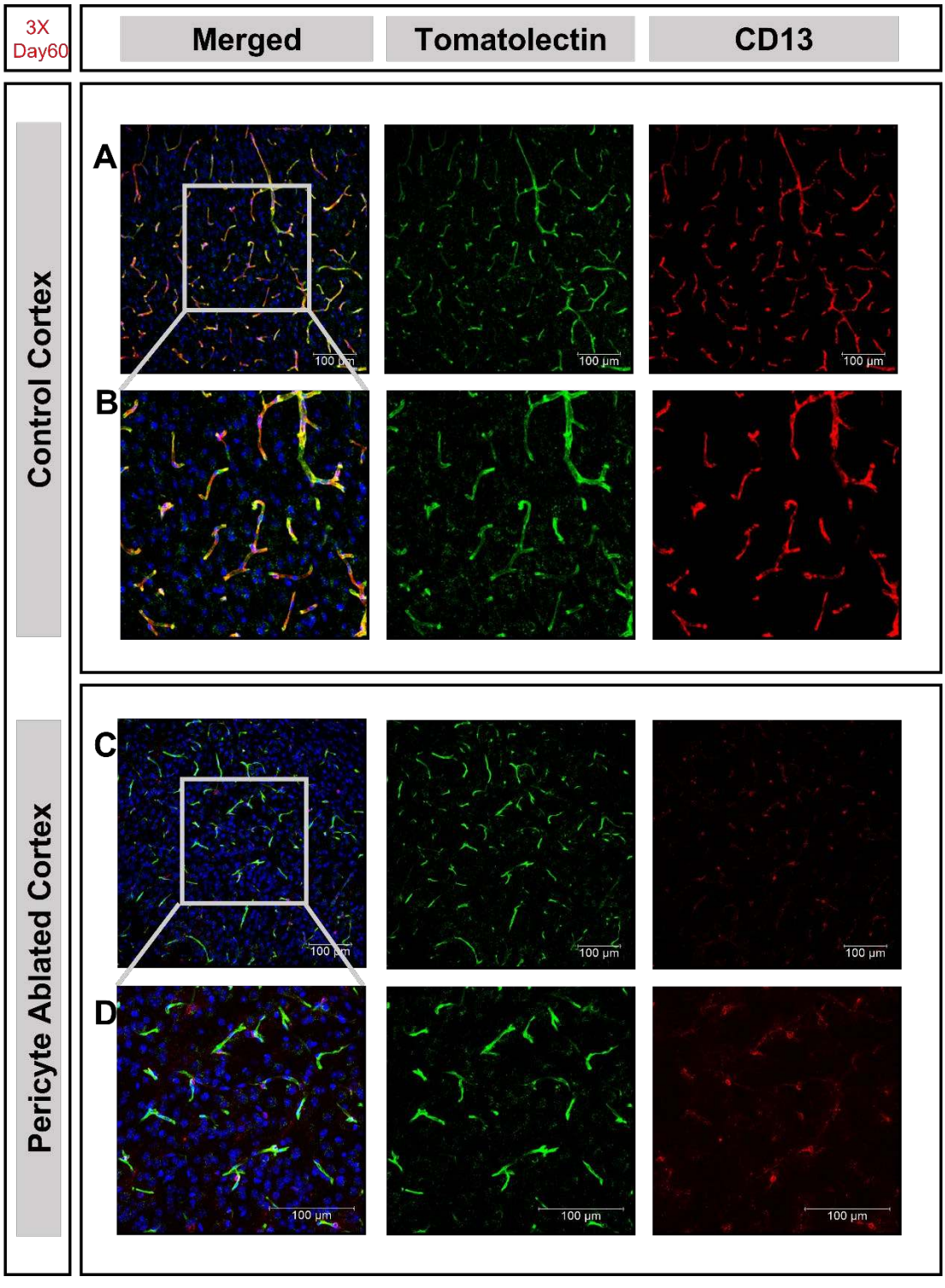

Figure 26. Cortex images of 3 times tamoxifen injected animals at Day 60

The confocal microscopy images of the CD13 stained pericytes (red) and Tomatolectin stained vessels and merged images with the Hoechst-stained nuclei (blue) are shown for the control group (A and B), and the pericyte ablated group (C and D). A and C were taken by using 20X objective, and B and C show the images taken by 2X digital zoom with the same objective. In C and D, the pericyte coverage and the

number are decreased compared to the pericyte coverage and the number of the A and B. The scale bars are shown in the right bottom corner of each image as 100µm.

The decrease in the pericyte coverage was also apparent in the long term for the three times tamoxifen injected pericyte ablation group (Figure 26).

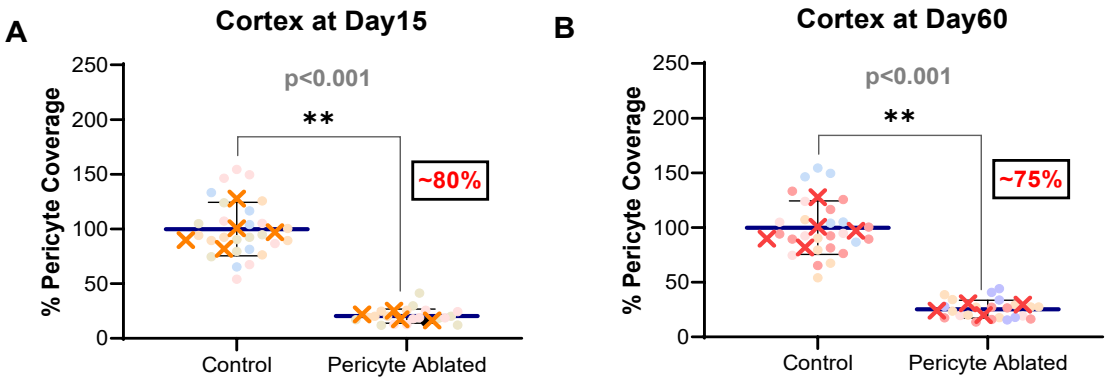

Figure 27. Quantification of the pericyte coverage in the cortex for three times tamoxifen injected animals

The confocal images of the cortex were quantified in terms of pericyte coverage) at both Day 15 (A) and at Day 60 (B) time points. A shows an 80% reduction in the pericyte coverage in the cortices of the three consecutive days of tamoxifen administered animals after 15 Days. In A and B, n=5 for the pericyte ablated group and n=4 for the control group. The x symbols on the graphs show the average value for each animal, and the different colors of dots show the pericyte coverage of the individual images of each animal (5-6 images per animal). The values were normalized to the average value of the control group. The statistical analysis was done by Student's t-test (two-tailed Mann Whitney test). $p<0.001$ for both A and B. The error bars show the SD.

The quantitative analysis of the cortices of the three times tamoxifen injected groups revealed around 80 percent decrease in 15 days (Figure 27 A) and 75 percent decrease in the 60 days (Figure 27 B) after the Cre activation ($p<0.001$).

Pericyte Ablation induced by two repetitive doses of tamoxifen (2X)

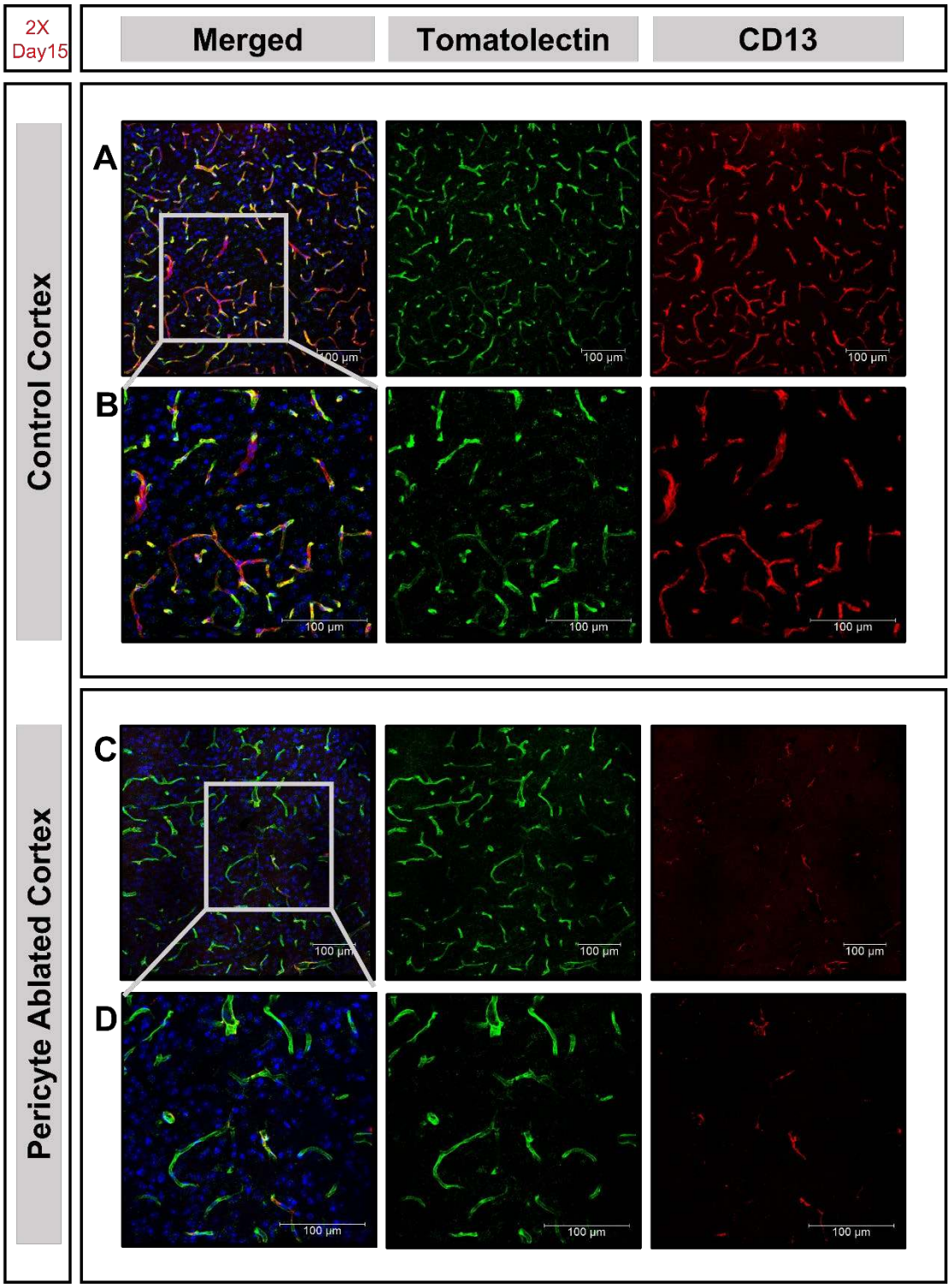

Figure 28. Cortex images of 2 times tamoxifen injected animals at Day 15

The confocal microscopy images of the CD13 stained pericytes (red) and Tomatolectin stained vessels and merged images with the Hoechst-stained nuclei (blue) are shown for the control group (A and B), and the pericyte ablated group (C and D). A and C were taken by using 20X objective, and B and C show the images taken by 2X digital zoom with the same objective. In C and D, the pericyte coverage and the number are decreased compared to the pericyte coverage and the number of the A and B. The scale bars are shown in the right bottom corner of each image as 100μm.

The immunohistochemical analysis of the cortex showed a pronounced decrease of pericyte coverage even in the 15 days post-induction of pericyte ablation with two doses of tamoxifen (Figure 28).

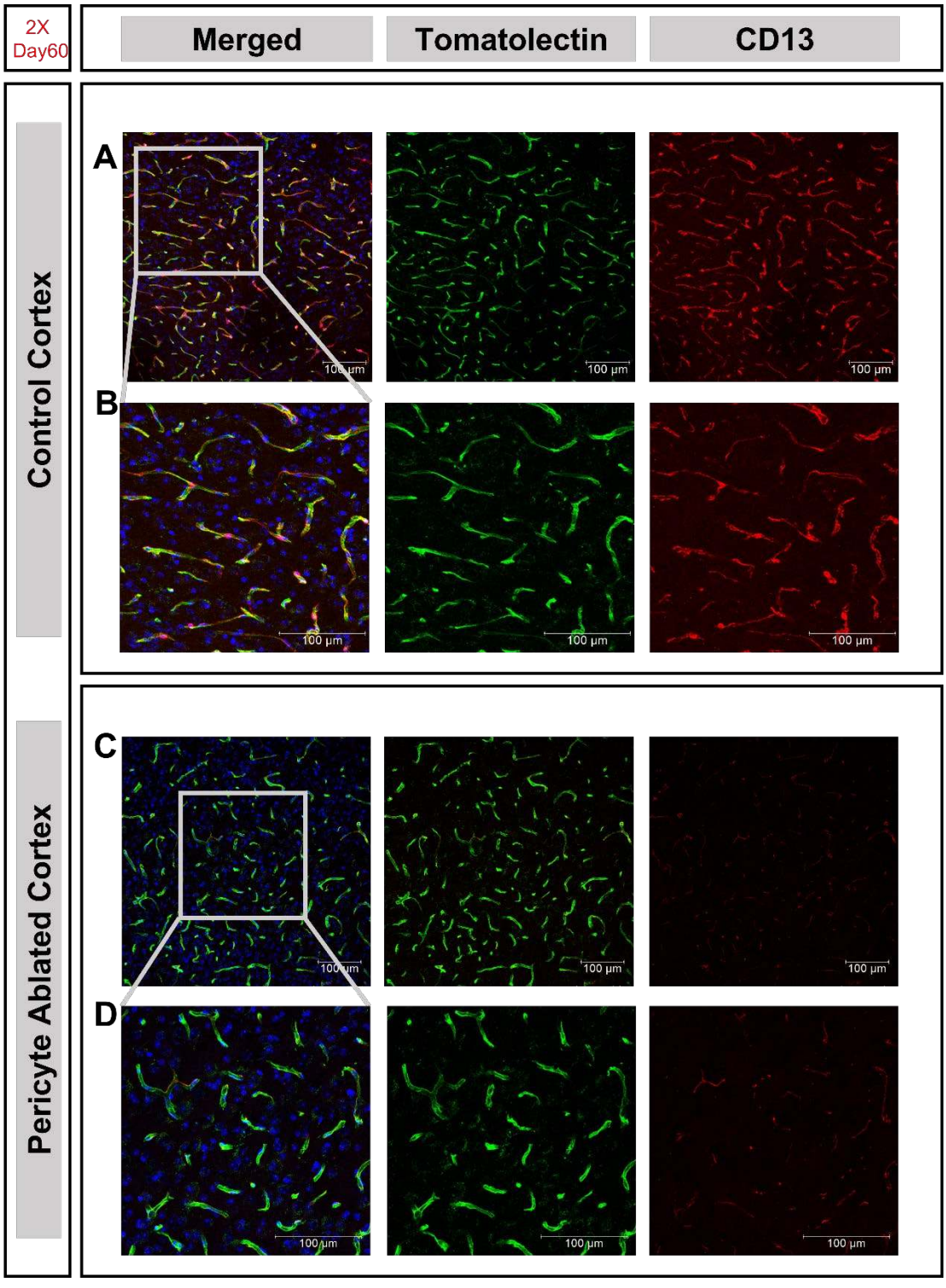

Figure 29. Cortex images of 2 times tamoxifen injected animals at Day 60

The confocal microscopy images of the CD13 stained pericytes (red) and Tomatolectin stained vessels and merged images with the Hoechst-stained nuclei (blue) are shown for the control group (A and B) and the pericyte ablated group (C and D). A and C were taken by using 20X objective, and B and C show the images taken by 2X digital zoom with the same objective. In C and D, the pericyte coverage and the

number are decreased compared to the pericyte coverage and the number of the A and B. The scale bars are shown in the right bottom corner of each image as 100µm.

The pericyte coverage reduction was also observable in the confocal images of the long-term pericyte ablated cortex (Figure 29).

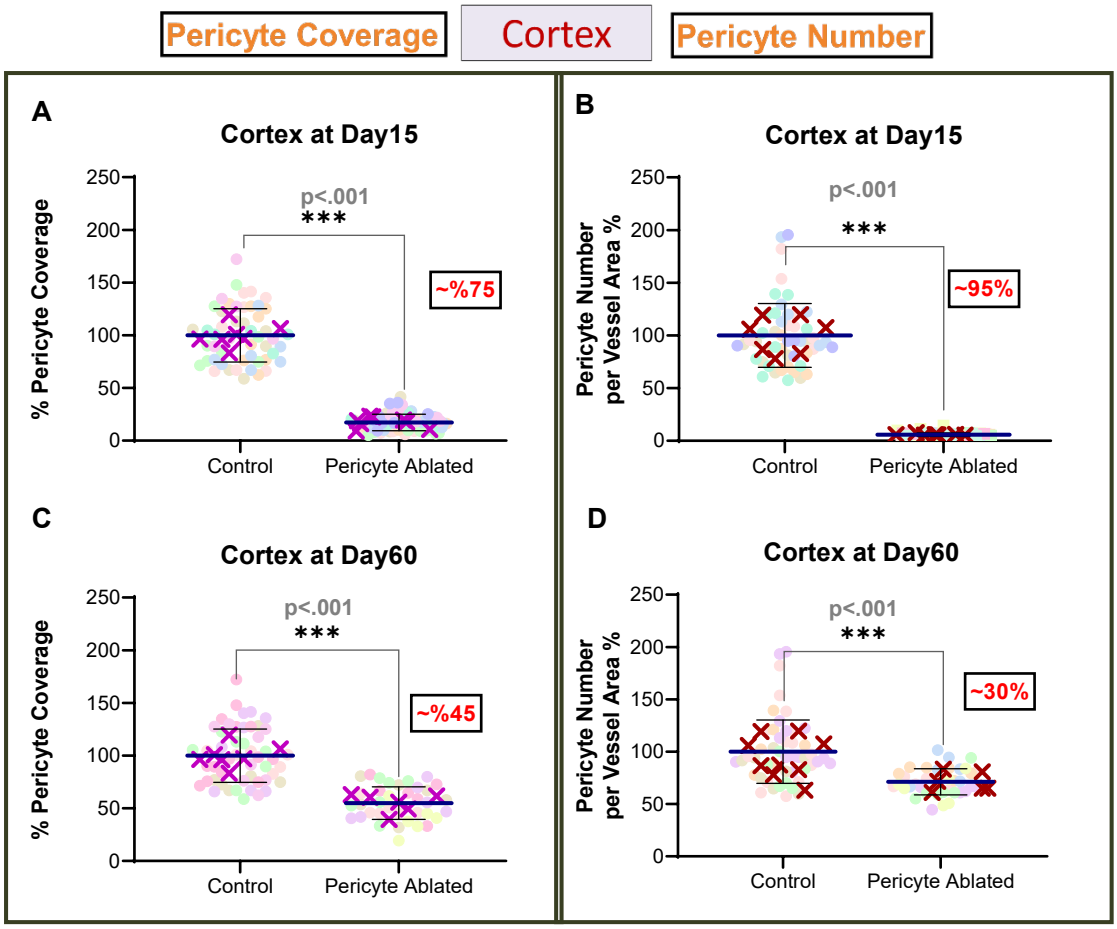

Figure 30. Quantification of the pericyte coverage and number in the cortex for two times tamoxifen injected animals

The confocal images of the cortex were quantified in terms of pericyte coverage (A and C) and pericyte number (C and D) at both Day 15 (A and B) and Day 60 (C and D) time points. A shows a 75% reduction in the pericyte coverage in the cortices of the two consecutive days of tamoxifen administered animals in 15 Days. For the same images, a 95% of reduction in the pericyte number is shown in B, for A and B, n=8 for the pericyte ablated group, and n=7 for the control group. In C and D, the pericyte coverage decrease of 45% and pericyte number decrease of 30% in the cortices of the pericyte ablated mice were

shown, respectively, for Day60. In C and D, n=6 for the pericyte ablated group and n=7 for the control group. The x symbols on the graphs show the average of each animal, and the different colors of dots show the pericyte coverage of the individual images of each animal (6-8 images per animal). The values were normalized to the control group average value as a percentage. The statistical analysis was done by Student's t-test (two-tailed Mann Whitney test). $p<0.001$ for all the graphs. The error bars show the SD.

The quantification of 8 images from 4 non-adjacent sections of cortex tissue for each animal showed a 75% decrease in pericyte coverage in the cortex at Day15 (Figure 30. A) and a 45% decrease at Day60 (Figure 30. C). Pericyte numbers were also decreased consistently with the pericyte coverage as 95% (Figure 30. B) and 30% (Figure 30. D) for Day15 and Day60, respectively.

3.3.2 Pericyte Ablation in the Spinal Cord

The pericyte coverage analysis of the cortex showed that two times tamoxifen injections were enough to achieve a sufficient pericyte ablation without harming the general health of the animals. Therefore, before the further experiments with our pericyte ablation model, the pericyte coverage of the spinal cord for the two times tamoxifen injected animals were also analyzed.

Pericyte Ablation induced by two repetitive doses of tamoxifen (2X)

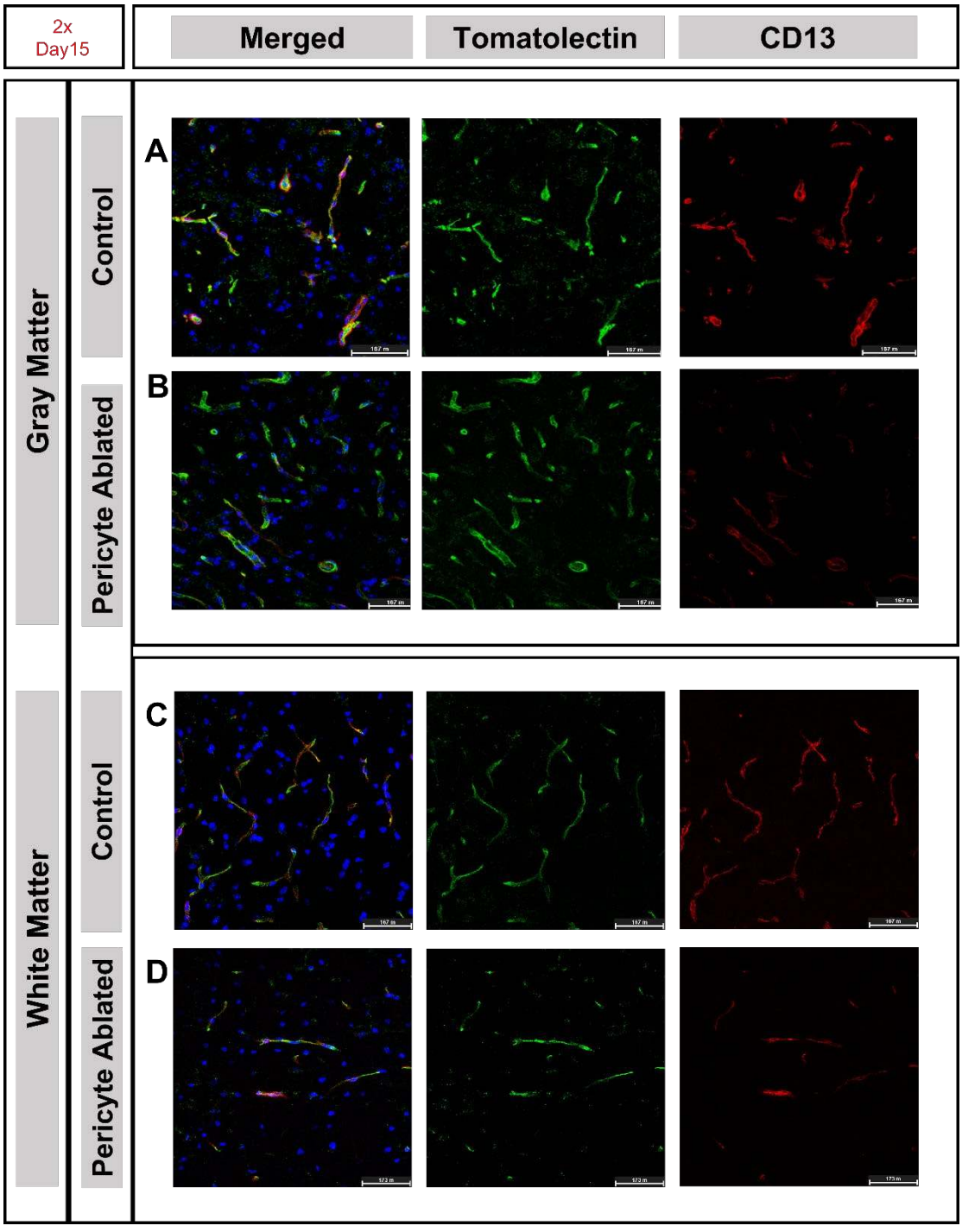

Figure 31. Spinal Cord images of 2 times tamoxifen injected animals at Day 15

The confocal microscopy images of the CD13 stained pericytes (red) and Tomatolectin stained vessels and merged images with the Hoechst-stained nuclei (blue) are shown for the control group (A and C), and the pericyte ablated group (B and D). A and B show the images of the gray matter, while C and D

show the images of the white matter. All images were taken by using a 40X objective. In B and D, the pericyte coverage and the number are decreased compared to the pericyte coverage and the number of the A and C. The scale bars are shown in the right bottom corner of each image as 100μm.

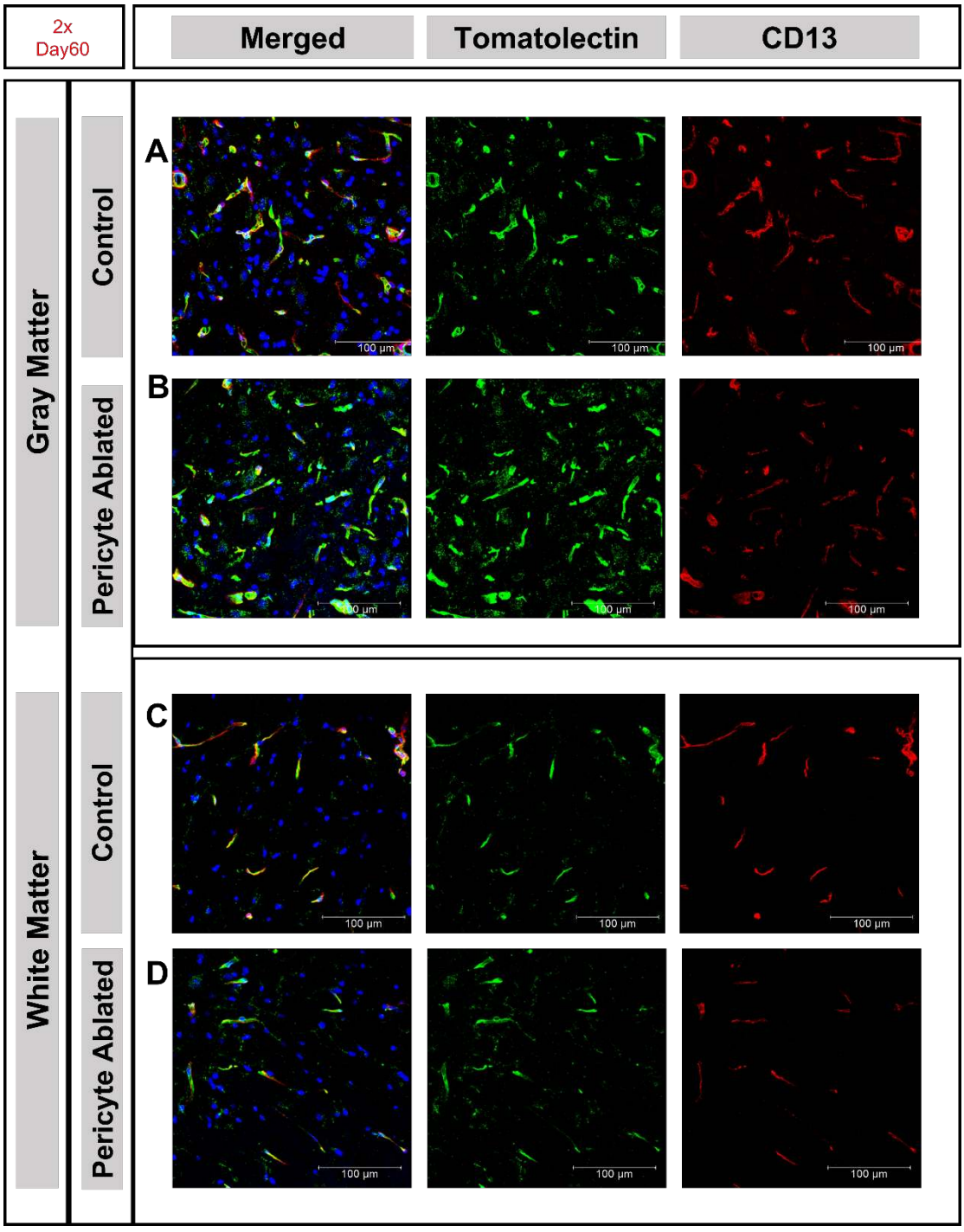

Figure 32. Spinal Cord images of 2 times tamoxifen injected animals at Day 60

The confocal microscopy images of the CD13 stained pericytes (red) and Tomatolectin stained vessels and merged images with the Hoechst-stained nuclei (blue) are shown for the control group (A and C), and the pericyte ablated group (B and D). A and B show the images of the gray matter, while C and D show the images of the white matter. All images were taken by using a 40X objective. In B and D, the

pericyte coverage and the number are decreased compared to the pericyte coverage and the number of the A and C. The scale bars are shown in the right bottom corner of each image as 100μm.

The confocal images of the spinal cords of both short-term (Figure 31) and long-term (Figure 32) pericyte ablation models showed a prominent pericyte coverage decrease in both white matter and gray matter.

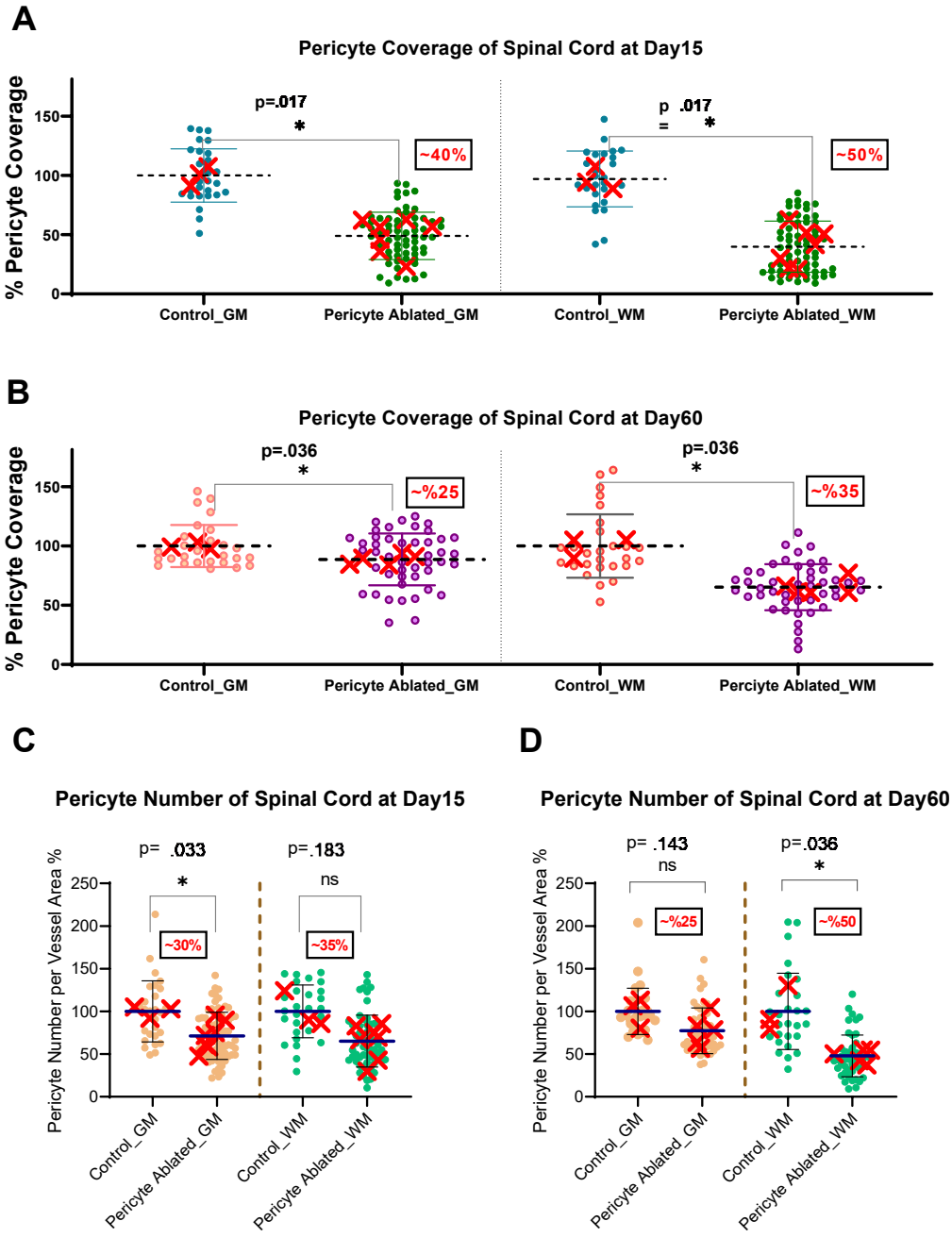

Figure 33. Quantification of the pericyte coverage and number in the Spinal Cord for two times tamoxifen injected animals

The confocal images of the gray and white matter of the spinal cord were quantified in terms of pericyte coverage (A and B) and pericyte number (C and D) at both Day 15 (A and C) and Day 60 (B and D) time points. A shows a 40% reduction in the pericyte coverage in the gray matter and a 30 % reduction in the white matter of the two consecutive days of tamoxifen administered animals in 15 Days. For the same

images, 39% of reduction in the pericyte number in the gray matter and 35% reduction in the white matter is shown in C. For A and C, n=7 for the pericyte ablated group and n=3 for the control group. In B and D, the pericyte coverage decreased by 25% in the gray matter and 35% in the white matter, and the pericyte number decreased by 25% in the gray matter, and 50% in the white matter of the pericyte ablated mice were shown, respectively for Day60. In B and D, n=5 for the pericyte ablated group and n=7 for the control group. The x symbols on the graphs show the average of each animal, and the different colors of dots show the pericyte coverage of the individual images of each animal (12 images per animal, four images from each spinal cord segment). The values were normalized to the average of the control group. The statistical analysis was done by Student's t-test (two-tailed Mann Whitney test). The error bars show the SDs.

A total of 24 images from gray matter and white matter of each spinal cord segment per animal were analyzed separately. In the short term, pericyte coverage was decreased by 40 % in the gray matter and 50% in the white matter (Figure 33. A). In the long-term analysis, these percentages were decreased to 25% and 35%, respectively (Figure 33. B). Pericyte number analysis revealed that 30% of pericytes in the gray matter and 35% of pericytes in the white matter were ablated in the short term (Figure 33. C). In the long term, 25 % of the pericytes in the gray matter and 50% of pericytes in the white matter were ablated (Figure 33).

3.4 The phenotypical changes of pericyte ablated mice after five consecutive days of tamoxifen administration

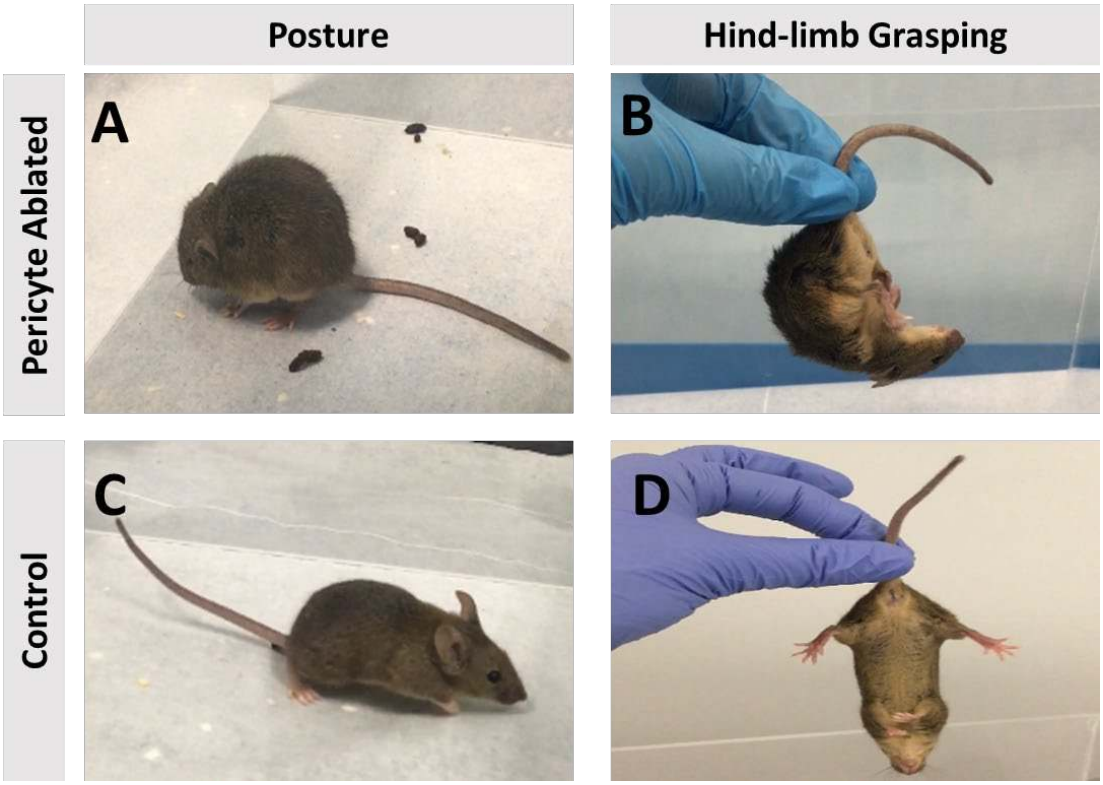

Figure 34.The phenotypical changes after the pericyte ablation by the full dose (5X) of tamoxifen administration

A and B show the pericyte ablated mice, while C and D show the control group (wild-type like) mice with five consecutive tamoxifen doses after the first week of the administration. A shows the posture change and the appearance of the humpback in the pericyte ablated mice, and in B, the foot grasping reflex of the pericyte ablated mice is shown.

In the pericyte ablated mice with five consecutive days of the tamoxifen injections, some physical changes were observed, such as the abnormal holding of the hindlimbs and humpback (see Figure 34). Additional to these physical changes, forced and imbalanced walking is also observed. These phenotypes were less detectable as the number of tamoxifen injection repeats decreased.

3.5 mRNA level changes of Pdgfrβ and CD31 genes in the pericyte ablated mice

The pericyte coverage changes in the 2X TAM pericyte ablation group were confirmed in the gene expression level by real-time quantitative polymerase chain reaction (RT-qPCR).

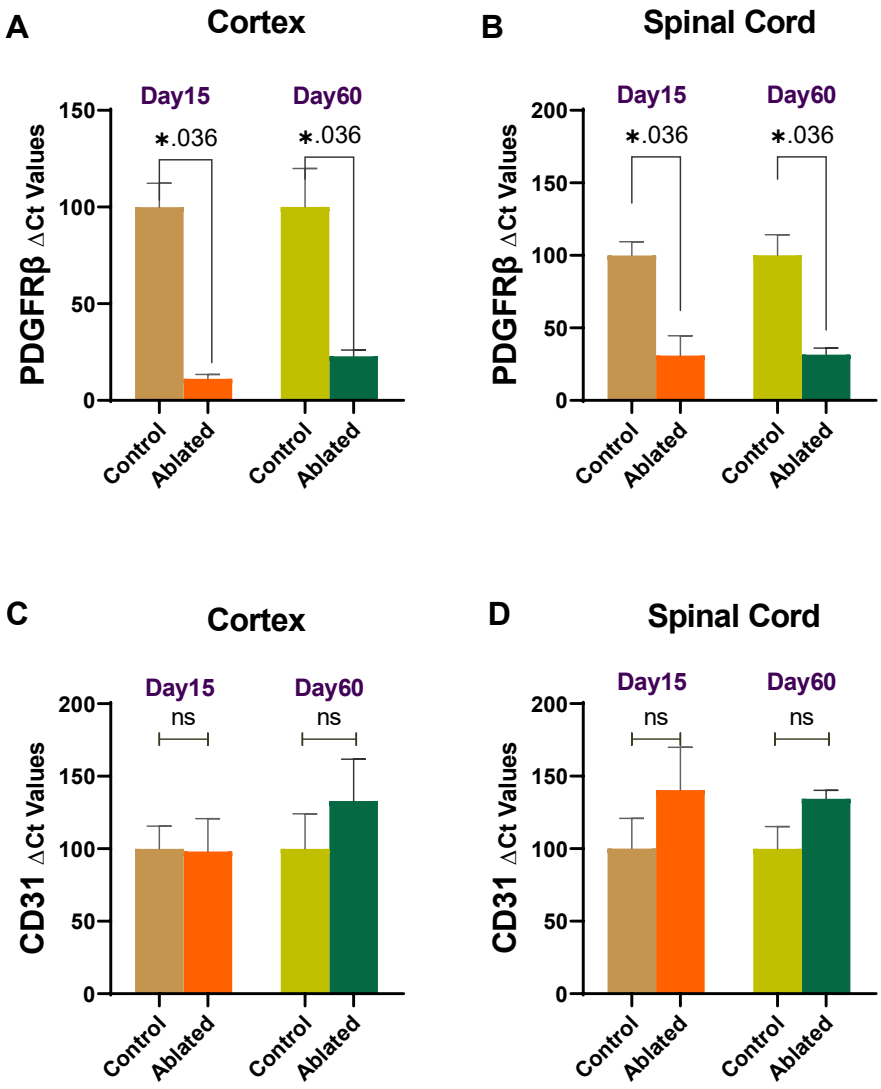

Figure 35. mRNA level changes of Pdgfrβ and CD31 genes in the pericyte ablated mice

A and B show the mRNA levels of the *Pdgfrβ*, as a pericyte marker, at Day 15 and Day 60 for brain and spinal cord tissues of control and pericyte ablated mice with the injection of 2 repetitive doses of

tamoxifen, respectively. In A and B, n=6 for the control group and n=2 for the ablation group. p=0.036 for the cortex and the spinal cord mRNA level changes in both termination points. C and D show the mRNA levels of the CD31, as an endothelial marker, at Day 15 and Day 60 for brain and spinal cord tissues of control and pericyte ablated mice with the injection of 2 repetitive doses of tamoxifen, respectively. C and D show mRNA levels of CD31 at Day15 and Day60 for brain and spinal cord, of control and pericyte ablated mice with the injection of 2 repetitive doses of tamoxifen, respectively. Compared to the control mice, the CD31 mRNA levels did not change significantly in both cortex and spinal cord for the pericyte ablated mice. In C, n=6 for the Day 15 control group and n=5 for the ablated group and n=6 for Day60 control group, and n=2 for the pericyte ablated group. In D, n=6 for the Day 15 control group and n=4 for the ablated group and n=4 for Day60 control group, and n=2 for the pericyte ablated group. Statistical analysis was done by Student's t-test (two-tailed Mann-Whitney test). The error bars show the SEMs.

Compared to control mice, *Pdgfrβ* gene expression decreased ~90% in the cortex (Figure 35. A, B) and ~60% in the spinal cord in the pericyte ablated mice at both Day 15 and Day 60. Expressions of CD31 (Figure 35. C, D) were similar between the groups.

3.6 Analysis of Vessel Morphology after Pericyte Ablation

The initial aim of creating our inducible pericyte ablation model was to eliminate the vascular abnormalities exiting in the other inborn deficiency models. Therefore, we next checked the vascular parameters in our inducible pericyte ablated mice.

3.6.1 Pericyte Ablation induced by two repetitive doses of tamoxifen (2X)

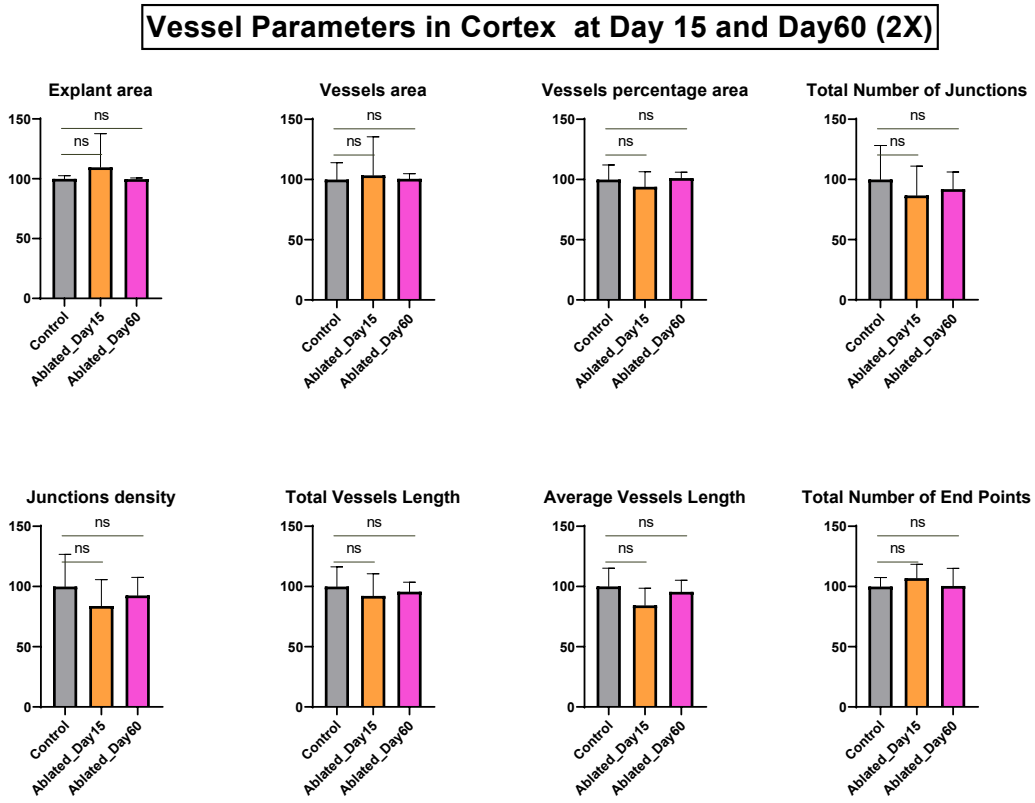

Figure 36. Vessel Parameters of the pericyte ablated and control mice brains within 15 days and 60 days after the tamoxifen injection for two consecutive days

Explant area, Vessel area, Vessel Percentage Area, Total Number of Junctions, Junction Density, Total Vessel Length, Average Vessel Length, and Total Number of End Points were analyzed by using tomatolectin stained vessel images. There was no significant difference between the cortical vessels of the pericyte ablated group and the control group at the time of 15 days post-injection of two doses of tamoxifen in terms of analyzed vessel parameters. n=8 for the control group and n=8 for the pericyte

ablated group at day 15, and n=6 for the pericyte ablated group at day 60. 4-6 cortex images were quantified per animal. Statistical analysis was done by Student's t-test (two-tailed Mann-Whitney test). The error bars show the SDs.

We have not observed any significant changes in the vessel parameters in the brains of the two doses of tamoxifen administered group in both time points (Figure 36).

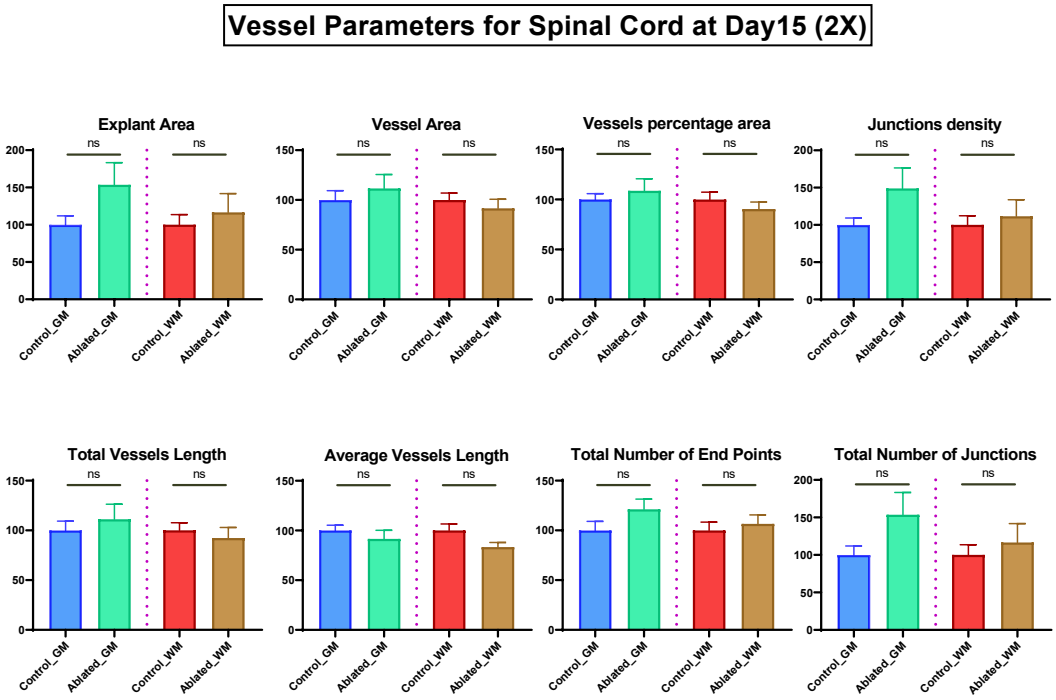

Figure 37. Vessel Parameters of the pericyte ablated and control mice spinal cords within 15 days after the tamoxifen injection for two consecutive days

Explant area, Vessel area, Vessel Percentage Area, Total Number of Junctions, Junction Density, Total Vessel Length, Average Vessel Length, and Total Number of End Points were analyzed by using tomatolectin stained vessel images. There was no significant difference between the spinal cord vessels of the pericyte ablated group and the control group at the time of 15 days post-injection of 2 doses of tamoxifen in terms of analyzed vessel parameters. n=3 for the control group and n=7 for the pericyte ablated group. Twelve images per animal as four images from each spinal cord segment (cervical,

thoracic, and lumbar) white matter and gray matter were separately quantified. Statistical analysis was done by Student's t-test (two-tailed Mann-Whitney test). The error bars show the SDs.

When we checked the vessel parameters for the spinal cords of the 2X TAM group in the short term, we again did not observe any significant changes (Figure 37).

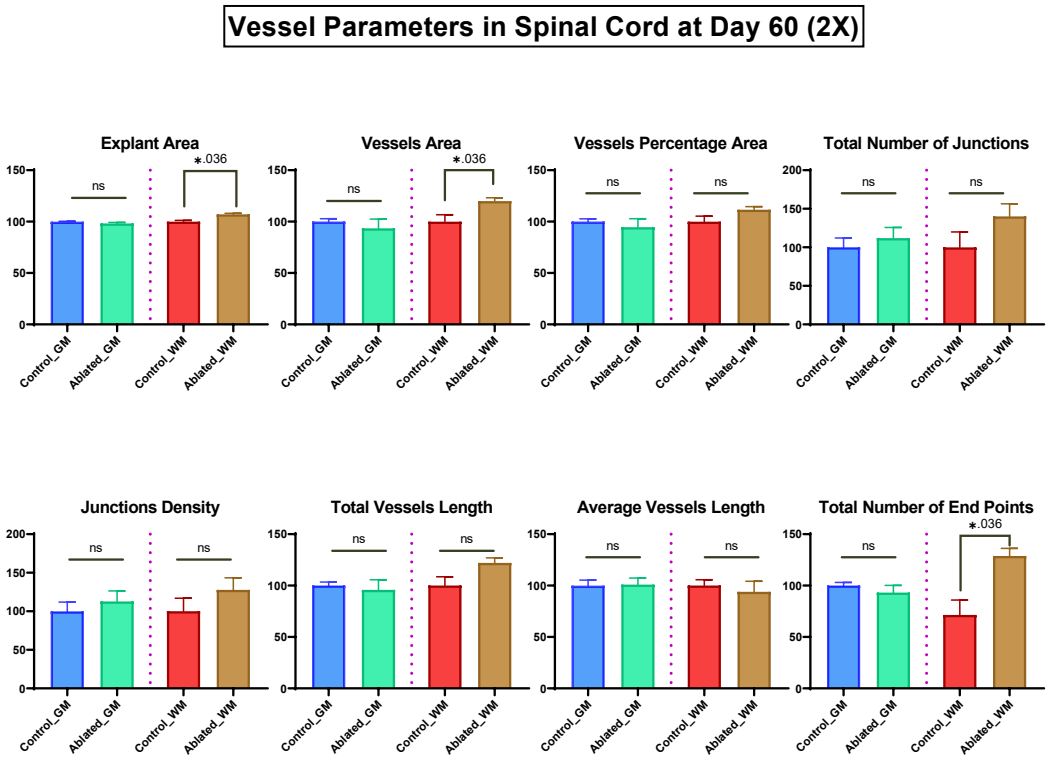

Figure 38. Vessel Parameters of the pericyte ablated and control mice spinal cords within 60 days after the tamoxifen injection for two consecutive days

Explant area, Vessel area, Vessel Percentage Area, Total Number of Junctions, Junction Density, Total Vessel Length, Average Vessel Length, and Total Number of End Points were analyzed by using tomatolectin stained vessel images. There was a significant increase in the explant area, vessel area, and the total number of endpoints in the white matter of the pericyte ablated and the control mice at the time of 60 days post-injection tamoxifen for two consecutive days—n =3 for the control group and n=5 for the pericyte ablated group. Twelve images per animal as four images from each spinal cord segment (cervical, thoracic, and lumbar) white matter and gray matter were separately quantified. Statistical analysis was done by Student's t-test (two-tailed Mann-Whitney test). The error bars show the SDs.

However, in the long-term 2X pericyte ablation model spinal cord, we observed some significant changes in the white matter. The explant area, vessel area, and the total number of endpoints increased significantly (Figure 38).

3.6.2 Pericyte Ablation induced by three repetitive doses of tamoxifen (3X)

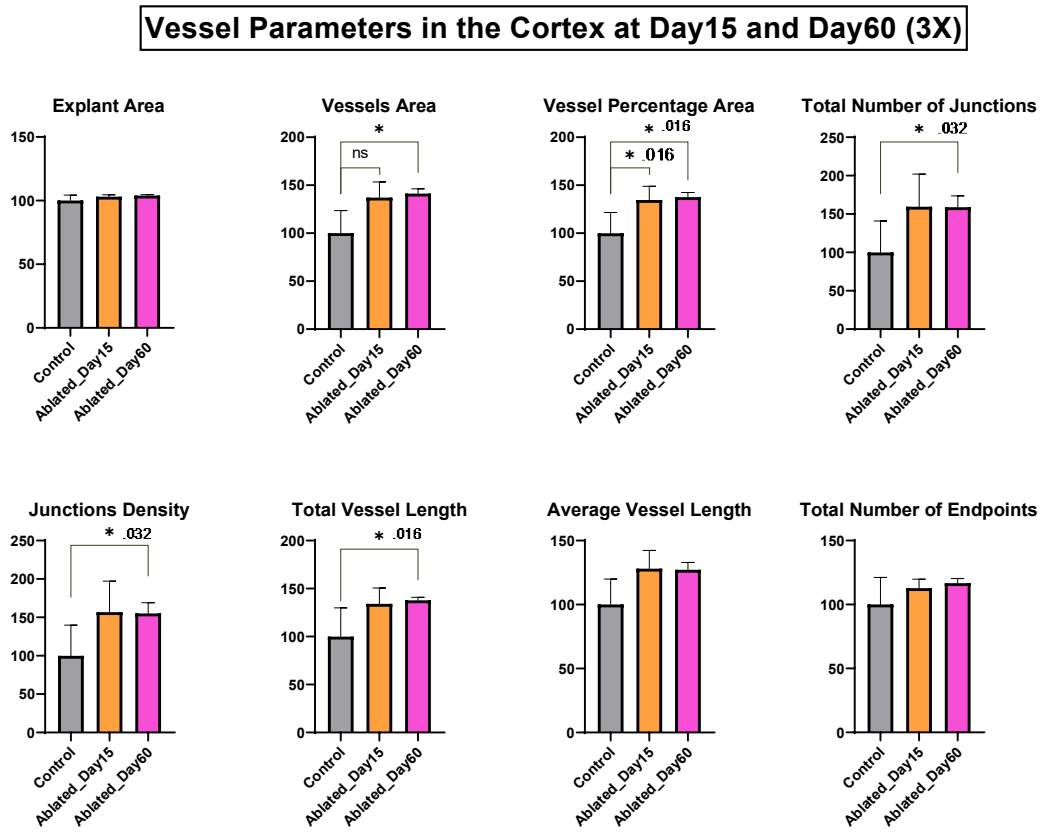

Figure 39. Vessel Parameters of the pericyte ablated and control mice brains within 15 days and 60 days after the tamoxifen injection for three consecutive days

Explant area, Vessel area, Vessel Percentage Area, Total Number of Junctions, Junction Density, Total Vessel Length, Average Vessel Length, and Total Number of End Points were analyzed by using tomatolectin stained vessel images. There was a significant increase in the vessel area, vessel percentage area both at the time of 15 days and 60 days post-injection of the two repetitive doses of tamoxifen injection. A significant difference also emerged for the junction's density and total vessel length at 60 days post-injection of tamoxifen, although not significantly differed at Day15. n=5 for the control group and n=4 for the pericyte ablated groups at both Days 15 and Day60. 4-6 cortex images were quantified

per animal. Statistical analysis was done by Student's t-test (two-tailed Mann-Whitney test). The error bars show the SDs.

In the cortical vessels of the 3X TAM group (3 consecutive days of tamoxifen injections), some changes in the vessel parameters were observed. In the short term, only the vessel percentage area has increased significantly. However, in the long term, in addition to the increase of the vessel percentage area, vessel area, total number of junctions, junctions' density, total vessel length also significantly increased in the 3X TAM group (Figure 39).

3.6.3 Pericyte Ablation induced by five repetitive doses of tamoxifen (5X)

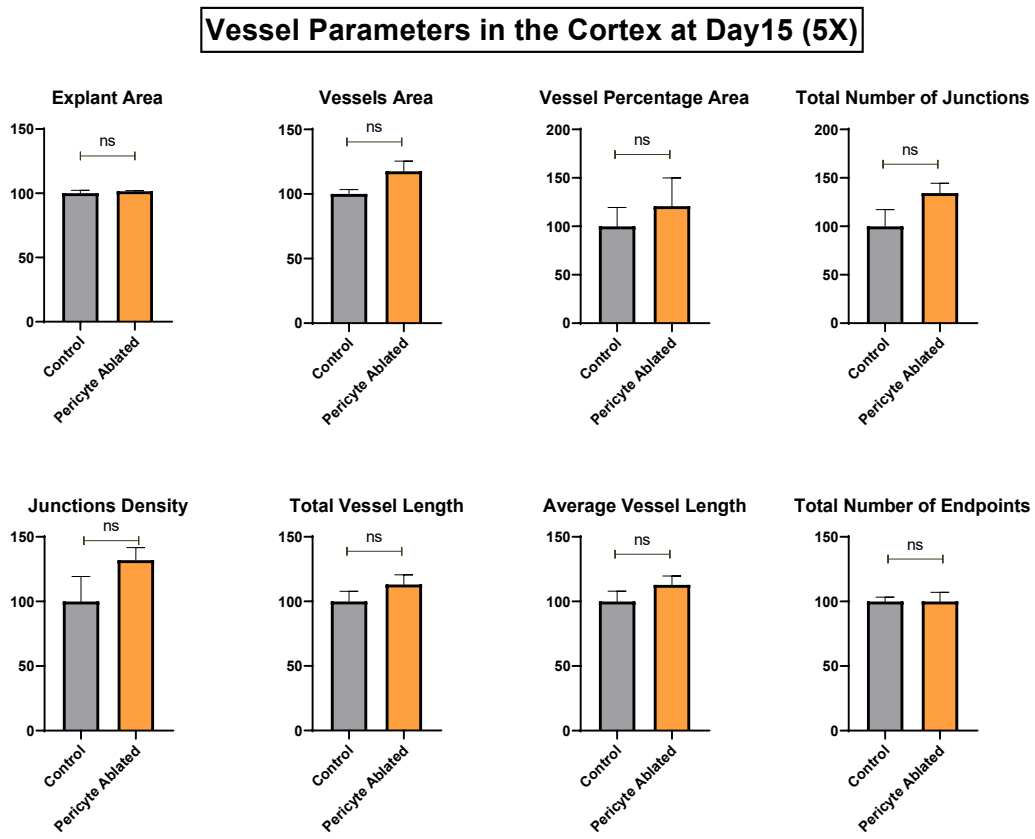

Figure 40. Vessel Parameters of the pericyte ablated and control mice brains within 15 days after the tamoxifen injection for five consecutive days

Explant area, Vessel area, Vessel Percentage Area, Total Number of Junctions, Junction Density, Total Vessel Length, Average Vessel Length, and Total Number of End Points were analyzed by using

tomatolectin stained vessel images. Although there is an increasing pattern in the pericyte ablated mice in terms of vessel area, vessel percentage area, the total number of junctions, total length, and total vessel length of the vessels, and the junction's density, these differences were not significant at the time of 15 days post-injection of 5 repetitive doses of tamoxifen. n=2 for the control group and n=3 for the pericyte ablated group. 4-6 cortex images were quantified per animal. Statistical analysis was done by Student's t-test (two-tailed Mann-Whitney test). The error bars show the SDs.

Lastly, the effects of pericyte ablation induced by the full dosage of tamoxifen administration (5 repeats of tamoxifen injections) were also analyzed in the short term. No significant differences were found. However, there was an increasing pattern in the parameters of vessel area, vessel percentage area, the total number of junctions, junction density, total vessel length, and average vessel length parameters (Figure 40).

3.7 Behavioral analysis of Pericyte Ablation

To check the cognitive function and locomotor activities of the pericyte ablated mice, we performed Y maze and Kondziela's inverted screen test, respectively.

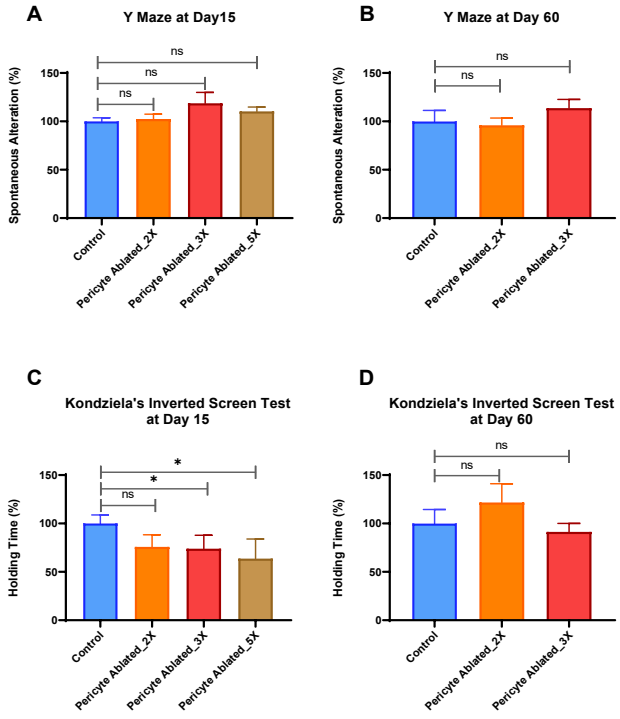

Figure 41. Cognitive and Motor function changes due to dose-dependent pericyte ablation Y maze

Y maze performance was performed for the cognitive function assessment, and Kondziela's Inverted screen test was used for the quantification of the motor function changes on the pericyte ablated mice compared to the control mice. In the Y maze, there was no significant change in the spontaneous alternations between the groups in both short and long-term pericyte ablation cases (A and B). In A, n=5 for 5x, n=8 for 3x, n=11 for 2x and n=15 for the control group. In B, n=4 for 3x and n=7 for 2x, and n=8 for the control group. In the Kodziela's Inverted Screen test, at Day15, there were 35% (p=0.033), 25% (p=0.012), and 25% (p=0.120) decrease in the holding time of the pericyte ablated animals with 5x, 3x, and 2x tamoxifen injections, respectively (C). In C, n=7 for 5x, n=11 for 3x, n=11 for 2x and n=19 for the control group. In D, n=10 for 3x and n=11 for 2x and n=12 for the control group. The statistical analysis was done by Student's t-test (one-tailed Mann Whitney test). The error bars show the SDs.

The behavioral experiments showed that pericyte ablation did not cause any cognitive changes in terms of spatial recognition memory for all of the dosages (Figure 41 A, B). For the locomotor activity test, we observed a gradual decrease with the increment of the tamoxifen dosage in the short term. The reduction of motor activity performance was significant for 3X TAM and 5X TAM groups, but it was not statistically significant for the 2X TAM group. However, in the long term, even though there is still a slight reduction in the motor performance of the 3X TAM group, this difference was not significant (Figure 41 A, B).

3.8 Establishment of active EAE model

To establish the EAE model in our laboratory, we have designed a pilot study with wild-type C57BL6/J mice. We have used the Hooke Laboratory MOG EAE kit for the induction of EAE.

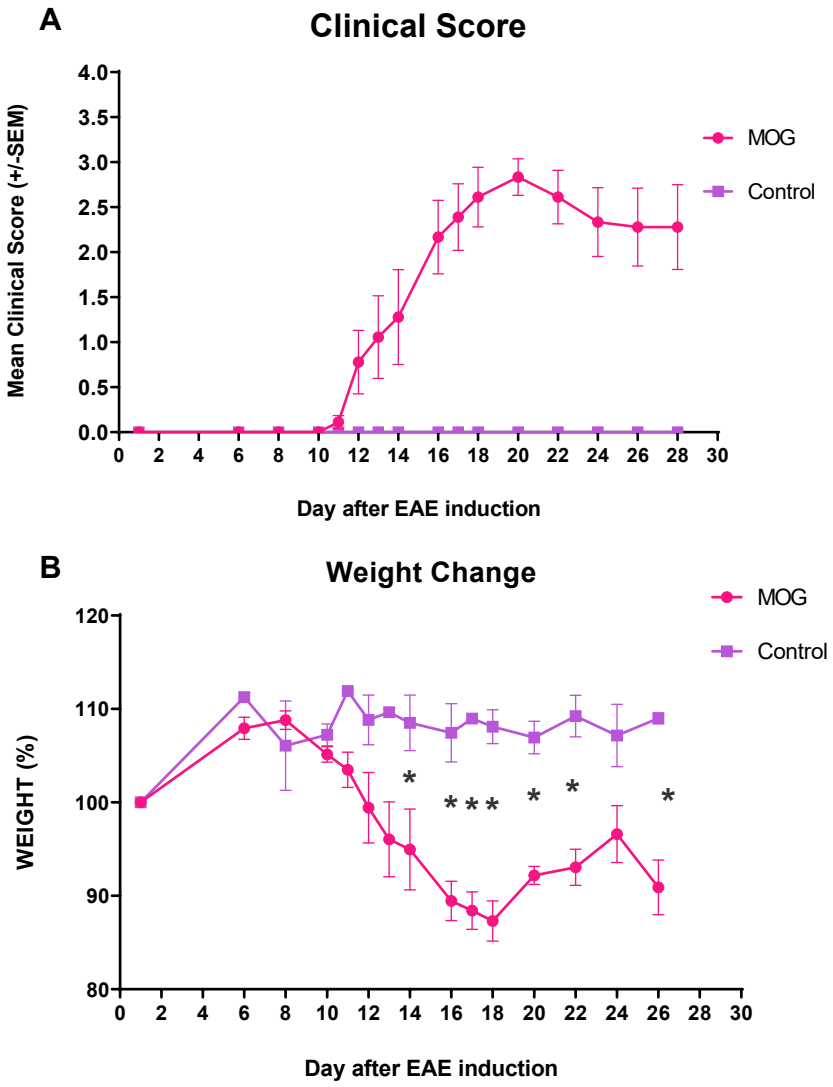

Figure 42. Clinical Score and Weight Changes of Active MOG EAE model of wild type C57BL6/J mice

MOG EAE model was characterized in terms of clinical symptomology and weight loss. In Figure A, the average clinical scores of the animals were graphed for 28 days. The experimental group started to show symptoms around Day 10 and reached the average peak score of 3.0 around Day 20. Then a partial

recovery was observed between Day20 to Day 28. In B, the normalized weights of the animals were graphed during the experiment. The difference between the MOG EAE experimental group and the control group was significant after the 14th day, and this significance continued until the end of the experiment. The statistical analysis was done by 2-way ANOVA repeated measures multiple comparison test. n=9 for the MOG EAE group and n=3 for the control group. p=0.0296 for Day14, p=0.0087 For Day16, p<0.0001 for Day 18, p= 0.0051 for Day20, p=0.0027 for Day22, p= 0.1023 for Day 24, p= 0.0002 for Day 26. The error bars show the SEMs.

The first clinical symptom of EAE started around the 10th day. Then, scores kept increasing until the peak point around Day 18-22. The peak clinical score average was around score 3. Then a partial recovery followed with a reduction of the average score to around 2.5 (Figure 42. A). Correspondingly, EAE animals progressively lost weight while their clinical scores were increasing (Figure 42. B).

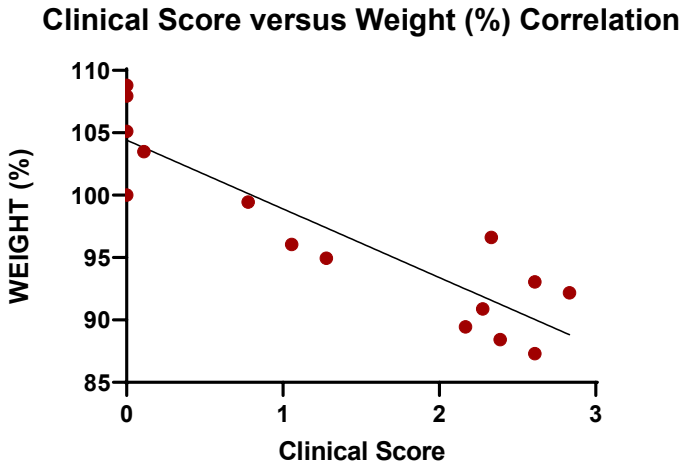

Figure 43 Negative Correlation between the Clinical Score and Weight Loss of the MOG EAE mice

Correlation and Linear Regression analyses were done between the average weight percent and the clinical scores of the MOG EAE animals in the corresponding days. Fifteen repeated measures of 9 animals were assessed for nine animals. Spearman r= -0.8513 and p<0.0001.

The correlation analysis of the weight loss and the clinical progression of the EAE model showed a significant correlation between these two parameters (Figure 43).

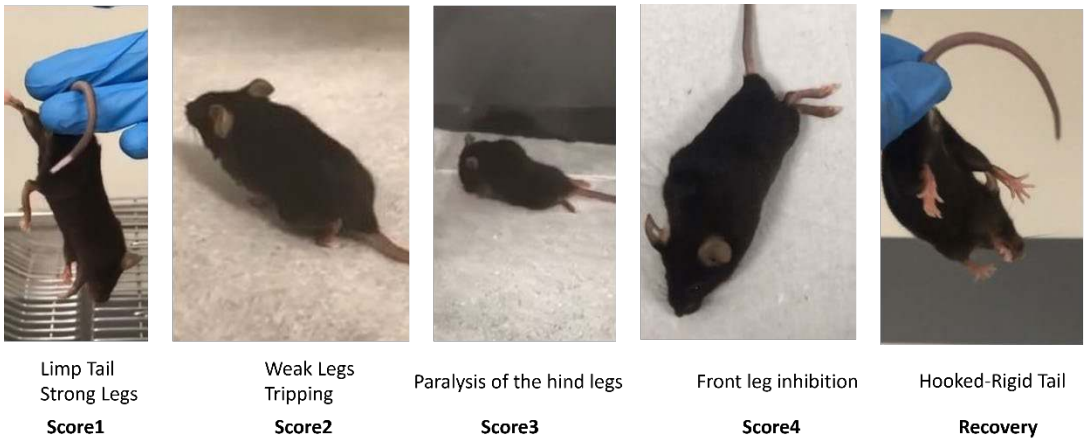

Figure 44. Visual representation of clinical scores of the Active EAE mice

The clinical progression of the EAE model in C57BL/6 mice was shown from Score1 to Recovery. In score 1, the tail gets limp and drops over the finger. On score 2, the hind legs of the mouse start weakening, and so the mouse starts tripping. In score 3, both hind legs get paralyzed, and a humpback is observed. Further in score4, front leg inhibition is also added on top of all these symptoms. Then the most of these symptoms partially recover with an appearance of hooked and rigid tail phenotype.

As a quick review of EAE mice clinical scoring, the most prominent futures of each score were demonstrated in Figure 44. As the first symptom of immune cell infiltration into the parenchyma, the tail gets limp and drops over the finger. Then in score 2, the legs start to get weaker, and the mouse begins limping. While the disease is progressing in score 3, both legs are paralyzed. On score four also the front leg weakness is added on top of all the other symptoms. In the final stage of the model, a partial recovery starts with the amelioration of most of the signs, and a hooked-rigid tail is observed.

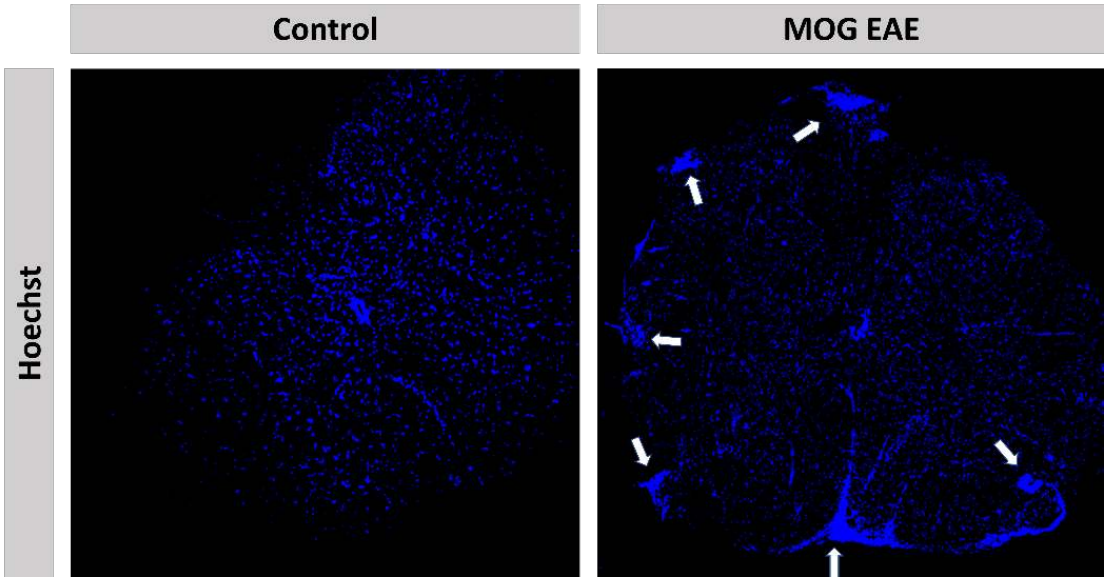

Figure 45. Immune cell infiltrations into the white matter of the spinal cord in the MOG EAE mouse model

The Hoechst staining of the nuclei in control and MOG EAE mice's spinal cord tissues were shown. The white arrows showed the cellular accumulations of the infiltrating immune cells.

The successful EAE modeling was also confirmed by the Hoechst staining of the spinal cord. The immune cell infiltrations to the CNS parenchyma of the MOG EAE mice are nicely shown in Figure 45.

3.9 The effect of inducible pericyte ablation on the pathogenesis and the progression of EAE

After the characterization of the pericyte ablation model and the establishment of the EAE model in wild-type mice next, we combined these two models to see the effect of pericyte loss on neuroinflammation.

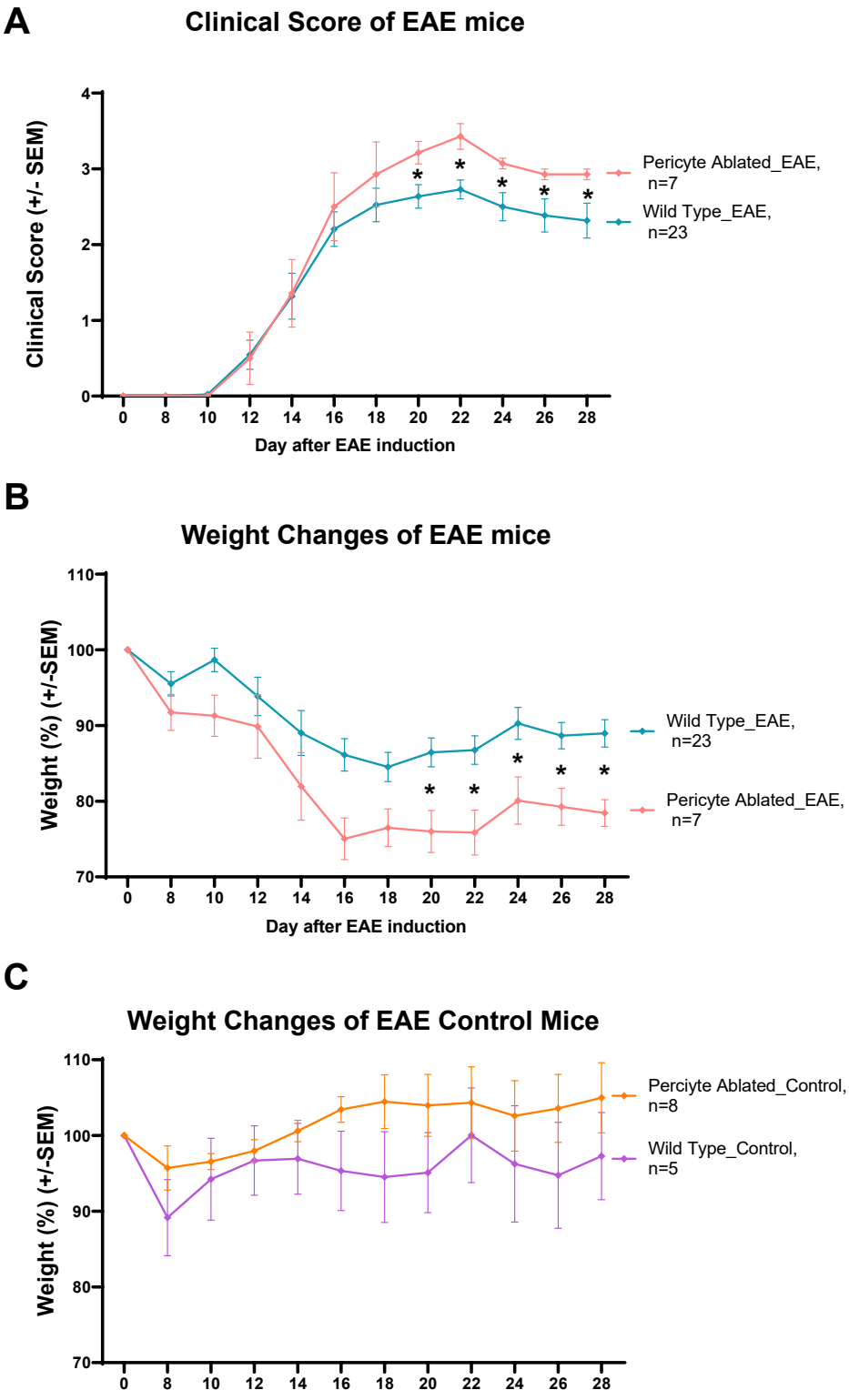

Figure 46. Clinical Scores and Weight Changes of the Pericyte Ablated and Control EAE mice

The clinical scores of pericyte ablated and wild-type mice were compared in A. The progression of the disease was significantly more severe after Day20, which is the peak of the disease, and the recovery

was relevantly less compared to the wild-type EAE mice. The weight changes of pericyte ablated mice and the wild type mice during EAE were also compared in B. Pericyte ablated mice lost more weight than the wild type mice, and this difference was significant starting from Day 20 to the end of the experiment. The weight changes of the EAE control mice were also compared for the pericyte ablated mice and the wild-type mice, and no significant differences were found. All the significance analyses were done by 2-way ANOVA repeated measures multiple comparison test. In A, p= 0.0141 for Day20, p= 0.0056 at Day22, p= 0.0081 at Day24, p= 0.0276 at Day26 and p= 0.0188 at Day28. In B, p= 0.0411 ay Day8, p= 0.0067 at Day16, p= 0.0236 at Day18, p= 0.0093 at Day 20, p= 0.01 at Day22, 0.0194 at Day 24, p =0.0081 at Day28, p= 0.0005 at Day 28. There is no significant difference found in C, comparing the weight differences of pericyte ablated and wild-type control (EAE vehicle) mice. The error bars show the SEMs.

By comparing the clinical score and weight graphs of the wild-type EAE and pericyte EAE mice, we deduced the effect of the pericyte loss on neuroinflammation. In the clinical score observations, although the first clinical symptoms similarly developed and worsened up to score 1.5 for both groups, the exacerbation rate was higher in the pericyte ablated mice. Consequently, the clinical score of pericyte ablated mice reached a higher peak than the wild-type EAE mice. At the recovery stage, despite the recovery trend in both groups being similar, the pericyte ablated EAE mice did not recover as much as the wild-type EAE mice (Figure 46 A).

Corresponding to the clinical score data, we observed that both pericyte ablated mice and the wild-type mice with EAE lose weight compared to the vehicle-injected control. However, pericyte ablated mice lost significantly more weight than wild-type EAE mice (Figure 46 B). This difference was not because of only pericyte ablation because, when we look at the weight graphs of the pericyte ablated and wild-type EAE control mice with only vehicle injections, no difference was observed because of the pericyte ablation (Figure 46C). Therefore, the weight difference is caused by the EAE progression differences of pericyte ablated and wild-type EAE mice.

Figure 47. The physical appearance of the control and pericyte ablated EAE mice in the recovery phase

Both pericyte ablated and the wild-type EAE mice in the recovery stage have the hooked and rigid tail phenotype. However, the degree of muscle loss depending on EAE paralysis and disability is more in the pericyte ablated mice, where they are not able to use their hind legs to move. Furthermore, they cannot groom themselves properly, so the furs seem sticky.

In the recovery stage, the wild-type EAE mice gained control of their feet and arms with a rigidity that obstructed normal walking. However, pericyte ablated mice underwent more muscle loss, and even though they were able to move their limps, they could not stand on them or adequately use them (Figure 47).

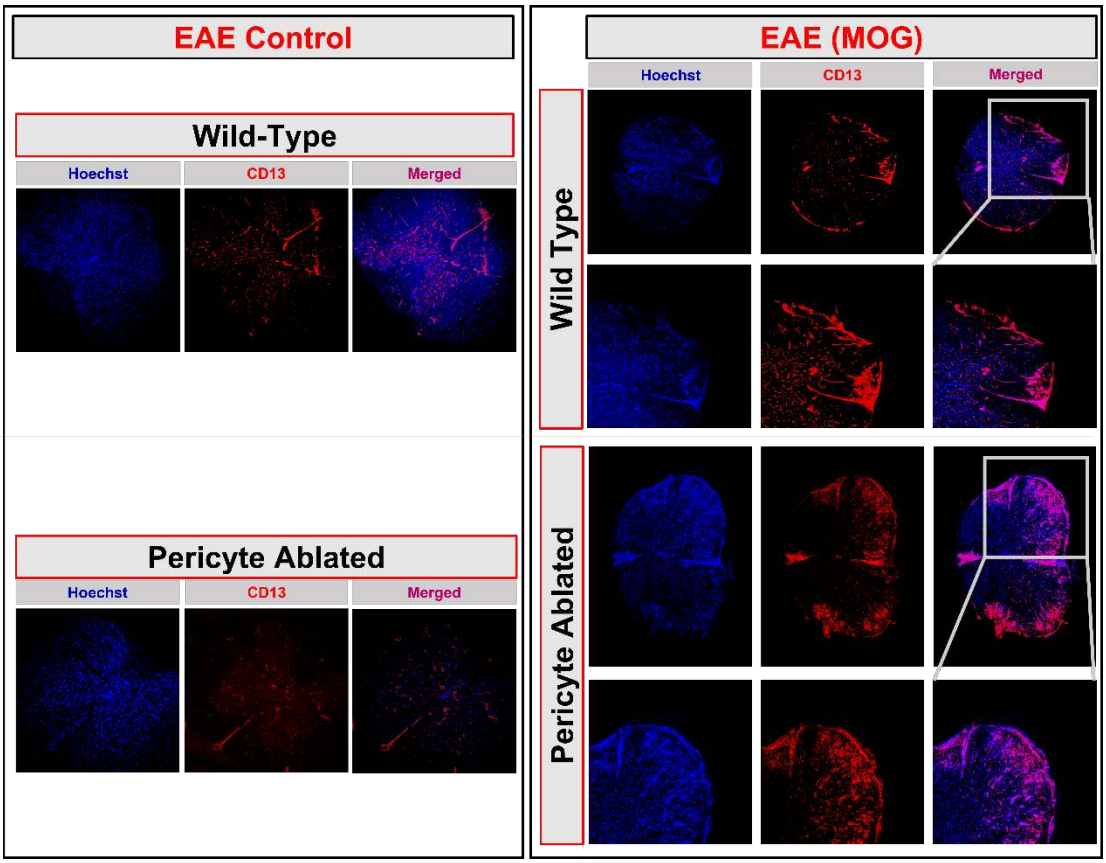

Figure 48. EAE Lesion Density in the Wild Type and Pericyte Ablated Mice

Immunohistochemical analysis of the spinal cord of the MOG EAE mice with or without pericyte ablation was done by CD13 staining for pericytes and Hoechst stating for the cell bodies. In the case of immune cell infiltration into the parenchyma, the accumulation of both strains was observed in the area of the inflammation lesion. In the spinal cords of both pericyte ablated and wild-type mice, there wasn't any cell accumulation that could be detected by the Hoechst nor CD13 staining (left panel). As expected, in both wild-type and pericyte ablated mice, there are EAE related cell infiltrations that were detected by both Hoechst and CD13 staining. As seen in the right bottom panel, the lesion amount and the size were more significant than the wild-type mice in the spinal cord of the pericyte ablated mice. The images were taken by the 20X objective with the tile scan function of the LASX software and merged.

Immunohistochemical analysis of the spinal cord tissues by the pericyte marker CD13 and cell body stain Hoechst we o revealed that pericyte ablated mice had more and larger lesions of immune cell accumulations than the lesions of wild-type EAE mice (Figure 48).

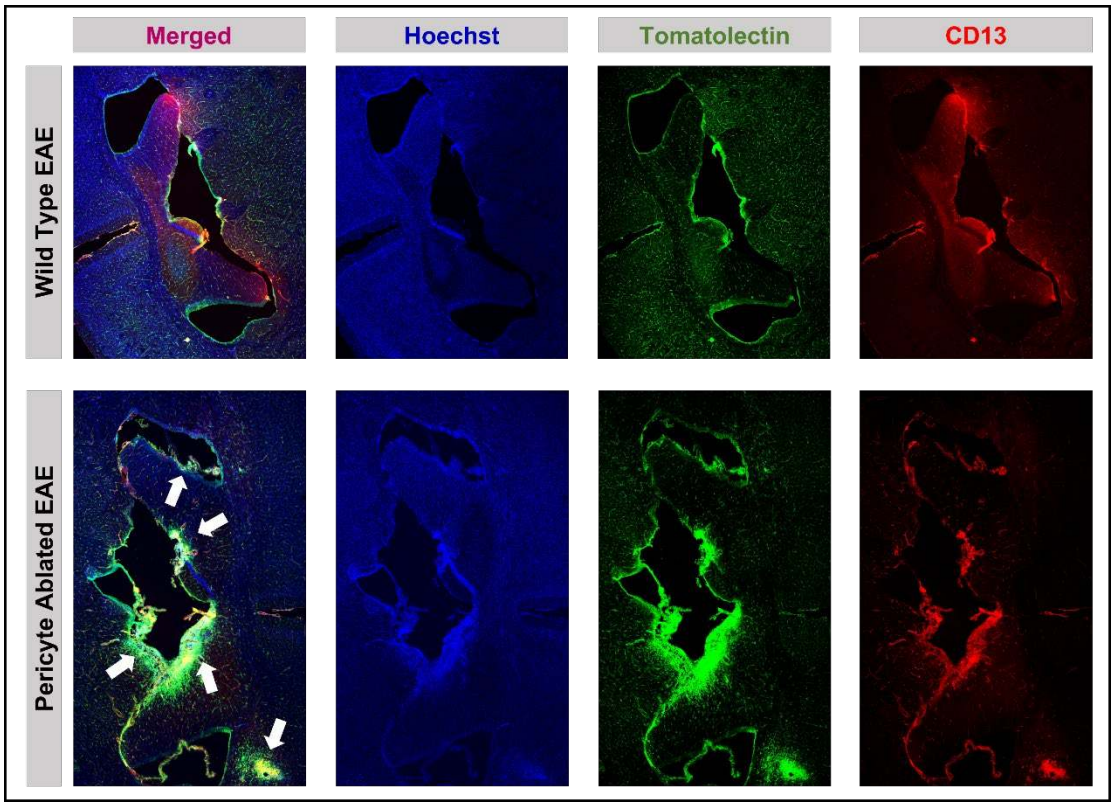

Figure 49. The pericyte ablation specific EAE lesion in the brain around the ventricles

Pericyte ablated and wild-type mice brains with EAE were stained with CD13 antibody for pericytes, Tomatolectin for endothelial cells, and Hoechst for the nucleus. Unusual cell infiltrations into the brain were from the ventricles were observed only in the pericyte ablated brains, and these cell types were stained with both the CD13 and Tomatolectin antibodies, as seen in the bottom panel. The white arrows in the bottom panel show the lesion foci in the pericyte ablated EAE model mice brain.

Lastly, as it is known, the MOG EAE model does not develop any lesions in the brain. However, interestingly, some unexpected immune cell infiltrations around the ventricles of the pericyte ablated mice were observed, and these infiltrations were not apparent in the wild-type EAE mice brains (Figure 49).

3.10 The results of the internal technical controls

A variety of internal controls were used to eliminate any possible side effects of the experimental procedures, such as Cre activation, tamoxifen administration, and usage of different races. Firstly, the pericyte ablation was again confirmed by immunochemical analysis of the pericyte ablated and wild-type mice with EAE.

3.10.1 Confirmation of the pericyte ablation in the cortices of EAE mice

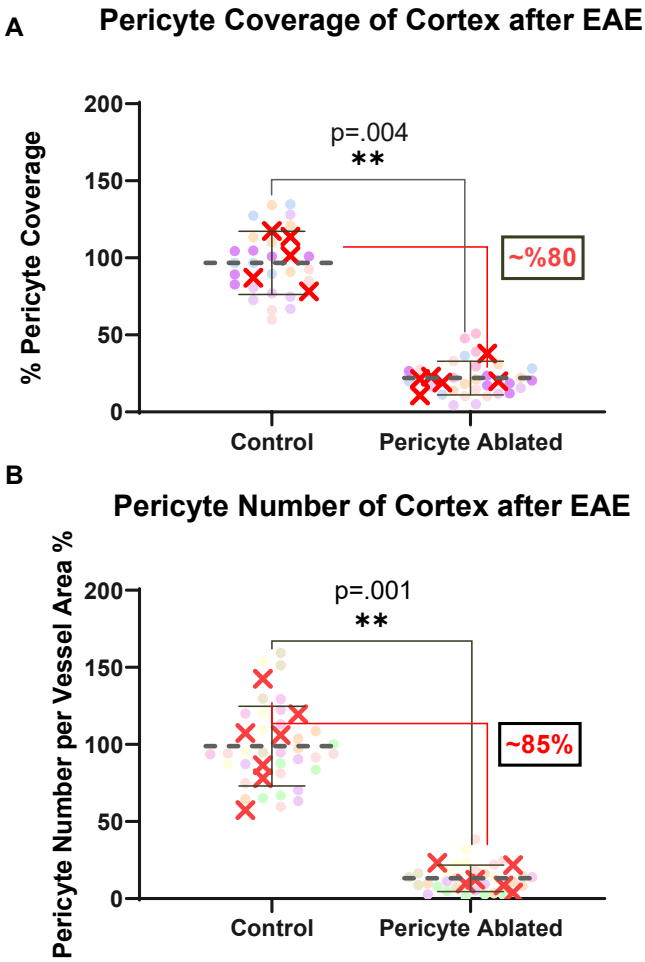

Figure 50. Pericyte coverage and number of pericyte ablated mice cortex after MOG EAE

Pericyte coverage (A) and number (B) were analyzed using confocal images of the cortex of the mice at DAY 28 of the MOG EAE and at the same time Day 43 of the pericyte ablation. Pericyte coverage was

decreased to 20%, and pericyte number was reduced to 15% in the pericyte ablated MOG EAE cortex. n=6 for the pericyte ablated group and n=5 for the control group. The x symbols on the graphs show the average of each animal, and the different colors of dots show the pericyte coverage of the individual images of each animal (5-6 images per animal). The values were normalized to the control group average value as a percentage. Statistical analysis was done by Student's t-test (two-tailed Mann-Whitney test). p=0.004 and p=0.001 for A and B, respectively. The error bars show the SDs.

The quantification of 5-6 images from 4 non-adjacent sections of cortex tissue for each EAE animal showed an 80 percent decrease in the pericyte coverage of the pericyte ablated mice with EAE compared to the wild-type EAE mice (Figure 50. A). The pericyte number analysis was also consistent with the coverage data by an 85% reduction (Figure 50. B).

3.10.2 The effect of tamoxifen on pericyte ablated and wild type mice

The pericyte ablation group of mice was administered with tamoxifen to activate the Cre recombinase and, therefore, start the diphtheria toxin's intrinsic expression. Since tamoxifen is also a toxic drug, it might cause a general health problem and weight loss in animals. To check if tamoxifen administration is a misleading factor for our weight loss assessments, a group of wild-type mice was also administered with tamoxifen. The weight graphs of the wild-type mice without tamoxifen, wild-type mice with tamoxifen, and pericyte ablated mice were compared (Figure 51).

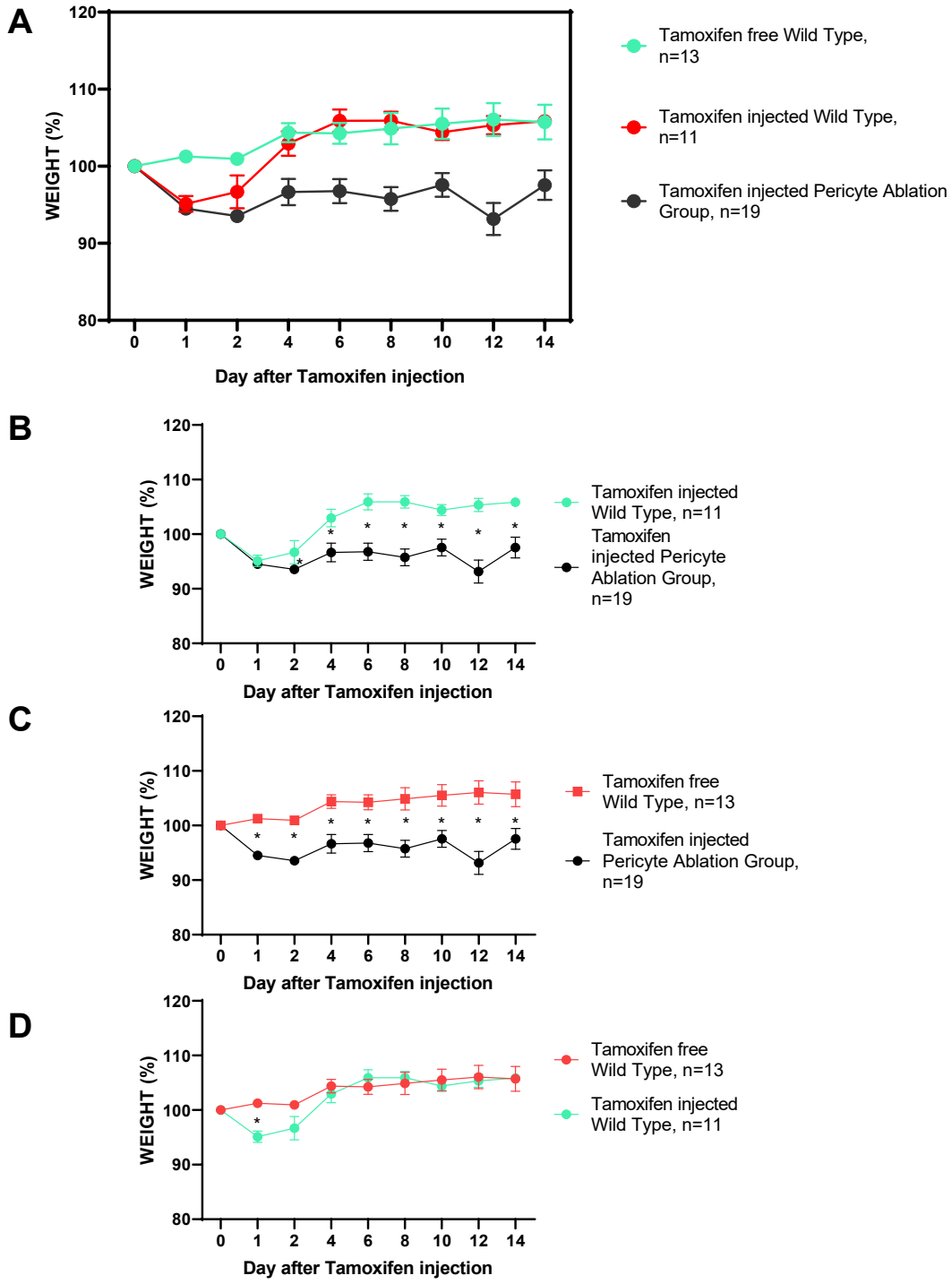

Figure 51. The effect of Tamoxifen in the wild type and pericyte ablated mice

Both the pericyte ablation model transgenic mice and wild-type mice were given tamoxifen, and the weight changes were monitored. In figure A, tamoxifen-free and injected wild-type weight graphs were compared with the tamoxifen injected, so pericyte ablated transgenic mice. In B, the difference between

the tamoxifen injected wild type, and pericyte ablation model mice were given, and the difference between the weights of the animals was significant starting from the second day. In C, Tamoxifen-free wild-type mice were compared with the pericyte ablation group and again, and this time, starting from the first day, weight differences between groups were significant. Finally, in C, tamoxifen free and the tamoxifen injected wild-type mice weight changes were compared, and only on the first day after the tamoxifen injection, the tamoxifen injected group lost significant weight, but this weight difference was not persistent for the following days, and there was no difference between the groups depending on the tamoxifen administration after the first day. The significance was assessed by the 2-way ANOVA repeated measures multiple comparison test. Statistical details are given in Appendix F. Statistical Analysis Results of Figure 51.

Weight comparisons of tamoxifen and tamoxifen-free groups revealed that the tamoxifen administration causes a consistent weight loss only for the pericyte ablated mice compared to both wild-type mice with or without tamoxifen (Figure 51 A). This weight loss is an effect of pericyte ablation but not the tamoxifen administration because wild-type mice with tamoxifen and without tamoxifen did not show any significant weight difference. There was slight but significant weight loss on the first day of the tamoxifen administration, but this weight loss was not consistent, and the weight graphs quickly evened out (Figure 51 D). Therefore, the fact that we administered the mice with tamoxifen before the EAE induction did not cause any confounding difference between the animals.

3.10.3 The effect of the tamoxifen on EAE

The tamoxifen administration as a toxin could interrupt the peripheral immunization process in the EAE model. Therefore, to eliminate this effect, we compared the wild-type EAE mice injected with tamoxifen and wild-type EAE mice without tamoxifen in terms of EAE progression.

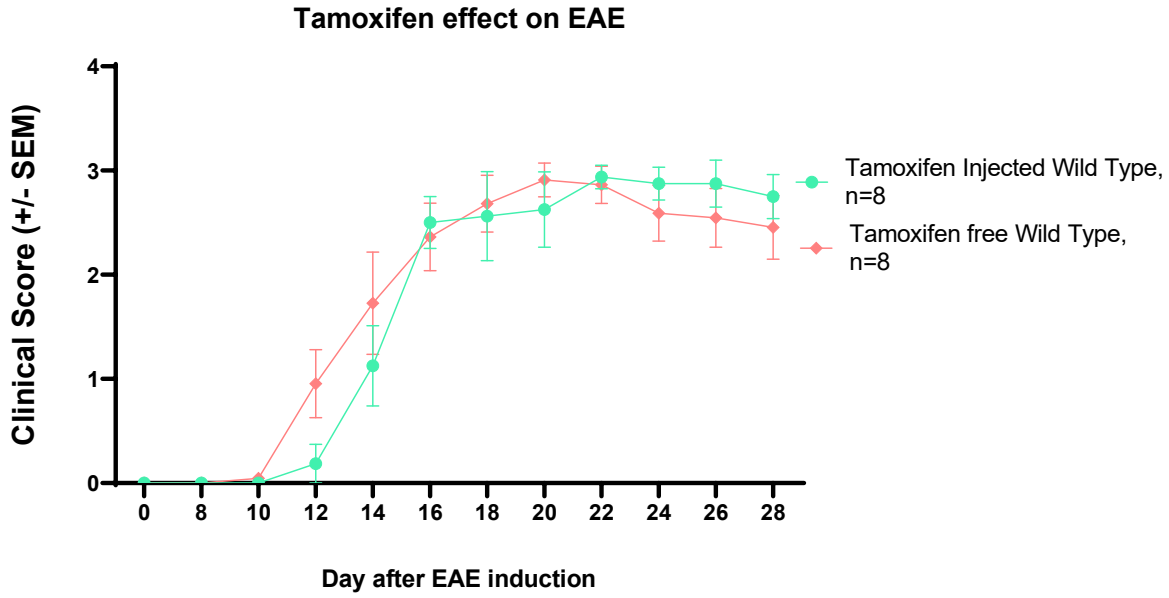

Figure 52. Tamoxifen effect on the progression of clinical symptoms of EAE in wild type mice

The effect of tamoxifen in the wild-type mice with EAE was compared in terms of clinical scores, and no differences were seen. The significance was assessed by the 2-way ANOVA repeated measures multiple comparison test. The error bars show the SEMs.

The observations of clinical scores did not reveal any difference in terms of clinical progression of the EAE in tamoxifen injected and tamoxifen-free wild-type mice. Therefore, tamoxifen did not have an impact on the EAE model efficacy (Figure 52).

3.10.4 The effect of the transgenic race on EAE

EAE is a sensitive model that could be affected by various internal or external influences such as stress, bedding changes, food type, the climate of the experimental room, etc. The model has been optimized in wild-type C57BL6/J animals, and the use of different races was reported to cause differences in the model's effectiveness. That is why we had to check if the use of our transgenic model with a mixed background affects the progression of EAE.

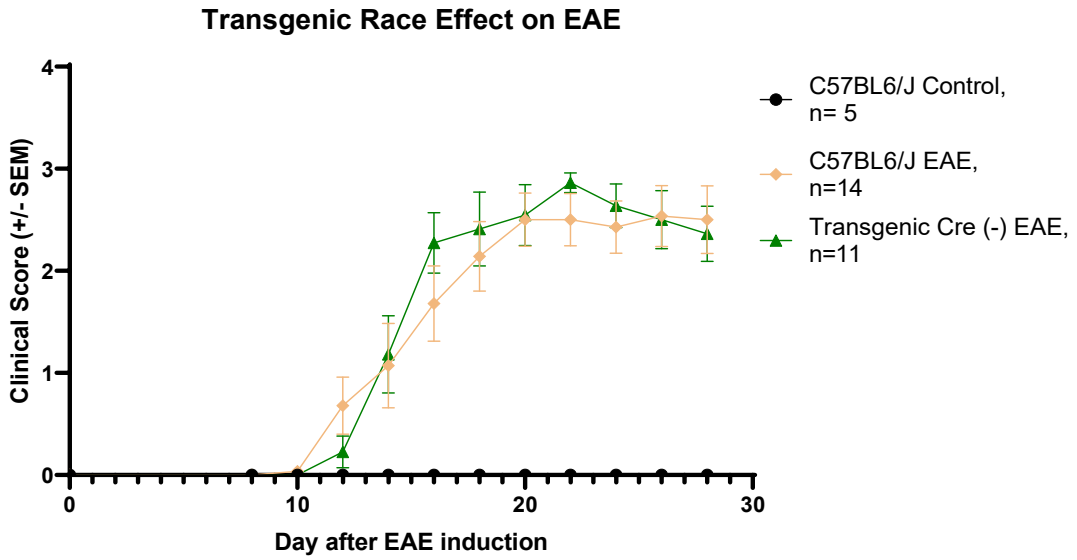

Figure 53. Race effect on the progression of clinical signs of EAE

Different races used during the experiments were compared in terms of EAE symptoms, and no difference depending on the race was seen during EAE progression in terms of clinical signs. The significance was assessed by the 2-way ANOVA repeated measures multiple comparison test. The error bars show the SEMs.

Comparison of the clinical score graphs of EAE mice with transgenic race and wild-type race revealed no difference in terms of the progression of the disease (Figure 53). Therefore, the race difference did not mislead the considerations about the EAE experiments.

CHAPTER 4

4 DISCUSSION

Pericytes are essential members of BBB. They have a variety of critical roles for the homeostasis of CNS and proper functioning of the neurovascular coupling. Correspondingly, they are related to several neurological disorders such as Alzheimer's disease, CADASIL, MS, ischemic stroke, glioblastoma multiforme, diabetic retinopathy, etc. [5,18,41,135,136]. To this day, many transgenic animal models have been used to study the function of pericytes in health and various diseases. These models focused primarily on transgenic manipulation to impose loss of function in pericyte signaling. The first model was introduced by Leven et al. as Pdgfβ$^{-/-}$ which aimed a complete loss of function in PDGFβ, the endothelial secreted molecule sensed by pericytes [64]. This model in the null mutant form was embryonic lethal. Hence, most of the studies which employed this model were irrevocably forced to focus on developmental roles of pericyte-endothelial cell interactions. However, its derivative, Pdgfβ$^{+/-}$ mouse was viable with a partial pericyte loss, but again these mice showed lots of capillary abnormalities such as microaneurysm, cylindrical dilations, and enhanced endothelial cellularity[80].

The second model of pericyte deficiency targeted the *Pdgfrβ* gene (receptor for PDGFβ) of pericytes. Similarly, these null mutant mice (Pdgfrβ$^{-/-}$) were also embryonic lethal with hemorrhagic, thrombocytopenic, and severely anemic phenotypes. Pdgfrβ$^{+/-}$ mice had a partial knock-out, presented with 27%-35% pericyte loss, and were viable [81,82]. This mouse has been reported to have diminished capillary circulation and BBB-breakdown-induced neurodegeneration[83]. Another group observed aberrant capillary circulation, but they could not explain the mechanisms of their findings because they did not detect apparent structural and functional changes in microvascular structure and reactivity as other researchers did [81]. Considering the mixed findings of the

abovementioned studies, the conclusions relied upon the usage of these models seem to be abortive.

The third model of pericyte deficiency was created by Lindblom et al. In their model, instead of deleting a major functional portion of PDGFβ protein, they targeted only the retention motive of the protein. As a result, PDGF-B binding to Heparan Sulfate Proteoglycans was disrupted in the progeny ($Pdgf\beta^{ret/ret}$). As a result, 26% less pericyte coverage[50], BBB breakdown, and pericyte loss-related LAMs increment were observed in those mice[85].

Another study investigated the role of PDGFRβ by creating point mutations in the tyrosine-binding sites for signal transduction molecules (Src, Grb2, PI3K, RasGAP, SHP-2, PLCɣ). The most popular mutation combination was the F7 mutation, in which 7 points mutations were administered, and the function of all seven transduction pathways was disrupted [82]. Increased BBB permeability and decreased blood flow were also observed in this model as in the previously mentioned models [87].

The last conventional model was endothelial-specific PDGFβ knock-out. To create this model, they used endothelial-specific Cre Recombinase expression to delete a functional part of the PDGFβ protein only in endothelial cells. The embryonic survival capacity was higher in those mice compared to the null mutant model ($Pdgf\beta^{-/-}$), but this model was inconsistent in terms of the efficacy of Cre activation and the amount of decrease in pericyte coverage[88]. Additionally, further research on endothelial-specific PDGFβ ablation reported that mutants developed organ defects such as cardiac, placental, and renal abnormalities as in the null mutants [90].

All the discussed pericyte deficiency models provide substantial contributions to the function of pericytes in both health and disease conditions. However, pericyte deficiency itself causes many structural and functional vascular changes in the CNS and throughout the body. Pericytes are required for healthy and functional BBB formation, development, maintenance. Therefore, inherently pericyte deficient mice present vascular malformations and BBB malfunction in adulthood even without any extrinsic experimental manipulations. Therefore, this condition could mislead the researchers when implementing disease models (e.g., EAE model, ischemic stroke, CSD, etc.) using those mice because the models are developed in an already disorganized biological state. Distinguishing the effect of pericyte deficiency itself

from the contribution of pericytes to the pathogenesis of the utilized disease models is a precarious task, especially for the pathologies involving loss of BBB integrity and vascular malfunctioning, including the MS disease.

In this thesis project, we aimed to investigate the role of pericytes in multiple sclerosis pathogenesis by using the combination of in vivo pericyte deficiency and neuroinflammation models. However, to be able to effectively and as naturally as possible mimic the neuroinflammation pathogenesis in pericyte deficient mice, we needed first to create an inducible pericyte ablation model which could be established in adult mice. Consequently, the mice would be intact from possible pericyte loss-related vascular side effects during embryonic development and postnatal maturation into adulthood. For our new generation pericyte ablation model, instead of targeting the signaling pathways of the pericytes (PDGFβ, PDGFRβ), we aimed to directly eliminate the pericyte cells themselves by utilizing genetic manipulations on their cell-type-specific genes. We used the Cre-LoxP system so that the PDGFRβ expressing cells would gain the ability to express the transgenic diphtheria toxin gene. So, the pericytes would go into apoptosis due to the toxic effect. To do so, we crossed PDGFRβ-P2A-CreER$^{+/-}$ (JAX Mice, 030201) and Rosa26-DTA176$^{+/+}$ (JAX Mice, 010527) and genotyped the progeny to distinguish PDGFRβ-P2A-CreER^{+} ; Rosa26-DTA176^{+} (Pericyte ablation group, Cre-positive) and PDGFRβ-P2A-CreER^{-} ; Rosa26-DTA176^{+} (Control group, Cre-negative) mice. This model is not activated unless induced because Cre Recombinase-Estrogen Receptor fusion protein (CreER) is restricted in cytoplasm unless provided with Estrogen receptor (ER) activating ligand, namely tamoxifen. After tamoxifen administration, CreER can go into the nucleus to excise the LoxP floxed sequences in the genome. In our model, this loxP floxed sequence is a transgenic stop gene inserted upstream of the transgenic DTA176 gene, inherited from the Rosa26-DTA176^{+} parent. When CreER reaches the genome, it removes the stop gene, which prevents the DTA176 functional protein translation. Upon excision of the stop codon, the DTA176 mRNA translation starts in the *Pdgfrβ* positive cells of the tamoxifen administered progeny. On the other hand, in the control progeny, mRNA of DTA176 translation stops because of the stop codon, and no toxic effects of DTA176 are observed. We have characterized a new pericyte ablation model using Cre-positive and Cre-negative progeny.

While we have been working on the characterization of our inducible pericyte ablation model, we realized that we are not the only group recognizing a need for acting upon the generation of an inducible pericyte ablation model. Zlokovic's group recently published a model of CNS-specific, inducible pericyte ablation[43]. They used the Cre-LoxP and Flp-Frt systems in tandem with a double-promoter method, employing the *Pdgfrβ* and *Cspg4 (NG2)* promoters as markers of CNS pericytes to develop a pericyte-specific line. They created two constructs: one that expressed flippase (Flp) recombinase under the control of the *Pdgfrβ* promoter, and the other one carried an Frt-Stop-Frt-CreER cassette under the control of the *Cspg4* promoter. They then co-injected both of these linearized constructs into C57BL/6 blastocysts to create Pdgfrβ-Flp; Cspg4-FSF-CreER mice (Pericyte-Cre mice). When tamoxifen was injected into those animals, they could achieve Cre Recombinase expression specific to the CNS pericytes. They crossed pericyte-CreER mice with iDTR animals harboring Cre-dependent human diphtheria toxin receptor (DTR). Injection of TAM to the progeny promoted DTR expression in brain capillaries of pericyte-CreER; iDTR mice and brain capillary pericytes were reduced when the animals were injected with DT subsequently. Using their inducible pericyte ablation model, they confirmed the previously identified characteristics of the pericyte loss phenotype, namely acute blood-brain barrier breakdown and severe blood flow loss. They also suggested a mechanism for pericyte ablation-induced rapid neuron loss. They associated the neurodegenerative pathology with loss of pericyte-derived pleiotrophin (PTN), a neurotrophic growth factor.

Following the genesis of the first inducible pericyte ablation model in 2019 by Nikolakopoulou et al., the Betsholtz group also introduced an endothelial-specific tamoxifen-inducible pericyte ablation model in 2021[140]. For their model, they crossed $Pdgf\beta^{flox/flox}$ or $Pdgf\beta^{flox/-}$ mice with endothelial-specific Cdh5(PAC)-CreERT2 mice. In the 2-months-old mice adult progeny, they imposed tamoxifen-inducible *Pdgfβ* knockout out, which eventually causes a slow progressive pericyte loss when they reach the age of 12–18 months. To elaborate, they obtained a ~50% decrease in endothelial/pericyte cell ratio, ~60% decrease in pericyte longitudinal capillary coverage, and >70% decrease in pericyte marker expression. Using that model, they again reconfirmed the role of pericytes in the maintenance of BBB and prevention of its selective permeability. They additionally showed that adult-induced loss of PDGFβ does not lead to vessel dilation, impaired arterio-venous zonation, or the formation of

microvascular calcifications, unlike observed in the constitutive developmental PDGFβ loss of function animal models. Therefore, they concluded that PDGFβ expression in quiescent adult microvascular brain endothelium is critical for maintaining pericyte coverage and normal BBB function, but that microvessel dilation, rarefaction, arterio-venous skewing, and calcification reflect developmental roles of PDGFβ.

Comparing these two inducible pericyte ablation models with our model, Zlokovic's model is more specific to CNS and also to pericytes other than the other cell types having the expression of the same markers (e.g., VSMCs). However, in their model, there is a need for an additional toxin administration to the mice that might bring upon adverse effects for the health of the animals. Betsholtz group, on the other hand, targets a signaling molecule secreted by endothelial cells but not directly targeting pericytes. Therefore, the reflection of the PDGFB ablation to pericyte coverage takes more time than the direct targeting of the pericytes. This indirect pericyte loss system is not well-controllable in terms of efficacy, timing, and consistency. In our model, direct pericytes are killed by cell-type-specific diphtheria toxin intrinsic expression. Consequently, our model is more predictable in terms of timing, dose-dependently controllable, does not require administration of any additional toxin other than tamoxifen for activation, and does not rely on any signaling pathway activity.

For the further analysis of our new pericyte ablation model, we divided animals into three different experimental groups as 2, 3, and 5 consecutive days of repeated tamoxifen injected animals. Then the short-term and long-term effects of pericyte ablation were assessed in 15 and 60 days, respectively (Figure 8). As the pericyte ablation characterization methodology, we first used immunohistochemistry and stained the brain and spinal cord tissues with CD13 for pericyte labeling and tomatolectin for the vessel labeling. Then, we calculated the pericyte coverage as the proportion of pericyte signal density to the vessel density (Figure 24, Figure 27, Figure 30, Figure 33). We also counted the pericyte number as a proportion to the tomatolectin-stained vessel area of the same confocal images. Then, we have analyzed the vessels of the same confocal images in terms of vessel area, average vessel length, and the total number of junctions by using AngioTool Software (Figure 36, Figure 37, Figure 38, Figure 39, Figure 40). Thirdly, we confirmed our pericyte coverage results with the real-time quantitative PCR technique by quantifying the decrease in the gene

expression of *Pdgfrβ* (Figure 35). Lastly, we applied Y maze and Kondziela's Inverted Screen (Grasping reflex) behavioral tests to assess the spatial memory performance changes and locomotor activity loss in our pericyte ablated mice.

As a first observation of the characterization of our pericyte ablation model, we have tracked the animals' weight changes as a parameter indicating the general health of the mice. There was a dose-proportional loss of body weight from two to five times increment of tamoxifen injections (Figure 18). Additionally, we observed a phenotype of humpback posture and hind-limb grasping reflex, especially in the five times tamoxifen injected animals. These phenotypes were less detectable as the number of tamoxifen injection repetitions decreased (Figure 34). Furthermore, the pericyte ablation induced by five consecutive doses of tamoxifen injection caused the death of the animals around 15 days. We do not have any mechanistic explanation for their abnormal phenotypes and lethality. Still, the facts that these phenotypes are noticeable in every mice of the experimental group of 5X TAM, diminution of these phenotypes with the reduction of TAM dosage and absence of the symptoms in the control groups (administered with the same dosages of TAM), altogether strongly suggest that the phenotypes led by the dose-dependent increment of pericyte coverage loss.

When the long-term weight tracking results (Figure 21) were analyzed, the significant weight loss was consistently continued, as evident in the same dose-dependent trend of the short-term weight data. In both short-term and long-term weight tracking data, two times tamoxifen injected group showed the mildest pattern in terms of the course of weight loss (Figure 18, Figure 21). Therefore, since we aimed to combine this pericyte ablation model with the EAE model, we have decided to continue with the mildest, the two times repetitive dosage of tamoxifen for further experiments.

The immunohistochemical analysis of pericyte coverage on the brain and the spinal cord vessels revealed different ratios of pericyte coverage reductions depending on the time passed after the Cre Recombinase activation and the dosage of tamoxifen. In any of the doses and time intervals, the amount of pericyte loss was significant enough to study pericyte functions. The reduction percentages are listed in Appendix H. Summary Tables of Pericyte Ablation, Table 7.

The pericyte coverage analysis results indicated that the two, three, or five-times tamoxifen administration works with the same efficiency (~75%) in terms of

diminution level in brain pericyte coverage for the acute time window (15 Days). The amount of pericyte coverage reduction remained at the same level for the cortices of the 3X TAM group for both short-term and long-term time intervals. However, for the 2X TAM group, the pericyte loss ratio monitored at Day 15, observed to be significantly reduced in the brain (30%) and in the spinal cord (15%) until Day 60 (Appendix E. Comparison of pericyte coverage loss amounts in Day15 and Day 60). This pericyte return could be the result of compensation with the induced generation of new pericytes from perivascular fibroblasts [141].

Interestingly, the quantification of the reduction in the pericyte coverage of 2X TAM in the brains of EAE mice after 43 days of Cre recombinase activation revealed an 80% decrease in the cortical pericyte coverage and an 85% decrease in the pericyte number (Figure 50 and Appendix H. Summary Tables of Pericyte Ablation, Table 8). This data shows that the pericyte ablation could not be compensated in EAE mice. This incapability could result from the inflammatory environment, which possibly precludes compensatory mechanisms efficient performance.

The pericyte coverage changes in the 2X TAM pericyte ablation group were confirmed in the gene expression level by RT-qPCR. Compared to the control mice, *Pdgfrβ* gene expression level decreased to ~90% in the cortex (Figure 35. A, B) and ~60% in the spinal cord of the pericyte ablated mice at Day 15 and Day 60. These results confirm that our pericyte ablation model is effectively working as the *Pdgfrβ* expressing cell number decreased, the mRNA level of the gene also decreased. Meanwhile, the expressions of CD31 (Figure 35. C, D) were similar between the groups, indicating that the endothelial cell numbers did not change in our induceable pericyte ablation model, as anticipated.

The initial aim of creating our inducible pericyte ablation model was to eliminate the vascular abnormalities existing in the other inherently pericyte-deficient models. Therefore, to check hypothesis fulfillment, we analyzed the morphological parameters of vasculature in our inducible pericyte ablated mice. We have not observed any significant changes in the brain and spinal cord vessel parameters for the short-term pericyte ablation group in both cortex and the spinal cord (Figure 36, Figure 37). However, in the long-term 2X TAM pericyte ablated spinal cord, we observed significant changes in the white matter. The explant area, vessel area, and the total

number of endpoints increased significantly (Figure 38). This data aligns well with the literature suggesting that the loss of pericytes engenders aberrant endothelial cell proliferation [66,67]. Correspondingly, the changes in the vascular morphology became more apparent with the increment of the tamoxifen dosage. In the cortical vessels of the 3X TAM group, the vessel percentage area has increased significantly in the short term. Additionally, vessel area, the total number of junctions, junction density, and total vessel length were also significantly increased in the cortices of the 3X TAM group in the long term (Figure 39). Lastly, the effects of pericyte ablation induced by the highest dosage of tamoxifen administration (5X TAM) were also analyzed in the short term. No significant differences were found compared to the control group. However, there was an increasing pattern in the parameters of vessel area, vessel percentage area, the total number of junctions, junction density, the total vessel length, and average vessel length (Figure 40). We could not assess the significance of these increments because the number of animals that could survive for the analysis was meager (n=2 for the control group and n=3 for the pericyte ablated group) due to the excessive pericyte ablation-related death of animals.

Upon observing phenotypic changes regarding the physical appearance of the animals (Figure 34), we also wanted to analyze the locomotor activity by using Kondziela's Inverted Screen Test (Grip Strength Test). The experiments revealed that the holding time of the 3X TAM and 5X TAM animals significantly decreased compared to the control group. However, the loss of locomotor strength was not significant in the mildest dose administered for the 2X TAM animals. These data suggest that the central or peripheral systemic effects of the pericyte ablation led to a loss of muscle strength in the animals. This could occur because of the loss of pericytes in the muscles or the loss of motor neurons in the CNS. Since we have used the unaffected 2X group, we are in the safe zone, but this effect should be considered if the higher dose-induced forms of this model are going to be used in disorders leading to muscle loss. The underlying reason for this motor deficit is not clear and needs further investigation. However, in the literature, it is shown that conventional full-body pericyte deficient mice ($Pdgf\beta^{het/het}$) have a default immune cell infiltration to the cerebellum; even though we have not tested it yet, there is a possibility that immune cell infiltration could be the case in our pericyte ablation model too[85]. Hypothetically,

the possible inflammation-induced neurodegeneration in the cerebellum could be the reason for the loss of muscle coordination.

After we optimized and characterized our new-generation inducible pericyte ablation model, we induced an EAE model on them to fulfill our second aim of exploring the role of pericytes during neuroinflammation. By comparing the clinical score and weight graphs of the wild-type EAE and pericyte EAE mice, we deduced the extant effect of the pericyte loss on neuroinflammation. In the clinical score observations, although the first clinical symptoms similarly developed and worsened up to score 1.5 for both groups at the same trend, the exacerbation rate was higher in the pericyte ablated mice after that point. Consequently, the clinical score of pericyte ablated mice reached a higher peak than the wild-type EAE mice. At the recovery stage, despite the recovery trend in both groups being similar, the pericyte ablated EAE mice did not recover as much as the wild-type EAE mice (Figure 46 A). These EAE clinical progression data suggest that the lack of pericytes did not make a difference in terms of exceeding the infiltration threshold necessary for clinical symptoms initiation. However, the higher clinical progression rate and worse clinical symptoms observed in pericyte ablated mice implicate that the pericyte loss might disturb the anti-inflammatory processes that suppress the inflammation. The alternative/simultaneous possibility is that the initial BBB impairment related to poorer pericyte coverage might facilitate the immense immune cell infiltration into the CNS at the beginning of the disease. Therefore, after that amount of infiltration, the anti-inflammatory mechanisms could fail to suppress the enormous inflammatory progression. In vein with this assumption, the literature shows that the pericyte ablation increases ICAM1 and VCAM1 expression in the endothelial cells, so the intensity of inflammatory cell entrance into the CNS increases upon EAE induction[85]. However, the expression levels of LAMs in our model should be checked to confidently claim that the increase in the leucocyte entrance is the mechanism for the observed severe presentations in the EAE clinical symptoms of the pericyte ablated mice.

Corresponding to the clinical score data, we observed that both pericyte ablated mice and the wild-type mice with EAE lose weight compared to the vehicle-injected controls. However, pericyte ablated EAE mice lost significantly more weight than wild-type EAE mice (Figure 46 B). This difference was not because of only pericyte ablation

according to our EAE control groups. We analyzed the weight difference between the EAE controls of pericyte ablated and wild-type animals without MOG administration (but with EAE vehicle injection). No significant weight difference was observed in those mice only because of the pericyte ablation (Figure 46C). Therefore, we could conclude that the weight difference observed is not due to the effect of the pericyte ablation itself but to the pericyte-loss-induced broken mechanisms during EAE. Furthermore, our correlation analysis of weight data and the clinical score of wild-type C57BL/6 mice showed a significant negative correlation between the intensity of the clinical presentation of disease and the weight gain of the animals. Therefore, we can infer that the significantly more weight loss of pericyte ablated mice was related to the more intense inflammation they experienced during EAE. This data suggests that the observational clinical score data was trusted in objectivity and accuracy.

The wild-type EAE mice gained control of their feet and arms back, but with spasticity that obstructed normal walking in the recovery stage. However, pericyte ablated mice underwent more muscle loss due to the paralyzing effect of EAE, and even though they were able to move their limbs upon external stimulation, they could not stand on them or adequately use them (Figure 47). Additionally, the furs remained sticky, resulting from stopped self-grooming behavior performed for self-cleaning. The self-care, self-feeding, and movement capacity decreased to a critical level, and we needed to terminate our experiment earlier than the planned schedule due to ethical reasons. The phenotypes that pericyte ablated mice demonstrated were not included in the standardized EAE scoring criteria. Therefore, according to the limitation of conventional scoring guidelines, the actual difference between the clinical presentation of pericyte ablated and control mice could not be represented accurately enough.

Immunohistochemical analysis of the spinal cord tissues by the pericyte marker CD13 and cell body stain Hoechst revealed that pericyte ablated mice had more and larger lesions of immune cell accumulations than those observed in the lesions of wild-type EAE mice (Figure 48). According to the literature, pericytes are known to function in scar formation, separation, and restriction of the injured tissues from the healthy parenchyma [73]. Therefore, our observation could be explained by the differentiation of remained pericytes into the myofibroblast-like cells and their migration into the damaged areas.

Lastly, as it is known, the MOG EAE model does not develop any lesions in the brain but in the spinal cord only, and this is a pathological difference of the EAE model from the human MS. However, interestingly, we observed some unexpected periventricular immune cell infiltrations in the brains of the pericyte ablated mice with EAE (Figure 49). This pathological phenotype better reflects the radiological presentation of human MS with periventricular lesions. This data suggests that the brain pericyte deficiency might be happening before the T cell entry to the brain parenchyma in the human MS pathogenesis. In the literature, cerebellar lesions were also observed in the EAE model of conventional Pdgfβ$^{ret/ret}$ mice with atypical EAE presentation and ataxia symptoms. Additionally, they reported the lack of spinal cord lesions in those mice. They explained these findings with the difference between the pericyte ablation efficiency of the brain and the spinal cord. They suggested that the brain, which loses more pericyte coverage than the spinal cord, becomes more vulnerable to immune cell infiltration in the case of pericyte deficiency[85]. However, in our model, both the periventricular and the spinal cord lesions are observed even though there is a similar way of difference in the ablation ratios of the brain and the spinal cord (75% to 45% in the short-term and 45% to 25% in the long term, respectively) as in the case of Pdgfβ$^{ret/ret}$ mice (75% to 26%). Furthermore, we did not observe atypical EAE, but our mice reflected typical EAE with more severe symptoms. Therefore, our model represents the pericyte deficiency effect in human MS better than the EAE study with the conventional model of pericyte deficiency.

A variety of internal controls were used to eliminate any possible side effects of the experimental procedures, such as Cre activation, tamoxifen administration, and usage of different races. Weight gain comparisons of tamoxifen and tamoxifen-free groups revealed that the tamoxifen administration causes a consistent weight loss only for the pericyte ablated mice compared to both wild-type mice with or without tamoxifen (Figure 51 A). This weight loss is an effect of pericyte ablation but not the tamoxifen administration because wild-type mice with tamoxifen and without tamoxifen did not show any significant weight differences. On the first day of the tamoxifen administration, there was slight but significant weight loss, but this observation was not consistent, and the weight graphs quickly evened out for both groups (Figure 51 D). Therefore, the fact that we administered the mice with tamoxifen before the EAE induction did not cause any confounding effects for our experimental

findings. Secondly, we thought that the intraperitoneal tamoxifen administration as a toxin could interrupt the peripheral immunization process in the EAE model. Therefore, to eliminate this effect, we compared the wild-type EAE mice injected with tamoxifen and wild-type EAE mice without tamoxifen in terms of EAE progression. The observations of clinical scores did not reveal any difference between the data for those mice regarding the clinical progression of the EAE. Therefore, tamoxifen did not impact the EAE model efficacy (Figure 52). Lastly, since the EAE model has been optimized in wild-type C57BL6/J animals, and previously, different races were reported to have variations in the model's effectiveness, we had to check if the use of our transgenic model with a mixed background affects the progression of EAE. Comparison of the clinical score graphs of EAE mice with transgenic and wild-type races revealed no difference in the progress of the disease (Figure 53). Therefore, the race difference did not interfere with considerations about the EAE experiments in our transgenic animal race.

This thesis project has created a very advantageous pericyte ablation model compared to other conventional and new inducible models. However, our model also has some disadvantages and limitations. First of all, pericytes do not have a specific marker, and in our pericyte ablation model, we are only targeting the *Pdgfrβ* marker of pericytes. However, the only cells that express *Pdgfrβ* are not CNS pericytes, but VSMCs, MC Cells (MSCs), and perivascular fibroblasts also express *Pdgfrβ.* Therefore, there is a possibility that the Cre-induced ablation can also affect these cell types.

Additionally, *Pdgfrβ*-positive pericyte is not exclusively found in CNS. Peripheral organs of the body, such as the kidney, liver, heart, muscles, etc., also have pericytes with a less pericyte/endothelial cell ratio than the retina and CNS. Therefore, even though our model has successfully maneuvered the developmental side effects of the conventional pericyte deficiency models, it could not bypass the problem of exclusivity to CNS similar to the other extant models, except the newly introduced double promoter inducible model of Zlokovic's Laboratory [43]. However, we have no idea of the possible limitation exerted by this issue as we did not quantify the pericyte loss in the peripheral organs for our model yet.

Since the EAE model also has a peripheral immunization component in itself, in our study, we could not be completely confident about if the observed differences are related to pericyte loss of CNS or the peripheral immune organs (e.g., spleen). We tried to bypass this pitfall by using the advantage of the dose-dependent controllability feature of our model. We used the lowest level of pericyte ablation (by 2X TAM) to target the cells that express Pdgfrβ marker in the highest level (pericytes) and the body parts that these cells are abundant the most (e.g., retina and brain). The dose-dependent variability of the effect size in our model pericyte ablation could also be considered advantageous. For instance, by using our pericyte ablation model, one can study the effects of pericyte loss in the peripheral diseases of the other organs by optimizing the dosage accordingly.

In the EAE studies, we have used the standard EAE scoring, but the symptoms of the pericyte ablated mice differed from the standardized symptoms. Therefore, we could not represent the actual amount of differences by using the existing system. Other than this limitation, even though we showed that pericytes have a protective role in neuroinflammation, we do not have a mechanistic explanation for that function yet.

CHAPTER 5

5 CONCLUSION

In this thesis project, we initially aimed to design an innovative inducible pericyte ablation model that would overcome the developmental deficiencies (BBB leakage, vascular and renal problems) of existing pericyte deficiency models used in the pericyte research. We planned to achieve this aim using a cell-type and time-specific CreER-LoxP system in combination with the chemical toxin genetic ablation approach. The transgenic mice used in a way that the cells expressing the *Pdgfrβ* gene (the most prominent marker of pericytes) would be ablated by the diphtheria toxin-induced apoptosis upon the trigger of Cre Recombinase activation by tamoxifen. We are the first group to use this approach to directly target the viability of pericytes in mice without requiring external toxin administration. Based on the quantitative analysis of pericyte coverage and count, we can confidently argue that we have successfully implemented the CNS endothelial pericyte coverage loss with ~75% efficiency in the cortex and ~45% efficiency in the spinal cord. In terms of gene expression profile, *Pdgfrβ* mRNA levels were decreased to ~10% in the cortex, and ~40% in the spinal cord in the pericyte ablated mice.

Meanwhile, vessel morphology and endothelial cell marker, CD31, expression levels composition remained unchanged after the acute pericyte ablation in our model with mild induction (2X TAM). If the correct dosage is used to induce diphtheria toxin expression, the implemented pericyte ablation is compatible with life, and our pericyte ablation model is conducive for additional manipulations. These properties make our model favorable to all other inherently pericyte deficiency models because acute pericyte ablation is isolated from all other secondary developmental deficiencies of BBB and vasculature. Our model would potentially better represent the effect of pericyte deficiency on *in vivo* loss of function studies of various CNS diseases.

In the second part of the thesis, we investigated the effect of acute pericyte loss in neuroinflammation as the project's main aim. We used an inducible pericyte ablation model with the EAE model of MS-like neuroinflammation for the first time ever. The clinical score and weight changes of the pericyte ablated mice and the wild-type EAE mice were compared to see the pericyte loss induced variations. The experimental results clearly illustrated that the pericytes have a protective role in the resolution of neuroinflammation. The further observation of the immunohistochemical stainings of the spinal cord and brain tissues of EAE mice supported our initial observations. The intensity and the spread of the spinal cord lesions were exaggerated in the absence of pericytes. Also, as exclusive to the pericyte ablated group with EAE, unexpected periventricular lesions were observed in the brain. Since the periventricular lesions reflect the radiological phenotype of the human MS, we concluded that EAE in our inducible pericyte ablation model mimicked the human MS radiological symptoms better than any other model. This finding suggested that the pericyte deficiency could be the initial event that makes MS patients susceptible to infiltration of the immune cells to the brain parenchyma.

The inducible pericyte ablation model we implemented here is a unique design and effective model for pericyte research, and it is adjustable to study a variety of vascular dysfunction-involved diseases. To better understand the implications of our model, future studies should address whether BBB leakage, cerebral blood flow dysregulation, and default immune cell infiltration are present in our model due to the acute ablation of pericytes. The degree of cell-type specificity to pericytes and CNS should also be further characterized. The mechanism of the 5X TAM group of pericyte ablated animals' lethality should be identified. Additionally, unearthing the partial recovery observation in the pericyte ablation of the 2X TAM group from Day15 to Day 60 is still an unfathomed necessity. For the findings related to EAE presentation in our pericyte ablated mice, the particular mechanism of more significant muscle loss observation in pericyte ablated mice and the specific way of protection that pericytes provided during EAE need a deeper investigation.

As of final remark in my thesis, I want to emphasize that, together, the findings of my thesis suggest that the pericyte deficiency in MS is a significant pathology that should be addressed in the diagnostics and the therapeutic approaches towards MS

clinics. According to my research findings, pericyte coverage protects the brain from the progression of MS pathogenesis. This information provides a precious insight into our understanding of MS pathology and related-pericyte functions. Additionally, a valuable new pericyte deficiency of adult mice was introduced to the realm of pericyte research, and I believe my model would be implicated in the studies of a wide range of diseases from now on.

APPENDIX

Appendix A. The MATLAB Codes, used for the pericyte Coverage Analysis

```
close all;
clc;
% Opening Tiff File
Directory ='C:\Users\dilatak\Desktop\1\1';
mkdir 2X_D15
save_dir='C:\Users\dilatak\Desktop\1\2X_D15';
Folder=Directory;
files=dir(Directory);
Tablo=[];
goruntu="on";
%% Waitbar
WW=waitbar(0,'Image Processing Starts');
N=length(files);
%% Processing Loop
for i=3:N
%% Waitbar
  rtnum=num2str(i);
  RTnum=num2str(N);
  rtnum=strcat('Current Image Number: ',{' '},rtnum);
  RTnum=strcat('Total Number of Images: ',RTnum);
  disp=string({rtnum,RTnum});
  waitbar(i/N,WW,disp)
%% File acquisition
filename = files(i);
File=filename.name;
[X1,map1] = imread(fullfile(Folder, File),'TIF',1);
[X2,map2] = imread(fullfile(Folder, File),'TIF',2);
[X3,map3] = imread(fullfile(Folder, File),'TIF',3);
[X4,map4] = imread(fullfile(Folder, File),'TIF',4);
[X5,map5] = imread(fullfile(Folder, File),'TIF',5);
[X6,map6] = imread(fullfile(Folder, File),'TIF',6);
%% Channel arrangement
rgbImage1 = X1;
% Extract color channels.
redChannel1 = rgbImage1(:,:,1); % Red channel
greenChannel1 = rgbImage1(:,:,2); % Green channel
blueChannel1 = rgbImage1(:,:,3); % Blue channel

rgbImage2 = X2;
% Extract color channels.
redChannel2 = rgbImage2(:,:,1); % Red channel
greenChannel2 = rgbImage2(:,:,2); % Green channel
blueChannel2 = rgbImage2(:,:,3); % Blue channel

rgbImage3 = X3;
% Extract color channels.
redChannel3 = rgbImage3(:,:,1); % Red channel
greenChannel3 = rgbImage3(:,:,2); % Green channel
```

```
blueChannel3 = rgbImage3(:,:,3); % Blue channel

rgbImage4 = X4;
% Extract color channels.
redChannel4 = rgbImage4(:,:,1); % Red channel
greenChannel4 = rgbImage4(:,:,2); % Green channel
blueChannel4 = rgbImage4(:,:,3); % Blue channel

rgbImage5 = X5;
% Extract color channels.
redChannel5 = rgbImage5(:,:,1); % Red channel
greenChannel5 = rgbImage5(:,:,2); % Green channel
blueChannel5 = rgbImage5(:,:,3); % Blue channel

rgbImage6 = X6;
%% Channel Extract
redChannel6 = rgbImage6(:,:,1); % Red channel
greenChannel6 = rgbImage6(:,:,2); % Green channel
blueChannel6 = rgbImage6(:,:,3); % Blue channel
%% Channel OVERLAP
red =
cat(3,redChannel1,redChannel2,redChannel3,redChannel4,redChannel5,red
Channel6);
green =
cat(3,greenChannel1,greenChannel2,greenChannel3,greenChannel4,greenCh
annel5,greenChannel6);
blue =
cat(3,blueChannel1,blueChannel2,blueChannel3,blueChannel4,blueChannel
5,blueChannel6);
%% max
redmax = max(red,[],3);
greenmax = max(green,[],3);
bluemax = max(blue,[],3);
%% Gaussian Filter
sigma=2;
red_filtered = imgaussfilt(redmax,sigma);
green_filtered = imgaussfilt(greenmax,sigma);
%% Histogram
bin=50;
[red_hist]=imhist(red_filtered,bin);
[green_hist]=imhist(green_filtered,bin);
%% Triangle
red_triangle=triangle_th(red_hist,bin);
green_triangle=triangle_th(green_hist,bin);
%% Thresholded Image Generation
red_thresh=imbinarize(red_filtered,red_triangle);
green_thresh=imbinarize(green_filtered,green_triangle);
%% Create Mask
% red_mask=1 - red_thresh;
% green_mask=1 - green_thresh;
% figure
% imshow(red_mask)
%% Pixel extraction
pixel=50; % PIXEL^2
red_cleared = bwareaopen(red_thresh,pixel);
green_cleared = bwareaopen(green_thresh,pixel);
% figure
% imshow(1-red_cleared)
%% Display
```

```
if goruntu=="on"
    figure(1)
    subplot(2,2,1), imshow(redmax)
    subplot(2,2,2), imshow(red_cleared)
    subplot(2,2,3), imshow(greenmax)
    subplot(2,2,4), imshow(green_cleared)
    fig_name=strcat(File,'_panel','.tif');
    saveas(gcf,fullfile(save_dir,fig_name))
end
%% Image Save Cleared
im_name_red=strcat(File,'_red_triangle','.tif');
imwrite(red_cleared,fullfile(save_dir,im_name_red),'tif')
im_name_green=strcat(File,'_green_triangle','.tif');
imwrite(green_cleared,fullfile(save_dir,im_name_green),'tif')

%% Processing the Table
[labeledImage1, numBlobs1] = bwlabel(red_cleared);
props1 =
regionprops(labeledImage1,red_filtered,'Area','MeanIntensity','PixelV
alues');
allRedAreas = [props1.Area];
allRedMeans = [props1.MeanIntensity];
TotalRedMeanPixelValues = mean(allRedMeans);
totalRedArea = sum(allRedAreas);
RedAreaPercent = totalRedArea/(512*512);
allRedIGLs = allRedAreas .* allRedMeans;
RedIntDent = sum(allRedIGLs);

[labeledImage2, numBlobs2] = bwlabel(green_cleared);
props2 = regionprops(labeledImage2,
green_filtered,'Area','MeanIntensity','PixelValues');

allGreenAreas = [props2.Area];
allGreenMeans = [props2.MeanIntensity];
TotalGreenMeanPixelValues = mean(allGreenMeans);
totalGreenArea = sum(allGreenAreas);
GreenAreaPercent = totalGreenArea/(512*512);
allGreenIGLs = allGreenAreas .* allGreenMeans;
GreenIntDent = sum(allGreenIGLs);

PericyteDensity = (sum(allRedIGLs)/sum(allGreenIGLs)* 100);

% Writing Excel
name=string(File);


Tablo = [Tablo;name,totalRedArea, RedAreaPercent,
TotalRedMeanPixelValues, RedIntDent, totalGreenArea,
GreenAreaPercent, TotalGreenMeanPixelValues,
GreenIntDent,PericyteDensity];

end
close(WW)
close(figure(1))
header=["name","totalRedArea","RedAreaPercent","TotalRedMeanPixelValu
es","RedIntDent","totalGreenArea","GreenAreaPercent","TotalGreenMeanP
ixelValues", "GreenIntDent","PericyteDensity"];
Tablo=[header;Tablo];
```

```
Tablo=table(Tablo);
writetable(Tablo,strcat('2X_D15','.xls'),'Sheet',1,'Range',strcat('A1
','':K4000''))
```

Appendix A. 1. The complementary function for the triangle thresholding

```
function [level]=triangle_th(lehisto,num_bins)
%     Triangle algorithm
%     This technique is due to Zack (Zack GW, Rogers WE, Latt SA
(1977),
%     "Automatic measurement of sister chromatid exchange frequency",
%     J. Histochem. Cytochem. 25 (7): 741?53, )
%     A line is constructed between the maximum of the histogram at
%     (b) and the lowest (or highest depending on context) value (a)
in the
%     histogram. The distance L normal to the line and between the
line and
%     the histogram h[b] is computed for all values from a to b. The
level
%     where the distance between the histogram and the line is
maximal is the
%     threshold value (level). This technique is particularly
effective
%     when the object pixels produce a weak peak in the histogram.
%     Use Triangle approach to compute threshold (level) based on a
%     1D histogram (lehisto). num_bins levels gray image.
%     INPUTS
%         lehisto :   histogram of the gray level image
%         num_bins:   number of bins (e.g. gray levels)
%     OUTPUT
%         level   :   threshold value in the range [0 1];
%
%     Dr B. Panneton, June, 2010
%     Agriculture and Agri-Food Canada
%     St-Jean-sur-Richelieu, Qc, Canad
%     bernard.panneton@agr.gc.ca
%   Find maximum of histogram and its location along the x axis
    [h,xmax]=max(lehisto);
    xmax=round(mean(xmax));   %can have more than a single value!
    h=lehisto(xmax);

%   Find location of first and last non-zero values.
%   Values<h/10000 are considered zeros.
    indi=find(lehisto>h/10000);
    fnz=indi(1);
    lnz=indi(end);
%   Pick side as side with longer tail. Assume one tail is longer.
    lspan=xmax-fnz;
    rspan=lnz-xmax;
    if rspan>lspan  % then flip lehisto
        lehisto=fliplr(lehisto');
        a=num_bins-lnz+1;
        b=num_bins-xmax+1;
        isflip=1;
    else
        lehisto=lehisto';
        isflip=0;
```

```
        a=fnz;
        b=xmax;
    end

%   Compute parameters of the straight line from first non-zero to
peak
%   To simplify, shift x axis by a (bin number axis)
    m=h/(b-a);

%   Compute distances
    x1=0:(b-a);
    y1=lehisto(x1+a);
    beta=y1+x1/m;
    x2=beta/(m+1/m);
    y2=m*x2;
    L=((y2-y1).^2+(x2-x1).^2).^0.5;
%   Obtain threshold as the location of maximum L.
    level=find(max(L)==L);
    level=a+mean(level);

%   Flip back if necessary
    if isflip
        level=num_bins-level+1;
    end

    level=level/num_bins
```

Appendix B. The ImageJ macro for the vessel analysis

```
open("C:/Users/dilatak/Desktop/1/1.tif");
selectWindow("");
run("Z Project...", "projection=[Max Intensity]");
selectWindow("1.tif");
close();
selectWindow("1.tif");
run("Gaussian Blur...", "sigma=2");
run("8-bit");
run("Auto Threshold", "method=Triangle white");
setOption("BlackBackground", false);
run("Convert to Mask");
run("Analyze Particles...", "size=20-Infinity pixel show=Masks");
saveAs("Tiff", "C:/Users/dilatak/Desktop/1.tif")
```

Appendix C. Statistical Analysis Results of Figure 18

Compare each cell mean with the other cell mean in that row								
Number of families	1							
Number of comparisons per family	4							
Alpha	0.05							
Sidak's multiple comparisons test	**Mean Diff.**	**95.00% CI of diff.**	**Significant?**	**Summary**	**Adjusted P Value**			
Cre (+)_3X TAM - Cre (+)_2X TAM								
DAY1	-0.9852	-3.289 to 1.319	No					
Day4	-6.009	-8.239 to -3.780	Yes					
Day9	-12.09	-15.75 to -8.433	Yes					
Day14	-13.11	-17.41 to -8.812	Yes					
Test details	**Mean 1**	**Mean 2**	**Mean Diff.**	**SE of diff.**	**N1**	**N2**	**t**	**DF**
Cre (+)_3X TAM - Cre (+)_2X TAM								
Day0								
DAY1	97.53	98.52	-0.9852	1.125	21	22	0.8754	28.42
Day4	96.28	102.3	-6.009	1.090	21	22	5.512	29.13
Day9	92.52	104.6	-12.09	1.794	21	22	6.741	30.74
Day14	90.26	103.4	-13.11	2.092	21	22	6.267	26.15

Compare each cell mean with the other cell mean in that row								
Number of families	1							
Number of comparisons per family	4							
Alpha	0.05							
Sidak's multiple comparisons test	**Mean Diff.**	**95.00% CI of diff.**	**Significant?**	**Summary**	**Adjusted P Value**			
Cre (+)_5X TAM - Cre (+)_2X TAM								
DAY1	0.2719	-2.916 to 3.460	No					
Day4	-2.897	-7.488 to 1.694	No					
Day9	-12.31	-16.46 to -8.168	Yes					
Day14	-16.08	-20.67 to -11.49	Yes					
Test details	**Mean 1**	**Mean 2**	**Mean Diff.**	**SE of diff.**	**N1**	**N2**	**t**	**DF**
Cre (+)_5X TAM - Cre (+)_2X TAM								
Day0								
DAY1	98.79	98.52	0.2719	1.504	14	22	0.1809	15.95
Day4	99.39	102.3	-2.897	2.146	14	22	1.350	14.38
Day9	92.30	104.6	-12.31	1.979	14	22	6.221	18.91
Day14	87.29	103.4	-16.08	2.172	14	22	7.405	16.79

Compare each cell mean with the other cell mean in that row								
Number of families	1							
Number of comparisons per family	4							
Alpha	0.05							
Sidak's multiple comparisons test	**Mean Diff.**	**95.00% CI of diff.**	**Significant?**	**Summary**	**Adjusted P Value**			
Cre (+)_5X TAM - Cre (+)_3X TAM								
DAY1	1.257	-2.350 to 4.864	No					
Day4	3.112	-1.726 to 7.951	No					
Day9	-0.2198	-5.098 to 4.658	No					
Day14	-2.969	-8.705 to 2.766	No					
Test details	**Mean 1**	**Mean 2**	**Mean Diff.**	**SE of diff.**	**N1**	**N2**	**t**	**DF**
Cre (+)_5X TAM - Cre (+)_3X TAM								
Day0								
DAY1	98.79	97.53	1.257	1.753	14	21	0.7172	25.38
Day4	99.39	96.28	3.112	2.310	14	21	1.348	18.74
Day9	92.30	92.52	-0.2198	2.387	14	21	0.09209	29.53
Day14	87.29	90.26	-2.969	2.812	14	21	1.056	30.89

Appendix D. Statistical Analysis Results of Figure 21

Mixed-effects analysis Multiple comparisons								
Compare each cell mean with the other cell mean in that row								
Number of families	1							
Number of comparisons per family	9							
Alpha	0.05							
Sidak's multiple comparisons test	**Mean Diff.**	**95.00% CI of diff.**	**Significant?**	**Summary**	**Adjusted P Value**			
Control - 2X Tam.								
Row 6	2.680	-0.8778 to 6.237	No					
Row 10	3.657	-0.1614 to 7.475	No					
Row 16	1.478	-3.329 to 6.285	No					
Row 24	3.117	-1.011 to 7.245	No					
Row 30	4.072	-0.3374 to 8.481	No					
Row 36	5.880	0.3574 to 11.40	Yes					
Row 44	7.340	1.025 to 13.65	Yes					
Row 51	6.704	-0.09757 to 13.51	No					
Row 59	7.459	2.288 to 12.63	Yes					
Test details	**Mean 1**	**Mean 2**	**Mean Diff.**	**SE of diff.**	**N1**	**N2**	**t**	**DF**
Control - 2X Tam.								
Row 1								
Row 6	100.5	97.80	2.680	1.748	24	11	1.533	32.90
Row 10	104.7	101.1	3.657	1.877	24	11	1.949	32.98
Row 16	102.5	101.0	1.478	2.340	24	11	0.6318	26.33
Row 24	103.7	100.6	3.117	2.022	24	11	1.541	30.35
Row 30	104.1	100.0	4.072	2.165	24	11	1.881	32.18
Row 36	106.2	100.3	5.880	2.714	24	11	2.167	32.81
Row 44	108.7	101.4	7.340	3.069	18	11	2.392	25.49
Row 51	106.5	99.85	6.704	3.299	18	11	2.032	24.53
Row 59	109.6	102.2	7.459	2.517	18	11	2.963	26.27

Mixed-effects analysis Multiple comparisons								
Compare each cell mean with the other cell mean in that row								
Number of families	1							
Number of comparisons per family	9							
Alpha	0.05							
Sidak's multiple comparisons test	**Mean Diff.**	**95.00% CI of diff.**	**Significant?**	**Summary**	**Adjusted P Value**			
Control - 3X Tam.								
Row 6	3.060	-0.7436 to 6.864	No					
Row 10	9.576	4.196 to 14.96	Yes					
Row 16	7.938	3.230 to 12.65	Yes					
Row 24	6.983	2.953 to 11.01	Yes					
Row 30	11.67	7.586 to 15.76	Yes					
Row 36	14.18	8.752 to 19.60	Yes					
Row 44	11.22	4.991 to 17.45	Yes					
Row 51	8.752	2.494 to 15.01	Yes					
Row 59	11.10	4.573 to 17.63	Yes					
Test details	**Mean 1**	**Mean 2**	**Mean Diff.**	**SE of diff.**	**N1**	**N2**	**t**	**DF**
Control - 3X Tam.								
Row 1								
Row 6	100.5	97.42	3.060	1.865	24	10	1.641	30.92
Row 10	104.7	95.15	9.576	2.577	24	10	3.716	19.69
Row 16	102.5	94.57	7.938	2.287	24	10	3.470	25.29
Row 24	103.7	96.71	6.983	1.972	24	10	3.541	29.58
Row 30	104.1	92.44	11.67	2.005	24	10	5.820	31.99
Row 36	106.2	91.99	14.18	2.663	24	10	5.324	31.84
Row 44	108.7	97.48	11.22	3.022	18	10	3.713	24.52
Row 51	106.5	97.80	8.752	3.039	18	10	2.880	25.06
Row 59	109.6	98.52	11.10	3.148	18	10	3.526	22.10

	2way ANOVA Multiple comparisons								
1	Compare each cell mean with the other cell mean in that row								
2									
3	Number of families	1							
4	Number of comparisons per family	9							
5	Alpha	0.05							
6									
7	**Sidak's multiple comparisons test**	**Mean Diff.**	**95.00% CI of diff.**	**Significant?**	**Summary**	**Adjusted P Value**			
8									
9	2X Tam. - 3X Tam.								
10	Row 6	0.3809	-2.680 to 3.441	No					
11	Row 10	5.919	0.9470 to 10.89	Yes					
12	Row 16	6.460	1.503 to 11.42	Yes					
13	Row 24	3.866	0.01278 to 7.719	Yes					
14	Row 30	7.600	4.051 to 11.15	Yes					
15	Row 36	8.297	3.755 to 12.84	Yes					
16	Row 44	3.882	-0.5453 to 8.309	No					
17	Row 51	2.048	-4.493 to 8.589	No					
18	Row 59	3.641	-2.110 to 9.393	No					
19									
20									
21	**Test details**	**Mean 1**	**Mean 2**	**Mean Diff.**	**SE of diff.**	**N1**	**N2**	**t**	**DF**
22									
23	2X Tam. - 3X Tam.								
24	Row 1								
25	Row 6	97.80	97.42	0.3809	1.456	11	10	0.2616	17.87
26	Row 10	101.1	95.15	5.919	2.310	11	10	2.562	13.51
27	Row 16	101.0	94.57	6.460	2.368	11	10	2.728	19.00
28	Row 24	100.6	96.71	3.866	1.841	11	10	2.100	19.00
29	Row 30	100.0	92.44	7.600	1.692	11	10	4.492	18.40
30	Row 36	100.3	91.99	8.297	2.170	11	10	3.824	19.00
31	Row 44	101.4	97.48	3.882	2.115	11	10	1.835	19.00
32	Row 51	99.85	97.80	2.048	3.122	11	10	0.6559	18.74
33	Row 59	102.2	98.52	3.641	2.692	11	10	1.352	14.63

Appendix E. Comparison of pericyte coverage loss amounts in Day15 and Day 60

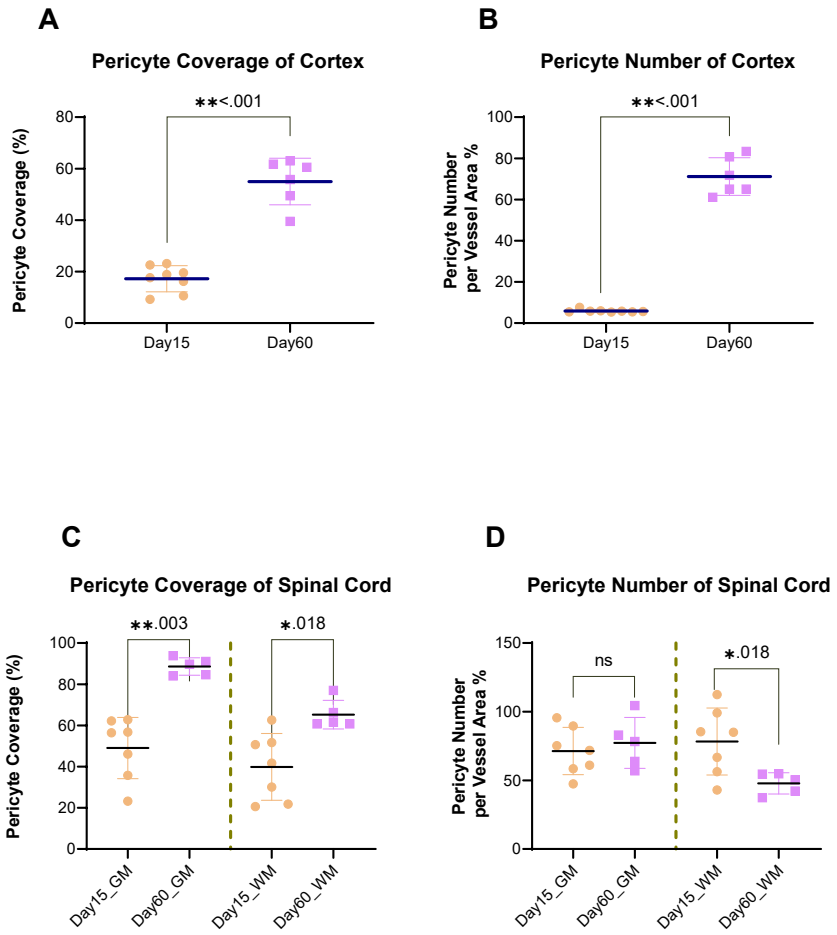

Figure 30. Comparison of Pericyte Ablation by two doses of tamoxifen at Day 15 and Day 60

A and B show the pericyte coverage and number in the cortex, respectively. n=7 for Day15 and n=6 for Day 60. The difference between the pericyte ablation in the cortex in terms of both pericyte coverage and number in Day15 and Day60 were significant, $p<0.001$. C and D show the pericyte coverage and number in the spinal cord, respectively—n=7 for Day 15 and n=5 for Day60. The difference between the pericyte coverage in the spinal cord significantly increased from Day15 to Day60, $p=0.003$ in the gray matter and $p=0.018$ in the white matter. In D, the pericyte number again significantly increased in the white matter of the Day60 animals compared to Day15. Even though there was a slight increase in the pericyte number in the gray matter, this increase was not significant. Statistical analysis was done by Student's t-test (two-tailed Mann-Whitney test). The error bars show the SDs.

Appendix F. Statistical Analysis Results of Figure 51

For Figure 51 B

Sidak's multiple comparisons test	Mean Diff.	95.00% CI of diff.	Significant?	Summary	Adjusted P Value			
Tamoxifen free Control, n=13 - Group C								
1	6.764	5.065 to 8.463	Yes					
2	7.417	5.321 to 9.512	Yes					
4	7.725	3.416 to 12.03	Yes					
6	7.481	3.257 to 11.71	Yes					
8	9.124	3.860 to 14.39	Yes					
10	7.945	2.781 to 13.11	Yes					
12	12.91	6.798 to 19.02	Yes					
14	8.179	2.085 to 14.27	Yes					

Test details	Mean 1	Mean 2	Mean Diff.	SE of diff.	N1	N2	t	DF
Tamoxifen free Control, n=13 - Group C								
0								
1	101.3	94.50	6.764	0.8315	13	19	8.134	29.81
2	101.0	93.54	7.417	1.026	13	19	7.230	29.91
4	104.4	96.65	7.725	2.109	13	19	3.663	29.71
6	104.3	96.78	7.481	2.068	13	19	3.618	29.88
8	104.9	95.76	9.124	2.552	13	19	3.575	24.23
10	105.5	97.57	7.945	2.508	13	19	3.168	25.09
12	106.1	93.15	12.91	2.987	13	19	4.322	28.66
14	105.7	97.55	8.179	2.966	13	19	2.757	26.31

For Figure 51 C

Sidak's multiple comparisons test	Mean Diff.	95.00% CI of diff.	Significant?	Summary	Adjusted P Value			
Group B - Group C								
1	0.6186	-1.913 to 3.150	No					
2	3.144	-1.748 to 8.036	No					
4	6.301	1.530 to 11.07	Yes					
6	9.131	4.739 to 13.52	Yes					
8	10.17	6.233 to 14.10	Yes					
10	6.847	3.055 to 10.64	Yes					
12	12.19	7.234 to 17.15	Yes					
14	8.295	4.059 to 12.53	Yes					

Test details	Mean 1	Mean 2	Mean Diff.	SE of diff.	N1	N2	t	DF
Group B - Group C								
0								
1	95.12	94.50	0.6186	1.202	11	19	0.5146	17.38
2	96.68	93.54	3.144	2.259	11	19	1.391	12.73
4	102.9	96.65	6.301	2.324	11	19	2.711	26.63
6	105.9	96.78	9.131	2.139	11	19	4.269	26.57
8	105.9	95.76	10.17	1.921	11	19	5.293	28.00
10	104.4	97.57	6.847	1.850	11	19	3.701	27.55
12	105.3	93.15	12.19	2.415	11	19	5.049	26.52
14	105.8	97.55	8.295	2.046	11	19	4.055	22.64

For Figure 51 D

Number of families	1							
Number of comparisons per family	8							
Alpha	0.05							
Sidak's multiple comparisons test	**Mean Diff.**	**95.00% CI of diff.**	**Significant?**	**Summary**	**Adjusted P Value**			
Tamoxifen free Control, n=13 - Group B								
1	6.145	3.666 to 8.625	Yes					
2	4.273	-0.5756 to 9.122	No					
4	1.424	-2.790 to 5.638	No					
6	-1.650	-5.798 to 2.498	No					
8	-1.044	-5.960 to 3.872	No					
10	1.098	-3.556 to 5.751	No					
12	0.7169	-4.392 to 5.826	No					
14	-0.1160	-5.203 to 4.971	No					
Test details	**Mean 1**	**Mean 2**	**Mean Diff.**	**SE of diff.**	**N1**	**N2**	**t**	**DF**
Tamoxifen free Control, n=13 - Group B								
0								
1	101.3	95.12	6.145	1.166	13	11	5.268	15.50
2	101.0	96.68	4.273	2.225	13	11	1.920	12.00
4	104.4	102.9	1.424	2.020	13	11	0.7050	19.89
6	104.3	105.9	-1.650	1.997	13	11	0.8262	21.41
8	104.9	105.9	-1.044	2.346	13	11	0.4451	18.65
10	105.5	104.4	1.098	2.212	13	11	0.4963	17.64
12	106.1	105.3	0.7169	2.437	13	11	0.2942	18.55
14	105.7	105.8	-0.1160	2.377	13	11	0.04878	14.37

Appendix G. Experimental Plan for the combination of inducible pericyte ablation and EAE

Application	DAY TAM.	DAY Hooke	DATE Group 1	DATE Group 2	DATE Group 3
Tamoxifen1	0		Saturday, Aug 8	Monday, Aug 10	Wednesday, Aug 12
Tamoxifen2	1		Sunday, Aug 9	Tuesday, Aug 11	Thursday, Aug 13
	2		Monday, Aug 10	Wednesday, Aug 12	Friday, Aug 14
	3		Tuesday, Aug 11	Thursday, Aug 13	Saturday, Aug 15
	4		Wednesday, Aug 12	Friday, Aug 14	Sunday, Aug 16
	5		Thursday, Aug 13	Saturday, Aug 15	Monday, Aug 17
	6		Friday, Aug 14	Sunday, Aug 16	Tuesday, Aug 18
	7		Saturday, Aug 15	Monday, Aug 17	Wednesday, Aug 19
	8		Sunday, Aug 16	Tuesday, Aug 18	Thursday, Aug 20
	9		Monday, Aug 17	Wednesday, Aug 19	Friday, Aug 21
	10		Tuesday, Aug 18	Thursday, Aug 20	Saturday, Aug 22
	11		Wednesday, Aug 19	Friday, Aug 21	Sunday, Aug 23
	12		Thursday, Aug 20	Saturday, Aug 22	Monday, Aug 24
	13		Friday, Aug 21	Sunday, Aug 23	Tuesday, Aug 25
	14		Saturday, Aug 22	Monday, Aug 24	Wednesday, Aug 26
Hooke-PTX1	15	0	Sunday, Aug 23	Tuesday, Aug 25	Thursday, Aug 27
PTX2	16	1	Monday, Aug 24	Wednesday, Aug 26	Friday, Aug 28
	17	2	Tuesday,	Thursday,	Saturday,

			Aug 25	Aug 27	Aug 29
	18	3	Wednesday, Aug 26	Friday, Aug 28	Sunday, Aug 30
	19	4	Thursday, Aug 27	Saturday, Aug 29	Monday, Aug 31
	20	5	Friday, Aug 28	Sunday, Aug 30	Tuesday, Sep 1
	21	6	Saturday, Aug 29	Monday, Aug 31	Wednesday, Sep 2
	22	7	Sunday, Aug 30	Tuesday, Sep 1	Thursday, Sep 3
score	23	8	Monday, Aug 31	Wednesday, Sep 2	Friday, Sep 4
	24	9	Tuesday, Sep 1	Thursday, Sep 3	Saturday, Sep 5
score	25	10	Wednesday, Sep 2	Friday, Sep 4	Sunday, Sep 6
	26	11	Thursday, Sep 3	Saturday, Sep 5	Monday, Sep 7
score	27	12	Friday, Sep 4	Sunday, Sep 6	Tuesday, Sep 8
	28	13	Saturday, Sep 5	Monday, Sep 7	Wednesday, Sep 9
score	29	14	Sunday, Sep 6	Tuesday, Sep 8	Thursday, Sep 10
	30	15	Monday, Sep 7	Wednesday, Sep 9	Friday, Sep 11
score	31	16	Tuesday, Sep 8	Thursday, Sep 10	Saturday, Sep 12
	32	17	Wednesday, Sep 9	Friday, Sep 11	Sunday, Sep 13
score	33	18	Thursday, Sep 10	Saturday, Sep 12	Monday, Sep 14
	34	19	Friday, Sep 11	Sunday, Sep 13	Tuesday, Sep 15
score	35	20	Saturday, Sep 12	Monday, Sep 14	Wednesday, Sep 16
	36	21	Sunday, Sep 13	Tuesday, Sep 15	Thursday, Sep 17
score	37	22	Monday, Sep 14	Wednesday, Sep 16	Friday, Sep 18
	38	23	Tuesday,	Thursday,	Saturday,

			Sep 15	Sep 17	Sep 19
score	39	24	Wednesday, Sep 16	Friday, Sep 18	Sunday, Sep 20
	40	25	Thursday, Sep 17	Saturday, Sep 19	Monday, Sep 21
score	41	26	Friday, Sep 18	Sunday, Sep 20	Tuesday, Sep 22
	42	27	Saturday, Sep 19	Monday, Sep 21	Wednesday, Sep 23
score	43	28	Sunday, Sep 20	Tuesday, Sep 22	Thursday, Sep 24
ex dates	44	29	Monday, Sep 21	Wednesday, Sep 23	Friday, Sep 25

Appendix H. Summary Tables of Pericyte Ablation

Table 7. Dose Dependent Pericyte Ablation Ratios in Short and Long Time Points

Tissue Type / Dosage of TAM		Short term	Long term	Short term	Long term
		Reduction of Pericyte Coverage (%)		Reduction of Pericyte Number (%)	
BRAIN	5X	75			
	3X	80	75		
	2X	75	45	45	30
SPINAL CORD (GRAY MATTER)	2X	40	25	30	25
SPINAL CORD (WHITE MATTER)	2X	50	35	35	50

Table 8. Pericyte Ablation Ratios after Neuroinflammation

Tissue Type / Dosage of TAM		43 Days After the Cre Activation and 28 Days After the EAE induction	
		Reduction of Pericyte Coverage (%)	Reduction of Pericyte Number (%)
BRAIN	2X	80	85

BIBLIOGRAPHY

1 Zudaire, E., Gambardella, L., Kurcz, C. & Vermeren, S. A computational tool for quantitative analysis of vascular networks. *PLoS One* **6**, e27385, doi:10.1371/journal.pone.0027385 (2011).

2 Bear, M., Connors, B. & Paradiso, M. A. *Neuroscience: Exploring the Brain, Enhanced Edition: Exploring the Brain, Enhanced Edition*. (Jones & Bartlett Learning, 2020).

3 Cockerill, I., Oliver, J. A., Xu, H., Fu, B. M. & Zhu, D. Blood-Brain Barrier Integrity and Clearance of Amyloid-beta from the BBB. *Adv Exp Med Biol* **1097**, 261-278, doi:10.1007/978-3-319-96445-4_14 (2018).

4 Valabrègue, R., Aubert, A., Burger, J., Bittoun, J. & Costalat, R. Relation between cerebral blood flow and metabolism explained by a model of oxygen exchange. *Journal of Cerebral Blood Flow & Metabolism* **23**, 536-545 (2003).

5 Zlokovic, B. V. The blood-brain barrier in health and chronic neurodegenerative disorders. *Neuron* **57**, 178-201, doi:10.1016/j.neuron.2008.01.003 (2008).

6 Lippmann, E. S. *et al.* Derivation of blood-brain barrier endothelial cells from human pluripotent stem cells. *Nat Biotechnol* **30**, 783-791, doi:10.1038/nbt.2247 (2012).

7 Kniesel, U. & Wolburg, H. Tight junctions of the blood-brain barrier. *Cell Mol Neurobiol* **20**, 57-76, doi:10.1023/a:1006995910836 (2000).

8 Shrestha, R., Millington, O., Brewer, J. & Bushell, T. Is central nervous system an immune-privileged site? *Kathmandu University Medical Journal* **11**, 102-107 (2013).

9 Lai, C. H. & Kuo, K. H. The critical component to establish in vitro BBB model: Pericyte. *Brain Res Brain Res Rev* **50**, 258-265, doi:10.1016/j.brainresrev.2005.07.004 (2005).

10 Chun, H. B. *et al.* The proteome of mouse brain microvessel membranes and basal lamina. *J Cereb Blood Flow Metab* **31**, 2267-2281, doi:10.1038/jcbfm.2011.104 (2011).

11 Muoio, V., Persson, P. B. & Sendeski, M. M. The neurovascular unit - concept review. *Acta Physiol (Oxf)* **210**, 790-798, doi:10.1111/apha.12250 (2014).

12 Allt, G. & Lawrenson, J. G. Pericytes: cell biology and pathology. *Cells Tissues Organs* **169**, 1-11, doi:10.1159/000047855 (2001).

13 Balabanov, R. & Dore-Duffy, P. Role of the CNS microvascular pericyte in the blood-brain barrier. *J Neurosci Res* **53**, 637-644, doi:10.1002/(SICI)1097-4547(19980915)53:6<637::AID-JNR1>3.0.CO;2-6 (1998).

14 Alarcon-Martinez, L., Yemisci, M. & Dalkara, T. Pericyte morphology and function. *Histol Histopathol* **36**, 633-643, doi:10.14670/HH-18-314 (2021).

15 Fisher, M. Pericyte signaling in the neurovascular unit. *Stroke* **40**, S13-15, doi:10.1161/STROKEAHA.108.533117 (2009).

16 Harrell, C. R. *et al.* Molecular mechanisms underlying therapeutic potential of pericytes. *J Biomed Sci* **25**, 21, doi:10.1186/s12929-018-0423-7 (2018).

17 Caruso, R. A. *et al.* Ultrastructural descriptions of pericyte/endothelium peg-socket interdigitations in the microvasculature of human gastric carcinomas. *Anticancer Res* **29**, 449-453 (2009).

18 Berthiaume, A. A., Hartmann, D. A., Majesky, M. W., Bhat, N. R. & Shih, A. Y. Pericyte Structural Remodeling in Cerebrovascular Health and Homeostasis. *Front Aging Neurosci* **10**, 210, doi:10.3389/fnagi.2018.00210 (2018).

19 Hartmann, D. A. *et al.* Pericyte structure and distribution in the cerebral cortex revealed by high-resolution imaging of transgenic mice. *Neurophotonics* **2**, 041402, doi:10.1117/1.NPh.2.4.041402 (2015).

20 Grant, R. I. *et al.* Organizational hierarchy and structural diversity of microvascular pericytes in adult mouse cortex. *J Cereb Blood Flow Metab* **39**, 411-425, doi:10.1177/0271678X17732229 (2019).

21 Dore-Duffy, P., Katychev, A., Wang, X. & Van Buren, E. CNS microvascular pericytes exhibit multipotential stem cell activity. *J Cereb Blood Flow Metab* **26**, 613-624, doi:10.1038/sj.jcbfm.9600272 (2006).

22 Daneman, R. *et al.* The mouse blood-brain barrier transcriptome: a new resource for understanding the development and function of brain endothelial cells. *PLoS One* **5**, e13741, doi:10.1371/journal.pone.0013741 (2010).

23 Yemisci, M. *et al.* Pericyte contraction induced by oxidative-nitrative stress impairs capillary reflow despite successful opening of an occluded cerebral artery. *Nat Med* **15**, 1031-1037, doi:10.1038/nm.2022 (2009).

24 Stallcup, W. B. The NG2 proteoglycan: past insights and future prospects. *J Neurocytol* **31**, 423-435, doi:10.1023/a:1025731428581 (2002).

25 Ozerdem, U. & Stallcup, W. B. Pathological angiogenesis is reduced by targeting pericytes via the NG2 proteoglycan. *Angiogenesis* **7**, 269-276, doi:10.1007/s10456-004-4182-6 (2004).

26 Kunz, J., Krause, D., Kremer, M. & Dermietzel, R. The 140-kDa protein of blood-brain barrier-associated pericytes is identical to aminopeptidase N. *J Neurochem* **62**, 2375-2386, doi:10.1046/j.1471-4159.1994.62062375.x (1994).

27 Mina-Osorio, P. *et al.* CD13 is a novel mediator of monocytic/endothelial cell adhesion. *J Leukoc Biol* **84**, 448-459, doi:10.1189/jlb.1107802 (2008).

28 Nehls, V. & Drenckhahn, D. The versatility of microvascular pericytes: from mesenchyme to smooth muscle? *Histochemistry* **99**, 1-12, doi:10.1007/BF00268014 (1993).

29 Cho, H., Kozasa, T., Bondjers, C., Betsholtz, C. & Kehrl, J. H. Pericyte-specific expression of Rgs5: implications for PDGF and EDG receptor signaling during vascular maturation. *FASEB J* **17**, 440-442, doi:10.1096/fj.02-0340fje (2003).

30 Bondjers, C. *et al.* Transcription profiling of platelet-derived growth factor-B-deficient mouse embryos identifies RGS5 as a novel marker for pericytes and vascular smooth muscle cells. *Am J Pathol* **162**, 721-729, doi:10.1016/S0002-9440(10)63868-0 (2003).

31 Bondjers, C. *et al.* Microarray analysis of blood microvessels from PDGF-B and PDGF-Rbeta mutant mice identifies novel markers for brain pericytes. *FASEB J* **20**, 1703-1705, doi:10.1096/fj.05-4944fje (2006).

32 Falix, F. A., Aronson, D. C., Lamers, W. H. & Gaemers, I. C. Possible roles of DLK1 in the Notch pathway during development and disease. *Biochim Biophys Acta* **1822**, 988-995, doi:10.1016/j.bbadis.2012.02.003 (2012).

33 Tigges, U., Welser-Alves, J. V., Boroujerdi, A. & Milner, R. A novel and simple method for culturing pericytes from mouse brain. *Microvasc Res* **84**, 74-80, doi:10.1016/j.mvr.2012.03.008 (2012).

34 Park, T. I. *et al.* Cultured pericytes from human brain show phenotypic and functional differences associated with differential CD90 expression. *Sci Rep* **6**, 26587, doi:10.1038/srep26587 (2016).

35 Nehls, V., Denzer, K. & Drenckhahn, D. Pericyte involvement in capillary sprouting during angiogenesis in situ. *Cell Tissue Res* **270**, 469-474, doi:10.1007/BF00645048 (1992).

36 Sweeney, M. D., Ayyadurai, S. & Zlokovic, B. V. Pericytes of the neurovascular unit: key functions and signaling pathways. *Nat Neurosci* **19**, 771-783, doi:10.1038/nn.4288 (2016).

37 Brozovich, F. V. *et al.* Mechanisms of Vascular Smooth Muscle Contraction and the Basis for Pharmacologic Treatment of Smooth Muscle Disorders. *Pharmacol Rev* **68**, 476-532, doi:10.1124/pr.115.010652 (2016).

38 Stratman, A. N., Schwindt, A. E., Malotte, K. M. & Davis, G. E. Endothelial-derived PDGF-BB and HB-EGF coordinately regulate pericyte recruitment during vasculogenic tube assembly and stabilization. *Blood* **116**, 4720-4730, doi:10.1182/blood-2010-05-286872 (2010).

39 Nehls, V. & Drenckhahn, D. Demonstration of actin filament stress fibers in microvascular endothelial cells in situ. *Microvasc Res* **42**, 103-112, doi:10.1016/0026-2862(91)90078-p (1991).

40 Kapanci, Y., Ribaux, C., Chaponnier, C. & Gabbiani, G. Cytoskeletal features of alveolar myofibroblasts and pericytes in normal human and rat lung. *J Histochem Cytochem* **40**, 1955-1963, doi:10.1177/40.12.1333502 (1992).

41 Hall, C. N. *et al.* Capillary pericytes regulate cerebral blood flow in health and disease. *Nature* **508**, 55-60, doi:10.1038/nature13165 (2014).

42 O'Farrell, F. M. & Attwell, D. A role for pericytes in coronary no-reflow. *Nat Rev Cardiol* **11**, 427-432, doi:10.1038/nrcardio.2014.58 (2014).

43 Nikolakopoulou, A. M. *et al.* Pericyte loss leads to circulatory failure and pleiotrophin depletion causing neuron loss. *Nat Neurosci* **22**, 1089-1098, doi:10.1038/s41593-019-0434-z (2019).

44 Stratman, A. N., Malotte, K. M., Mahan, R. D., Davis, M. J. & Davis, G. E. Pericyte recruitment during vasculogenic tube assembly stimulates endothelial basement membrane matrix formation. *Blood* **114**, 5091-5101, doi:10.1182/blood-2009-05-222364 (2009).

45 Diaz-Flores, L. *et al.* Pericytes. Morphofunction, interactions and pathology in a quiescent and activated mesenchymal cell niche. *Histol Histopathol* **24**, 909-969, doi:10.14670/HH-24.909 (2009).

46 Frank, R. N., Dutta, S. & Mancini, M. A. Pericyte coverage is greater in the retinal than in the cerebral capillaries of the rat. *Invest Ophthalmol Vis Sci* **28**, 1086-1091 (1987).

47 Shepro, D. & Morel, N. M. Pericyte physiology. *FASEB J* **7**, 1031-1038, doi:10.1096/fasebj.7.11.8370472 (1993).

48 Hori, S., Ohtsuki, S., Hosoya, K., Nakashima, E. & Terasaki, T. A pericyte-derived angiopoietin-1 multimeric complex induces occludin gene expression in brain capillary endothelial cells through Tie-2 activation in vitro. *J Neurochem* **89**, 503-513, doi:10.1111/j.1471-4159.2004.02343.x (2004).

49 Tilton, R. G., Kilo, C. & Williamson, J. R. Pericyte-endothelial relationships in cardiac and skeletal muscle capillaries. *Microvasc Res* **18**, 325-335, doi:10.1016/0026-2862(79)90041-4 (1979).

50 Armulik, A. *et al.* Pericytes regulate the blood-brain barrier. *Nature* **468**, 557-561, doi:10.1038/nature09522 (2010).

51 Banks, W. A. From blood-brain barrier to blood-brain interface: new opportunities for CNS drug delivery. *Nat Rev Drug Discov* **15**, 275-292, doi:10.1038/nrd.2015.21 (2016).

52 Daneman, R., Zhou, L., Kebede, A. A. & Barres, B. A. Pericytes are required for blood-brain barrier integrity during embryogenesis. *Nature* **468**, 562-566, doi:10.1038/nature09513 (2010).

53 Risau, W. Mechanisms of angiogenesis. *Nature* **386**, 671-674, doi:10.1038/386671a0 (1997).

54 Krock, B. L., Skuli, N. & Simon, M. C. Hypoxia-induced angiogenesis: good and evil. *Genes Cancer* **2**, 1117-1133, doi:10.1177/1947601911423654 (2011).

55 Gerhardt, H. *et al.* VEGF guides angiogenic sprouting utilizing endothelial tip cell filopodia. *J Cell Biol* **161**, 1163-1177, doi:10.1083/jcb.200302047 (2003).

56 Hellstrom, M., Phng, L. K. & Gerhardt, H. VEGF and Notch signaling: the yin and yang of angiogenic sprouting. *Cell Adh Migr* **1**, 133-136, doi:10.4161/cam.1.3.4978 (2007).

57 Barnett, J. M. *et al.* Pharmacologic and genetic manipulation of MMP-2 and -9 affects retinal neovascularization in rodent models of OIR. *Invest Ophthalmol Vis Sci* **48**, 907-915, doi:10.1167/iovs.06-0082 (2007).

58 Grako, K. A., Ochiya, T., Barritt, D., Nishiyama, A. & Stallcup, W. B. PDGF (alpha)-receptor is unresponsive to PDGF-AA in aortic smooth muscle cells from the NG2 knockout mouse. *J Cell Sci* **112 (Pt 6)**, 905-915 (1999).

59 Grako, K. A. & Stallcup, W. B. Participation of the NG2 proteoglycan in rat aortic smooth muscle cell responses to platelet-derived growth factor. *Exp Cell Res* **221**, 231-240, doi:10.1006/excr.1995.1371 (1995).

60 Hellstrom, M., Kalen, M., Lindahl, P., Abramsson, A. & Betsholtz, C. Role of PDGF-B and PDGFR-beta in recruitment of vascular smooth muscle cells and pericytes during embryonic blood vessel formation in the mouse. *Development* **126**, 3047-3055 (1999).

61 Betsholtz, C. *et al.* Role of platelet-derived growth factor in mesangium development and vasculopathies: lessons from platelet-derived growth factor and platelet-derived growth factor receptor mutations in mice. *Curr Opin Nephrol Hy* **13**, 45-52, doi:10.1097/00041552-200401000-00007 (2004).

62 Hirschi, K. D. Expression of Arabidopsis CAX1 in tobacco: altered calcium homeostasis and increased stress sensitivity. *Plant Cell* **11**, 2113-2122, doi:10.1105/tpc.11.11.2113 (1999).

63 Thurston, G. Role of Angiopoietins and Tie receptor tyrosine kinases in angiogenesis and lymphangiogenesis. *Cell Tissue Res* **314**, 61-68, doi:10.1007/s00441-003-0749-6 (2003).

64 Leveen, P. *et al.* Mice deficient for PDGF B show renal, cardiovascular, and hematological abnormalities. *Genes Dev* **8**, 1875-1887, doi:10.1101/gad.8.16.1875 (1994).

65 Soriano, P. Abnormal kidney development and hematological disorders in PDGF beta-receptor mutant mice. *Genes Dev* **8**, 1888-1896, doi:10.1101/gad.8.16.1888 (1994).

66 Shih, A. H. & Holland, E. C. Platelet-derived growth factor (PDGF) and glial tumorigenesis. *Cancer Lett* **232**, 139-147, doi:10.1016/j.canlet.2005.02.002 (2006).

67 Benjamin, L. E., Hemo, I. & Keshet, E. A plasticity window for blood vessel remodelling is defined by pericyte coverage of the preformed endothelial network and is regulated by PDGF-B and VEGF. *Development* **125**, 1591-1598 (1998).

68 Rolls, A., Shechter, R. & Schwartz, M. The bright side of the glial scar in CNS repair. *Nat Rev Neurosci* **10**, 235-241, doi:10.1038/nrn2591 (2009).

69 Fawcett, J. W. & Asher, R. A. The glial scar and central nervous system repair. *Brain Res Bull* **49**, 377-391, doi:10.1016/s0361-9230(99)00072-6 (1999).

70 Sofroniew, M. V. Molecular dissection of reactive astrogliosis and glial scar formation. *Trends Neurosci* **32**, 638-647, doi:10.1016/j.tins.2009.08.002 (2009).

71 Gurtner, G. C., Werner, S., Barrandon, Y. & Longaker, M. T. Wound repair and regeneration. *Nature* **453**, 314-321, doi:10.1038/nature07039 (2008).

72 Greenhalgh, S. N., Iredale, J. P. & Henderson, N. C. Origins of fibrosis: pericytes take centre stage. *F1000Prime Rep* **5**, 37, doi:10.12703/P5-37 (2013).

73 Goritz, C. *et al.* A pericyte origin of spinal cord scar tissue. *Science* **333**, 238-242, doi:10.1126/science.1203165 (2011).

74 Rustenhoven, J. *et al.* TGF-beta1 regulates human brain pericyte inflammatory processes involved in neurovasculature function. *J Neuroinflammation* **13**, 37, doi:10.1186/s12974-016-0503-0 (2016).

75 Navarro, R. *et al.* Role of nucleotide-binding oligomerization domain 1 (NOD1) in pericyte-mediated vascular inflammation. *J Cell Mol Med* **20**, 980-986, doi:10.1111/jcmm.12804 (2016).

76 Rustenhoven, J., Jansson, D., Smyth, L. C. & Dragunow, M. Brain Pericytes As Mediators of Neuroinflammation. *Trends Pharmacol Sci* **38**, 291-304, doi:10.1016/j.tips.2016.12.001 (2017).

77 Kamouchi, M., Ago, T. & Kitazono, T. Brain pericytes: emerging concepts and functional roles in brain homeostasis. *Cell Mol Neurobiol* **31**, 175-193, doi:10.1007/s10571-010-9605-x (2011).

78 Persidsky, Y. *et al.* Dysfunction of brain pericytes in chronic neuroinflammation. *J Cereb Blood Flow Metab* **36**, 794-807, doi:10.1177/0271678X15606149 (2016).

79 Duan, G., Song, S. & Niu, S. WITHDRAWN: Long non-coding RNA HOTAIR promotes LPS-induced inflammatory injury by down-regulation of microRNA-124 in murine chondrogenic ATDC5 cells. *Life Sci*, doi:10.1016/j.lfs.2018.07.039 (2018).

80 Lindahl, P., Johansson, B. R., Leveen, P. & Betsholtz, C. Pericyte loss and microaneurysm formation in PDGF-B-deficient mice. *Science* **277**, 242-245, doi:10.1126/science.277.5323.242 (1997).

81 Watson, A. N. *et al.* Mild pericyte deficiency is associated with aberrant brain microvascular flow in aged PDGFRbeta(+/-) mice. *J Cereb Blood Flow Metab* **40**, 2387-2400, doi:10.1177/0271678X19900543 (2020).

82 Tallquist, M. D., French, W. J. & Soriano, P. Additive effects of PDGF receptor beta signaling pathways in vascular smooth muscle cell development. *PLoS Biol* **1**, E52, doi:10.1371/journal.pbio.0000052 (2003).

83 Bell, R. D. *et al.* Pericytes control key neurovascular functions and neuronal phenotype in the adult brain and during brain aging. *Neuron* **68**, 409-427, doi:10.1016/j.neuron.2010.09.043 (2010).

84 Lindblom, P. Endothelial PDGF-B retention is required for proper investment of pericytes in the microvessel wall. *Genes & Development* **17**, 1835-1840, doi:10.1101/gad.266803 (2003).

85 Torok, O. *et al.* Pericytes regulate vascular immune homeostasis in the CNS. *Proc Natl Acad Sci U S A* **118**, doi:10.1073/pnas.2016587118 (2021).

86 Winkler, E. A., Sengillo, J. D., Bell, R. D., Wang, J. & Zlokovic, B. V. Blood-spinal cord barrier pericyte reductions contribute to increased capillary permeability. *J Cereb Blood Flow Metab* **32**, 1841-1852, doi:10.1038/jcbfm.2012.113 (2012).

87 Montagne, A. *et al.* Pericyte degeneration causes white matter dysfunction in the mouse central nervous system. *Nature Medicine* **24**, 326-337, doi:10.1038/nm.4482 (2018).

88 Gustafsson, E., Brakebusch, C., Hietanen, K. & Fassler, R. Tie-1-directed expression of Cre recombinase in endothelial cells of embryoid bodies and transgenic mice. *J Cell Sci* **114**, 671-676 (2001).

89 Enge, M. *et al.* Endothelium-specific platelet-derived growth factor-B ablation mimics diabetic retinopathy. *EMBO J* **21**, 4307-4316, doi:10.1093/emboj/cdf418 (2002).

90 Bjarnegard, M. *et al.* Endothelium-specific ablation of PDGFB leads to pericyte loss and glomerular, cardiac and placental abnormalities. *Development* **131**, 1847-1857, doi:10.1242/dev.01080 (2004).

91 Walton, C. *et al.* Rising prevalence of multiple sclerosis worldwide: Insights from the Atlas of MS, third edition. *Mult Scler* **26**, 1816-1821, doi:10.1177/1352458520970841 (2020).

92 Torkildsen, O. *et al.* Living with secondary progressive multiple sclerosis in Europe: perspectives of multiple stakeholders. *Neurodegener Dis Manag* **11**, 9-19, doi:10.2217/nmt-2020-0054 (2021).

93 Reich, D. S., Lucchinetti, C. F. & Calabresi, P. A. Multiple Sclerosis. *N Engl J Med* **378**, 169-180, doi:10.1056/NEJMra1401483 (2018).

94 Filippi, M. *et al.* Multiple sclerosis. *Nat Rev Dis Primers* **4**, 43, doi:10.1038/s41572-018-0041-4 (2018).

95 Schapiro, R. T. Managing symptoms of multiple sclerosis. *Neurol Clin* **23**, 177-187, vii, doi:10.1016/j.ncl.2004.09.001 (2005).

96 Henze, T. Managing specific symptoms in people with multiple sclerosis. *Int MS J* **12**, 60-68 (2005).

97 Valentino, P. *et al.* Cognitive deficits in multiple sclerosis patients with cerebellar symptoms. *Mult Scler* **15**, 854-859, doi:10.1177/1352458509104589 (2009).

98 Surekha, D., Manasa, D. & Vutla, V. R.

99 McKay, K. A., Kwan, V., Duggan, T. & Tremlett, H. Risk factors associated with the onset of relapsing-remitting and primary progressive multiple sclerosis: a systematic review. *Biomed Res Int* **2015**, 817238, doi:10.1155/2015/817238 (2015).

100 Pollinger, B. *et al.* Spontaneous relapsing-remitting EAE in the SJL/J mouse: MOG-reactive transgenic T cells recruit endogenous MOG-specific B cells. *J Exp Med* **206**, 1303-1316, doi:10.1084/jem.20090299 (2009).

101 Koch, M., Kingwell, E., Rieckmann, P., Tremlett, H. & Neurologists, U. M. C. The natural history of secondary progressive multiple sclerosis. *J Neurol Neurosurg Psychiatry* **81**, 1039-1043, doi:10.1136/jnnp.2010.208173 (2010).

102 McCormack, P. L. & Scott, L. J. Interferon-beta-1b: a review of its use in relapsing-remitting and secondary progressive multiple sclerosis. *CNS Drugs* **18**, 521-546, doi:10.2165/00023210-200418080-00004 (2004).

103 Alonso, A. & Hernan, M. A. Temporal trends in the incidence of multiple sclerosis: a systematic review. *Neurology* **71**, 129-135, doi:10.1212/01.wnl.0000316802.35974.34 (2008).

104 Miller, D. H. & Leary, S. M. Primary-progressive multiple sclerosis. *Lancet Neurol* **6**, 903-912, doi:10.1016/S1474-4422(07)70243-0 (2007).

105 Goodin, D. S. The causal cascade to multiple sclerosis: a model for MS pathogenesis. *PLoS One* **4**, e4565, doi:10.1371/journal.pone.0004565 (2009).

106 Grant, C. R., Liberal, R., Mieli-Vergani, G., Vergani, D. & Longhi, M. S. Regulatory T-cells in autoimmune diseases: challenges, controversies and--yet--unanswered questions. *Autoimmun Rev* **14**, 105-116, doi:10.1016/j.autrev.2014.10.012 (2015).

107 Willing, A. *et al.* CD8(+) MAIT cells infiltrate into the CNS and alterations in their blood frequencies correlate with IL-18 serum levels in multiple sclerosis. *Eur J Immunol* **44**, 3119-3128, doi:10.1002/eji.201344160 (2014).

108 Frisch, T. *et al.* Multiple Sclerosis Atlas: A Molecular Map of Brain Lesion Stages in Progressive Multiple Sclerosis. *Netw Syst Med* **3**, 122-129, doi:10.1089/nsm.2020.0006 (2020).

109 Peruzzo, D. *et al.* Heterogeneity of cortical lesions in multiple sclerosis: an MRI perfusion study. *J Cereb Blood Flow Metab* **33**, 457-463, doi:10.1038/jcbfm.2012.192 (2013).

110 Poser, C. M. The peripheral nervous system in multiple sclerosis. A review and pathogenetic hypothesis. *J Neurol Sci* **79**, 83-90, doi:10.1016/0022-510x(87)90262-0 (1987).

111 Martino, G. *et al.* Cytokines and immunity in multiple sclerosis: the dual signal hypothesis. *J Neuroimmunol* **109**, 3-9, doi:10.1016/s0165-5728(00)00295-2 (2000).

112 Olson, J. K., Croxford, J. L., Calenoff, M. A., Dal Canto, M. C. & Miller, S. D. A virus-induced molecular mimicry model of multiple sclerosis. *J Clin Invest* **108**, 311-318, doi:10.1172/JCI13032 (2001).

113 McCoy, L., Tsunoda, I. & Fujinami, R. S. Multiple sclerosis and virus induced immune responses: autoimmunity can be primed by molecular mimicry and augmented by bystander activation. *Autoimmunity* **39**, 9-19 (2006).

114 Loma, I. & Heyman, R. Multiple sclerosis: pathogenesis and treatment. *Curr Neuropharmacol* **9**, 409-416, doi:10.2174/157015911796557911 (2011).

115 Gold, R., Linington, C. & Lassmann, H. Understanding pathogenesis and therapy of multiple sclerosis via animal models: 70 years of merits and culprits in experimental autoimmune encephalomyelitis research. *Brain* **129**, 1953-1971, doi:10.1093/brain/awl075 (2006).

116 Confavreux, C. & Vukusic, S. Accumulation of irreversible disability in multiple sclerosis: from epidemiology to treatment. *Clin Neurol Neurosurg* **108**, 327-332, doi:10.1016/j.clineuro.2005.11.018 (2006).

117 Azevedo, P. O. *et al.* Pericytes modulate myelination in the central nervous system. *J Cell Physiol* **233**, 5523-5529, doi:10.1002/jcp.26348 (2018).

118 Silva, M. E. *et al.* Pericytes Favor Oligodendrocyte Fate Choice in Adult Neural Stem Cells. *Front Cell Neurosci* **13**, 85, doi:10.3389/fncel.2019.00085 (2019).

119 Grygorowicz, T., Dabrowska-Bouta, B. & Struzynska, L. Administration of an antagonist of P2X7 receptor to EAE rats prevents a decrease of expression of claudin-5 in cerebral capillaries. *Purinergic Signal* **14**, 385-393, doi:10.1007/s11302-018-9620-9 (2018).

120 Ulusoy, C. *et al.* Impact of Autoimmune Demyelinating Brain Disease Sera on Pericyte Survival. *Noro Psikiyatr Ars* **58**, 83-86, doi:10.29399/npa.27350 (2021).

121 Iacobaeus, E. *et al.* Dynamic Changes in Brain Mesenchymal Perivascular Cells Associate with Multiple Sclerosis Disease Duration, Active Inflammation, and Demyelination. *Stem Cells Transl Med* **6**, 1840-1851, doi:10.1002/sctm.17-0028 (2017).

122 Simmons, S. B., Pierson, E. R., Lee, S. Y. & Goverman, J. M. Modeling the heterogeneity of multiple sclerosis in animals. *Trends Immunol* **34**, 410-422, doi:10.1016/j.it.2013.04.006 (2013).

123 Constantinescu, C. S., Farooqi, N., O'Brien, K. & Gran, B. Experimental autoimmune encephalomyelitis (EAE) as a model for multiple sclerosis (MS). *Br J Pharmacol* **164**, 1079-1106, doi:10.1111/j.1476-5381.2011.01302.x (2011).

124 Batoulis, H., Recks, M. S., Addicks, K. & Kuerten, S. Experimental autoimmune encephalomyelitis--achievements and prospective advances. *APMIS* **119**, 819-830, doi:10.1111/j.1600-0463.2011.02794.x (2011).

125 Wuerfel, J. *et al.* Changes in cerebral perfusion precede plaque formation in multiple sclerosis: a longitudinal perfusion MRI study. *Brain* **127**, 111-119, doi:10.1093/brain/awh007 (2004).

126 Robinson, A. P., Harp, C. T., Noronha, A. & Miller, S. D. The experimental autoimmune encephalomyelitis (EAE) model of MS: utility for understanding disease pathophysiology and treatment. *Handb Clin Neurol* **122**, 173-189, doi:10.1016/B978-0-444-52001-2.00008-X (2014).

127 Mendel, I., Kerlero de Rosbo, N. & Ben-Nun, A. A myelin oligodendrocyte glycoprotein peptide induces typical chronic experimental autoimmune encephalomyelitis in H-2b mice: fine specificity and T cell receptor V beta expression of encephalitogenic T cells. *Eur J Immunol* **25**, 1951-1959, doi:10.1002/eji.1830250723 (1995).

128 Meek, C., Topcu, G., Moghaddam, N. & das Nair, R. Experiences of adjustment to secondary progressive multiple sclerosis: a meta-ethnographic systematic review. *Disabil Rehabil* **43**, 3135-3146, doi:10.1080/09638288.2020.1734105 (2021).

129 McRae, B. L. *et al.* Induction of active and adoptive relapsing experimental autoimmune encephalomyelitis (EAE) using an encephalitogenic epitope of proteolipid protein. *J Neuroimmunol* **38**, 229-240, doi:10.1016/0165-5728(92)90016-e (1992).

130 Mokhtarian, F., McFarlin, D. E. & Raine, C. S. Adoptive transfer of myelin basic protein-sensitized T cells produces chronic relapsing demyelinating disease in mice. *Nature* **309**, 356-358, doi:10.1038/309356a0 (1984).

131 Swamydas, M. & Lionakis, M. S. Isolation, purification and labeling of mouse bone marrow neutrophils for functional studies and adoptive transfer experiments. *J Vis Exp*, e50586, doi:10.3791/50586 (2013).

132 Hasselmann, J. P. C., Karim, H., Khalaj, A. J., Ghosh, S. & Tiwari-Woodruff, S. K. Consistent induction of chronic experimental autoimmune encephalomyelitis in C57BL/6 mice for the longitudinal study of pathology and repair. *J Neurosci Methods* **284**, 71-84, doi:10.1016/j.jneumeth.2017.04.003 (2017).

133 Sriram, S. & Steiner, I. Experimental allergic encephalomyelitis: a misleading model of multiple sclerosis. *Ann Neurol* **58**, 939-945, doi:10.1002/ana.20743 (2005).

134 Dendrou, C. A., Fugger, L. & Friese, M. A. Immunopathology of multiple sclerosis. *Nat Rev Immunol* **15**, 545-558, doi:10.1038/nri3871 (2015).

135 Winkler, E. A., Bell, R. D. & Zlokovic, B. V. Central nervous system pericytes in health and disease. *Nat Neurosci* **14**, 1398-1405, doi:10.1038/nn.2946 (2011).

136 Dalkara, T., Gursoy-Ozdemir, Y. & Yemisci, M. Brain microvascular pericytes in health and disease. *Acta Neuropathol* **122**, 1-9, doi:10.1007/s00401-011-0847-6 (2011).

137 Cheng, J. *et al.* Targeting pericytes for therapeutic approaches to neurological disorders. *Acta Neuropathol* **136**, 507-523, doi:10.1007/s00401-018-1893-0 (2018).

138 Montagne, A. *et al.* Pericyte degeneration causes white matter dysfunction in the mouse central nervous system. *Nat Med* **24**, 326-337, doi:10.1038/nm.4482 (2018).

139 Yang, R. & Dunn, J. F. Multiple sclerosis disease progression: Contributions from a hypoxia-inflammation cycle. *Mult Scler* **25**, 1715-1718, doi:10.1177/1352458518791683 (2019).

140 Vazquez-Liebanas, E. *et al.* Adult-induced genetic ablation distinguishes PDGFB roles in blood-brain barrier maintenance and development. *J Cereb Blood Flow Metab*, 271678X211056395, doi:10.1177/0271678X211056395 (2021).

141 Rajan, A. M., Ma, R. C., Kocha, K. M., Zhang, D. J. & Huang, P. Dual function of perivascular fibroblasts in vascular stabilization in zebrafish. *PLoS Genet* **16**, e1008800, doi:10.1371/journal.pgen.1008800 (2020).